A Study of Hydrogen Mobility
in Glassy Zr_2Pd
Using Internal Friction

Thesis by

Lowell Eugene Hazelton

In Partial Fulfillment of the Requirements
for the Degree of
Doctor of Philosophy

California Institute of Technology
Pasadena, California

1985

(Submitted 21 December 1984)

ACKNOWLEDGEMENTS

I want to express my great appreciation for the environment created by Professor William L. Johnson, and for his encouragement at crucial times. The physicists for whom I have the greatest respect are those who have a strong intuition for physics, and who solve problems on that basis. Bill is one of those people. The fact that he is easy to get along with has only increased my appreciation for his presence.

Several other people have contributed significantly to the pleasure and profit of my stay here. Dave Baxter has frequently been helpful with his knowledge of numerical techniques and of the computer. I have had many enjoyable discussions with Michael Atzmon on topics ranging from physics to life in general. He also contributed a very much appreciated last-minute review of this manuscript for errors large and small. Eric Cotts has more than once stimulated my thinking in new directions, to say nothing of the effect of his presence on spicing up life in the lab. I have had numerous enjoyable discussions with Xian Li Yeh on metal hydrides. Mike Tenhover and Bob Bowman provided me with several of the specimens used in this study.

Speaking of spicing up life, it would be unforgivable not to mention Concetto Geremia, who is always ready for a laugh, an argument or most any other needed diversion, in addition to rendering technical support. Angela Bressan deserves great appreciation for her help in preparing this manuscript, as does Darvia Herold, who provided far more help than I had originally anticipated needing.

Finally, the two most important people in my life also made a substantial contribution to my progress. Yvonne's emotional support and patience and Bryna's impatience with my getting finished provided much motivation. David and Berneva were also very supportive and went beyond the call of duty to help me through some rough times.

This work was supported by the United States Department of Energy, for which much appreciation is due.

ABSTRACT

Hydrogen-related internal friction peaks have been measured in amorphous Zr_2Pd and $Y_{64}Fe_{36}$, covering a range of hydrogen concentrations up to 0.86 H/M for the former alloy. The internal friction peaks were found to be several times wider than a peak due to a single relaxing defect, and quite asymmetric with a long low temperature tail, as with previous measurements on hydrogen in amorphous metals. They showed a thermally activated relaxation time with a frequency prefactor and a range of activation energies indicative of a point defect source. The evidence is shown to strongly indicate a Snoek-type defect, consisting of single hydrogen atoms in interstitial sites with strongly elliptical or variable strain dipole tensors. The integral equation that gives the internal friction is inverted for the first time to yield the distribution of relaxation times . It is suggested that the main peak in the resulting distribution of activation energies results from hydrogen hopping through three-sided faces, primarily between tetrahedral sites. These sites are found to change at high concentration to have a lower strain dipole ellipticity and to become more well-defined. This is interpreted as signaling a change in the structure of the amorphous metal itself. In addition there appear to be a small number of other deep-well sites where hydrogen is initially trapped at low concentrations. These have a very broad distribution of activation energies ranging from the main peak down to below 0.1 eV. A model is proposed to account for this by hopping of hydrogen between larger sites through distorted four-sided faces in the metal lattice.

CONTENTS

LIST OF TABLES

LIST OF FIGURES

GLOSSARY OF SYMBOLS

a	Lattice constant
a-	Prefix indicating an amorphous alloy
A_{ij}	m x n matrix relating g(E) to $Q^{-1}(T)$.
B	Bulk modulus.
bcc	Body centered cubic lattice.
c	Concentration of hydrogen expressed as a hydrogen to metal (H/M) atom number ratio.
c_{ν}	Concentration of hydrogen in sites of orientation ν.
D(E)	Density of electronic states in a metal.
d_o, d_1	Distance from internal friction specimen to receiver and drive electrodes, respectively.
DRPHS	Dense random packing of hard spheres.
DSC	Differential scanning calorimeter.
E	Young's modulus.
E_a	Activation energy for classical hydrogen hopping.
F	Free energy.

$f(C,\beta)$	Correction factor for calculating the internal friction value expected at a different vibration frequency and a corresponding temperature, given $Q^{-1}(\omega,T)$, for the case of a distribution of activation energies.
fcc	Face centered cubic lattice.
FWHM	Full width at half maximum.
G	a). Gibbs free energy. b). Shear modulus.
g(E)	Distribution of relaxation strengths over activation energy.
J	Hydrogen-hydrogen quantum interaction matrix element in a metal.
k	a). Boltzmann's constant. b). Pseudorank of the A matrix.
LHe	Liquid helium.
LN_2	Liquid nitrogen.
M	Symbol for a modulus of an unspecified type.
M_R	Relaxed modulus.
M_u	Unrelaxed modulus.
M_1	Real part of the dynamic modulus.
M_2	Imaginary part of the dynamic modulus.
δM	Anelastic modulus.
m, n	Dimensions of the matrix A.

N	Number of metal atoms in a solid.
n_d	Number of possible crystallographic orientations of a given defect.
n_t	Number of possible crystallographic orientations of a given strain tensor.
NMR	Nuclear magnetic resonance.
P	Macroscopic stress dipole tensor.
ΔP	Ellipticity of the stress dipole tensor.
Q^{-1}	Internal friction.
RDF	Radial distribution function.
SVD	Singular value decomposition method for inversion of an ill-conditioned equation.
T	Temperature.
T_f	Furnace temperature.
T_g	Glass transition temperature.
T_r	Room temperature.
V_o	Atomic volume of metal lattice atoms.
Z	Partition function.
β	a). Symbol for 1/kT. b). Geometrical factor in calculation of $\Delta\lambda$.

Γ	Jump rate for hydrogen out of a given site.
Δ	Relaxation strength $\delta M/M_R$.
$\underset{\sim}{\varepsilon}$	Strain tensor.
$\underset{\sim}{\lambda}$	Macroscopic strain dipole tensor.
$\Delta\lambda$	Ellipticity of strain dipole tensor.
μ or μ_H	Chemical potential of hydrogen in a metal.
$\Delta\mu$	Deviation of hydrogen's chemical potential from Sieverts' law.
ν	a). A label assigned to the various crystallographic orientations of a defect. b). Vibration frequency of a hydrogen atom in the potential well of an interstitial site.
ξ	A coordinate that lies along the route taken by a hydrogen atom in jumping between two sites.
ρ	Mass density.
$\underset{\sim}{\sigma}$	Stress tensor.
σ	Level of error in the Q^{-1} data.
σ_i	Order parameter, Le Claire-Lomer theory.
τ	Time constant, usually for hopping of hydrogen atoms.
τ_o	Prefactor for a thermally activated time constant.
ϕ^ν	Free energy of a single defect in orientation ν, excluding the configurational entropy contribution.

ω	Frequency, usually for vibration of internal friction specimen.
ω_o	Natural vibration frequency of an internal friction specimen.

1. INTRODUCTORY SURVEY

1.1 INTRODUCTION

The existence and properties of hydrogen dissolved in a metal have been investigated since 1866. When hydrogen enters a metal it displays several properties not found anywhere else. At temperatures below room temperature it diffuses faster in solids than any other element. It strains the metal so severely as to cause it in some cases to disintegrate into a powder. It is the prototype for the lattice gas, whose atoms are confined to discrete lattice points and which display a gas-liquid type phase transition. It is therefore a very interesting subject for study on its own, apart from any possible applications. The aspects of particular interest here will be briefly covered in this chapter.

Bulk amorphous metals were first discovered in 1959. They have been studied intensely since then, and now constitute a major field of research. They will be discussed in this chapter also, but only to the extent of outlining what is known about their atomic structure. In particular, possible interstitial sites for hydrogen in the amorphous lattice will be of interest, since hydrogen in all known cases enters metals as an interstitial rather than a substitutional atom. Hydrogen has been studied in amorphous metals only since 1978, and not yet in very great detail. Much remains to be learned about its behavior there.

The present investigation actually has a dual thrust. In addition to giving information on the mobility of hydrogen in amorphous metals, internal friction measurements essentially use the hydrogen atom as a microscopic probe of the structure of the metal itself. This will be used to study the hydrogen sites and the paths it takes in jumping from one site to another.

Chapter 2 will develop the theory of internal friction. Most of the discussion will be based on the simple case of atomic hopping in a crystalline material, where the defect is a single interstitial atom which occupies only one type of site. Internal friction measurements can give the activation energy and frequency prefactor for the atomic hopping, as well as information on the asymmetry of the hydrogen site. The strength of the relaxation which leads to internal friction depends on the square of the asymmetry. For an amorphous metal there is no longer just one type of site, and parameters such as well depth and the activation energy for hopping become distributed quantities, while the relaxation strength gives an average value for the site asymmetry factor.

Chapter 3 contains a description of the experimental apparatus, including the low-temperature vacuum probe and the drive and detection electronics. Measurements were made on thin amorphous Zr_2Pd specimens hydrogenated to different levels, as well as on an amorphous Y-Fe compound, over a temperature range of 10 K to 370 K. The results are presented in the first part of chapter 4 and show considerable qualitative similarity to internal friction results seen in other hydrogenated amorphous metals. The internal friction peaks are 3-5 times as wide as the simple Debye peak resulting from a relaxation involving only a single site, and are quite asymmetric, showing a long low-temperature tail. The mathematical techniques needed to deal with the results where the activation energy is distributed are then developed and applied for the first time to yield this distribution.

Chapter 5 contains an interpretation of the results in terms of possible hydrogen sites. The data appear to require two types of sites, a common site together with a less-common site with lower ground state energy which becomes filled first. Further, two types of hydrogen jump paths are proposed to explain the form of the data. In addition, changes with hydrogen concentration indicate a change in the nature of the predominant type of jump, and probably in the structure of the metal itself, at higher concentrations. Thus not only is the local mobility of hydrogen elucidated but much is inferred about the types of sites it occupies and about the atomic structure of the amorphous metal lattice itself.

1.2 HYDROGEN IN METALS

The first observation of hydrogen in a metal over a century ago started with the observation that palladium takes up large amounts of hydrogen, that it diffuses at a rapid rate and causes a great expansion and embrittlement of the metal, and that it is not absorbed in stoichiometric amounts(1.1). Hydrogen is absorbed easily until the number ratio c of hydrogen to metal atoms (or H/M ratio) is about 0.6. Then the chemical potential starts rising rather abruptly. Palladium will easily absorb hydrogen directly from the gas phase of H_2 at elevated temperatures(1.2), so in this case the pressure of H_2 in equilibrium with the dissolved hydrogen rises sharply after c = 0.6. This is not related to the complete filling of one particular kind of interstitial site in Pd, but to the filling of the electronic d-band of Pd by the shared electrons of hydrogen(1.2), as will be discussed below. In other cases hydrogen forms a definite stoichiometric compound with the metal, which is called a hydride as distinguished from a continuous solid solution like that in Pd. For example, $ZrNiH_x$ apparently exists as a solid solution of H in ZrNi, as the hydride for x = 1, and as a trihydride at x = 3. Hydrogen appears to have very small solubility in the mono- and tri-hydrides(1.3).

There is a considerable amount of technological interest in the hydrogenation of metals. One area of interest is in using them as an efficient (and safe) way of storing hydrogen, since in many metals it exists at a higher density than in its liquid state. Palladium, the group III, IV, and V transition metals, the rare-earths, and the actinide metals all react exothermically with hydrogen to form either stable solid solutions or hydrides. The remaining transition metals react endothermically with hydrogen. In alloys of two elements A and B where A has a higher hydrogen affinity than B, the hydrogen is commonly found to preferentially occupy sites entirely surrounded by A atoms(1.3), or even to cause a separation of the alloy into two phases, one poor and one rich in A, with the hydrogen going into the A rich phase(1.4, 1.5).

Another area of interest lies in concern over the effects of hydrogen embrittlement on mechanical structures, as in the case of fusion reactor components. This embrittlement is due partly to the large expansion of the crystal lattice, which can be of the order of a 15%-20% volume increase at c = 1(1.6). In addition hydrogen tends to concentrate itself at the apex of any cracks that have formed, due to the local lattice strain there. This in turn stresses the lattice more and promotes propagation of the crack.

Hydrogen embrittlement is actually just one result of the interaction between hydrogen and the elastic properties of the metal. When hydrogen enters a metal it occupies interstitial sites between metal atoms, rather than substitutional sites where it would replace a metal atom or fill a vacancy. As with most interstitials, each such hydrogen atom causes a local dilatation of the lattice. This of course increases the heat of solution of hydrogen in the metal, in spite of introducing strain energy into the lattice. But of perhaps more interest than this is the effective interaction that is induced between dissolved hydrogen atoms.

1.2.1 Lattice Gas

Hydrogen in crystalline metals can cause two kinds of phase transition with increasing concentration. One kind is a change in the crystal structure of the metal lattice. For example, $ZrPdH_x$ is orthorhomic at x = 0 and 3 but triclinic at x = 1(1.3), while ZrH_x is fcc around c = 1.6-1.65 and face-centered tetragonal above about c = 1.75, though it is hcp at x = 0(1.7). The other kind of phase transition involves the local density of hydrogen, not the crystal structure of the metal. Above a certain concentration which depends on temperature, a new high concentration phase can coexist with the low concentration phase at the same hydrogen pressure or activity. The upper concentration value is also a function of the temperature. These upper and lower concentrations converge as the temperature is raised until they meet at a critical point (figure 1.1).

The obvious analogy to the liquid-gas phase transition immediately leads one to look for an attractive effective interaction between the hydrogen atoms. It is now accepted that this is due to the interaction of the strain fields of a pair of hydrogen atoms(1.8). The pair can

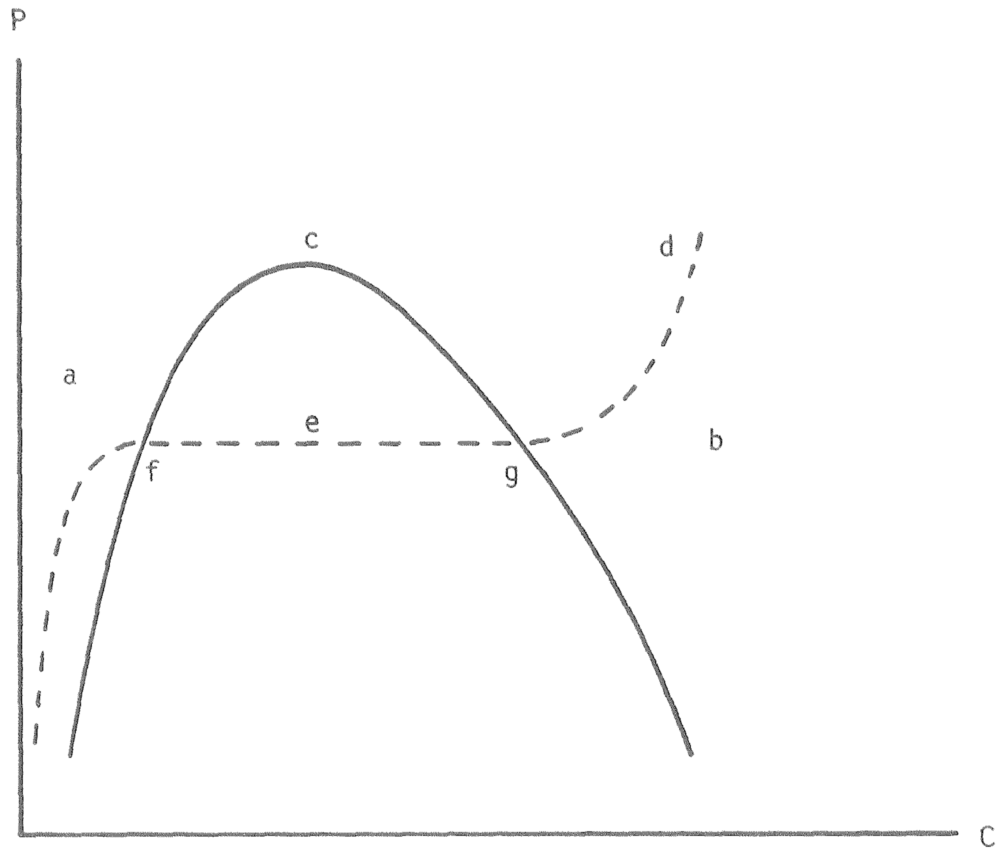

Figure 1.1 Pressure-composition diagram with an isotherm. a). Low density phase. b). High density phase. c). Critical point. d). Isotherm. e). Plateau of isotherm, in mixed phase region. f,g). Lower and upper phase limits.

lower its total strain energy by moving into proximity with each other and sharing the burden of dilating the lattice. This interaction is a long-range one. Consider the strain ε_{ij} produced by a concentration c of hydrogen interstitials (or any defects, for that matter) where c is the hydrogen to metal atom number ratio. At low defect concentrations the macroscopic strain produced will be linearly proportional to c. The strain may in general not be isotropic. Further, in a crystal there may be n_d crystallographically equivalent orientations of the defect site, each referred to by an index $\nu^{(1.9)}$. Each will be populated by a defect concentration c_ν, with

$$c = \sum_{\nu}^{n_d} c_\nu \,. \tag{1.1}$$

A defect of orientation ν produces a set of displacements $\vec{U}_k$ of the surrounding lattice atoms which initially occupy lattice positions at $\vec{R}_k$. We can describe this strain field by a multipole expansion, in analogy with the way that the field due to an electric charge distribution is characterized$^{(1.10)}$. We do this to enable the computation of the interaction energy of the local dilatation with an external stress field, for reasons that will be explained later. Since the stress is a tensor field the multipole moments will also be tensors, while in the electrostatics case the quantities are all vectors. Therefore, the two cases are not formally identical. Furthermore the strain field to be described here is not the spatially varying one due to a single defect but the uniform macroscopic expansion due to a uniform distribution of defects. Generally it is found that only the dipole term is needed to adequately describe the experimental facts. Then the multipole expansion is given by

$$\varepsilon_{ij} = \sum_{\nu}^{n_d} \lambda_{ij}^{\nu} \; c_{\nu} \tag{1.2}$$

with

$$\lambda_{ij}^{\nu} = \sum_{k} U_j^k \; R_i^k \tag{1.3}$$

where R_i^k is the position of neighboring atom k relative to the position of a defect of type ν. The indices i and j refer to Cartesian coordinates. From equation 1.2, we have

$$\lambda_{ij}^{\nu} = \frac{\partial \varepsilon_{ij}}{\partial c_{\nu}} \quad . \tag{1.4}$$

We see that λ_{ij}^{ν} is the average macroscopic strain due to unit concentration of defects in sites of crystallographic orientation ν(1.9).

Another conjugate approach to describing the same dilatation is to do a multipole expansion of the stress field (at constant, e.g., zero, strain) rather than of the strain field, in terms of the forces on atoms around a defect. These forces $\vec{f}^k$, introduced by Kanzaki(1.11), are the forces on an atom k that would be required to move it in the absence of the defect to the position that it assumes with the introduction of the defect. Here again only the dipole term is kept, and we find(1.6)

$$\sigma_{ij} = - \frac{1}{V_0} \sum_{\nu}^{n_d} P_{ij}^{\nu} \; c_{\nu} \tag{1.5}$$

with

$$P_{ij}^{\nu} = \sum_k f_j^k R_i^k \tag{1.6}$$

and

$$P_{ij}^{\nu} = - V_o \frac{\partial \sigma_{ij}}{\partial c_\nu} \tag{1.7}$$

where V_o is the atomic volume of the lattice atoms and $\underset{\sim}{P}$, the dipole moment of the force field, often called the double-force tensor, is positive. Then λ_{ij} and P_{ij} are related by

$$\lambda_{ij}^{\nu} = \frac{1}{V_o} \sum_{k\ell} S_{ijk\ell} P_{k\ell}^{\nu} . \tag{1.8}$$

The change in volume of a crystal with $c_\nu = c/n_d$ for all ν is given by

$$\frac{\Delta v}{v} = \sum_\nu \varepsilon_{ii}^{\nu} = c \cdot \text{Trace}\ \lambda_{ij} \tag{1.9}$$

where

$$\lambda_{ij} = \sum_\nu \lambda_{ij}^{\nu} . \tag{1.10}$$

Since the λ tensor is a strain tensor it is symmetric, and can be diagonalized by a spatial rotation to

$$\lambda_m = \begin{bmatrix} \lambda_1 & 0 & 0 \\ 0 & \lambda_2 & 0 \\ 0 & 0 & \lambda_3 \end{bmatrix} \tag{1.11}$$

with

$$\lambda^{\nu}_{ij} = \sum_{m=1}^{3} \alpha^{\nu}_{im} \, \alpha^{\nu}_{jm} \, \lambda_m \tag{1.12}$$

where the α_{im} are the direction cosines for the orientation ν and the λ_i are the principal values of λ along three mutually perpendicular principal axes. All orientations ν are crystallographically equivalent so they all become the same when diagonalized; only their orientations with respect to the crystal axes differ. If $\lambda_1 = \lambda_2 = \lambda_3$, the local dilatation is spherically symmetric. If this is not the case the local dilatation takes the form of an ellipsoid. In some cases more than one defect orientation will result in the same strain dipole tensor(1.9). For example, a defect composed of an interstitial-vacancy pair will be distinguishable from the original defect after the pair are interchanged by an inversion operation, but the inversion of an ellipsoid leaves it unaffected, so their two strain dipoles are degenerate. Then we introduce a symbol n_t for the number of dipole tensor orientations, with $n_t \le n_d$, and do our sums, such as equation (1.2), over tensor rather than defect orientations. As will be seen in Chapter 2, anelastic relaxation, which gives rise to internal friction, is possible only in the case of an elliptical strain dipole unless there is more than one kind of defect. The effect is proportional to the square of a difference between different principal values of λ, i.e. its ellipticity.

The change in relative lattice constant $\Delta a/a$ or volume $\Delta V/V \approx 3\Delta a/a$ mentioned above can be measured by accurate measurements of changes in the lattice parameter using x-ray or neutron diffraction. Another approach is to make measurements of length changes in macroscopic specimens using strain gauges or a vernier gauge. Since equation (1.9) indicates that the change in volume is proportional to the number of hydrogen atoms, we assign to each hydrogen atom a volume Δv equal to the change in crystal volume V_c caused by its introduction

$$\Delta V_c = n\Delta v = Nc\Delta v = \frac{V_c}{V_o} \, c\Delta v \qquad (1.13)$$

or

$$\frac{\Delta V_c}{V_c} = c \, \frac{\Delta v}{V_o} \qquad (1.14)$$

where V_o is the average volume of a metal atom. Rather surprisingly, a comparison of Δv for hydrogen in a large number of hcp, bcc, and fcc metals and alloys discloses a nearly uniform value of about 2.9 to 3 $\mathring{A}^3$ per hydrogen atom in the low concentration region$^{(1.6)}$. At high c this can fall off by perhaps 5-10%.

We are now prepared to discuss the dipole-dipole interaction between the strain fields of two interstitial atoms. It goes asymptotically as r^{-3} in an infinite crystal which shows that it is indeed a long-range interaction. If the strain field is calculated in a finite lattice the boundary conditions are changed: the surface of the crystal is free rather than being constrained by the surrounding material. The solution then is a superposition of two strain fields: that of a proton in an infinite lattice, and a solution to the homogeneous equations (no hydrogen present) that yields the expansion needed to meet the new boundary conditions at the surface. This latter strain field depends strongly on the shape of the material. Thus two hydrogen atoms or groups of atoms create strain fields that depend on sample shape, be it a sphere, rod, or foil, resulting in a shape dependence to the interaction force and hence to measurable properties sensitive to these interactions(1.8). In a mean field theory, for example, the relaxation time for diffusion takes on a Curie-Weiss form so that T_c and the diffusion coefficient $D^{*}\sim MkT(T-T_c)$ depend on the shape. This has clearly been seen in diffusion experiments where T_c for wires and foils differed by 100 K(1.8). This provides direct experimental evidence that the hydrogen-hydrogen interaction is mediated by lattice strain rather than by some other interaction.

There may also be a short-range H-H repulsive interaction in addition to the long range attraction(1.12). A minimum distance of 2.1-2.2 Å has been suggested for the H-H interstitial separation, based on band structure calculations by Switendick and on some circumstantial evidence regarding maximum solubilities of hydrogen in alloys(1.13). However this is rather speculative at this point.

These interactions between hydrogen atoms lead naturally to a Van der Waals equation of state, and in fact the metal-hydrogen system obeys the equation better than any actual gas in the region around the critical point(1.14). This system is commonly called a lattice gas.

The discontinuity in hydrogen density at the boundary between the gas-like and liquid-like phases in such a system below the critical temperature would cause a large difference in the lattice parameter if the two phases were physically separated from each other. Thus at a phase boundary the lattice parameter mismatch can easily exceed the maximum strain a crystal can support without developing dislocations. Therefore, the metal may only remain coherent, or free of dislocation, for temperatures down to a few degrees K below the critical point before the concentrations of the two phases diverge sufficiently that dislocations will develop(1.8)

1.2.2 Electronic Effects

In the low-concentration regime, it is often found experimentally that when a metal is hydrogenated from H_2 gas, the concentration is initally proportional to $p^{1/2}$ where p is the pressure of H_2. This is called Sieverts' law, and it can be derived by equating the chemical potential of hydrogen inside and outside of the metal. That of H_2 is(1.15)

$$\mu_{H_2} = \mu^{o}_{H_2}(T) + kT \ln P \tag{1.15}$$

while the chemical potential of H in H_2 is 1/2 of this. In the metal, μ_H can be represented by(1.2)

$$\mu_H = \mu^{o}_{H} + kT \ln\left(\frac{c}{1-c}\right) + \Delta\mu_H \tag{1.16}$$

where μ^{o}_{H} is the standard potential, the second term is the configurational entropy term, and the third term represents any differences between the actual chemical potential and the ideal form represented by the first two terms. Combining these, we get

$$\frac{1}{2} kT \ln P = kT \ln K + kT \ln \left(\frac{c}{1-c}\right) + \Delta\mu_H \qquad (1.17)$$

where $K = \exp[(\mu_H^o - \frac{1}{2}\mu_{H_2}^o)/kT]$ is Sieverts' constant. If $\Delta\mu_H$ is zero, at low c we get $p^{\frac{1}{2}} \approx Kc$ as claimed.

The difference term $\Delta\mu_H$ can be split into two parts, one due to the electron and one to the proton,

$$\Delta\mu_H = \Delta\mu_e + \Delta\mu_{H+} \qquad (1.18)$$

The protonic term is the energy of the expansive stress on the lattice, already discussed. The electronic term represents the rise in the Fermi level due to filling of the states by the added electrons of the hydrogen. In a rigid band model the rate of increase would just be inversely proportional to $D(E_F)$ for the pure metal. As mentioned near the beginning, in Pd this is the reason for the sharp rise of μ_H above about $c = 0.6$. Below that level the 5s band plus the very top of the Pd 4d band is being filled. At $c = 0.6$ the 4d band becomes filled and only the 5s band with sharply lower density of states is available(1.2). However in Pd metal there are only 0.36 empty states in the 4d band(1.16). Hence the rigid band model is not applicable; the addition of hydrogen modifies the band structure. In fact, what apparently happens is that the Pd 4d band remains relatively rigid, but some of the electrons contributed by hydrogen are in turn used for screening the proton. These are not totally localized, but are broadened by interaction with other bands into what looks like an extension of the broad 5s band to even lower energy; i.e., it appears that the s band has been shifted down in energy(1.2). Thus the 4d band gets filled less rapidly than expected, as does the s band after the d band is filled. Other metals have not been studied as extensively as Pd but the behavior of the electrons may be qualitatively similar.

1.2.3 Diffusion

One very important topic from the point of view of the present research is the nature of diffusion of hydrogen in metals. Below room temperature, hydrogen diffusivities in some metals exceed the diffusivity of any other atomic species. This is particularly true in the bcc hydrogen absorbing metals such as V, Nb, and Ti.

Fundamentally, as one increases the temperature from absolute zero four different regimes of diffusion are possible(1.17). At the lowest temperatures true quantum mechanical tunneling should predominate. Here the existence of a hydrogen atom in a particular energy well does not correspond to an eigenstate of the system. Instead, the interaction between hydrogen in neighboring interstitial sites will lead to a broadening of the discrete energies into bands, just as in the case of electrons in metals, and the states will be delocalized. The matrix element J for the hydrogen-hydrogen interaction is small compared to the strength of the hydrogen-lattice interaction(1.17) so the bands will be narrow. The diffusion rate will be limited by scattering due to defects and phonons. Quantum tunneling has not been seen in metal-hydrogen systems to date.

Going up in temperature, before thermal energies are sufficient to allow classical over-the-barrier hopping at significant rates a region of phonon-assisted quantum tunneling is found. The fundamental distinction between the quantum states here and those above is that the states are now localized. This is probably due to at least two factors$^{(1.17)}$. One relates to the proton-phonon interaction which limits the lifetime τ of the delocalized quantum state. When this becomes so short such that the energy uncertainty h/τ is greater than the energy width of the band given by J, the extended quantum state has lost its meaning. The other reason is that the matrix element J between hydrogen atoms in neighboring sites, and therefore the bandwidth itself, decreases with increasing temperature. This is related to the local dilatation caused by hydrogen atoms. The local expansion results in a lowering of the potential energy of the hydrogen in its site relative to its value before relaxation of the lattice, as illustrated by site 1 of figure 1.2. This does not imply that one site has a lower energy than the others in the low-temperature extended quantum state. There the dilatation and lowering of the potential energy will be spread out over all hydrogen sites uniformly. Here, however, when calculating the tunneling matrix element J one must take this relaxation into account. Neighboring quantum energy levels are no longer degenerate, which reduces J by one order of magnitude at $T = 0$ and by two orders of magnitude at room temperature, supressing tunneling$^{(1.17)}$. This further contributes to the transition from band quantum states to localized quantum states and causes the hydrogen to be self-trapped.

In contrast, phonon-assisted quantum tunneling occurs when thermal fluctuations in the metal lattice momentarily raise the energy in site 1 to the level in a neighboring site and allow quantum tunneling between

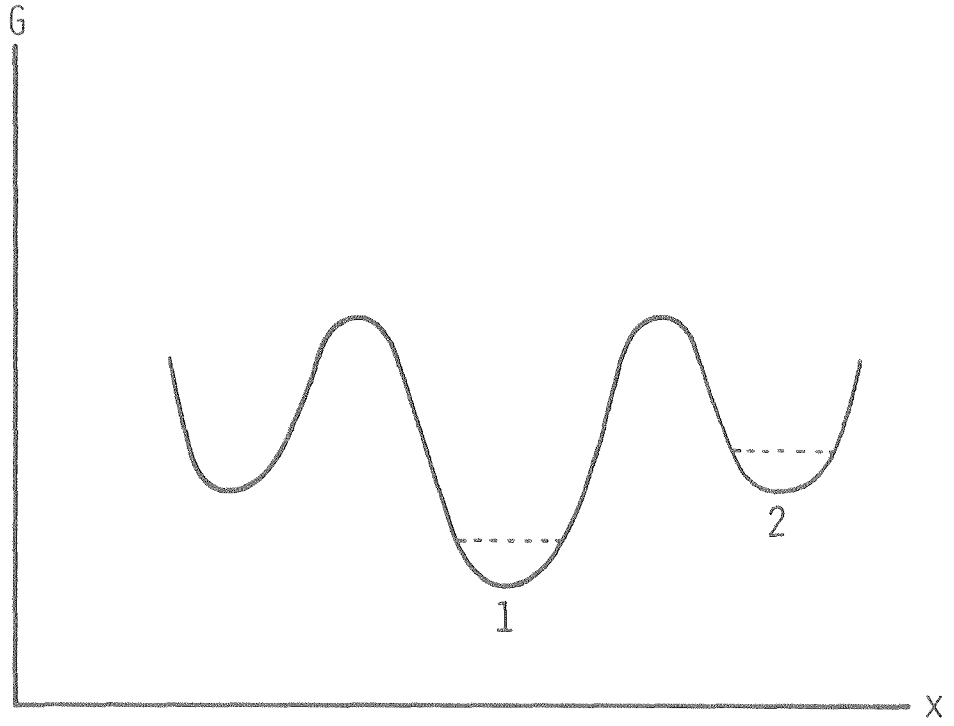

Figure 1.2 Lowering of the potential energy (i.e., self-trapping) of a hydrogen atom in site 1 relative to originally degenerate sites such as 2, due to dilatation of the lattice.

them. This is a thermally activated process with an activation energy given by the energy required to bring the quantum levels in two sites to equality. It is now becoming accepted that this is the process responsible for the very low activation energies, of the order of 50 meV, in the bcc metals at temperatures below about 250K, though it is not seen at all in other metals.

At higher temperatures yet, thermal energies become sufficient to allow classical hopping over the barrier to dominate. This is a result of the higher frequency prefactors involved, which are basically of the order of the Einstein frequency for atomic vibration of the hydrogen in the potential well of the interstitial site. We consider an atom moving from site A to a site B. Due to relaxation of the lattice all the metal atoms are affected and the configuration space involves all 3N + 3 coordinates. Following Kehr(1.17) we introduce a coordinate ξ that follows the path from A to B over the saddle point S. The results of absolute rate theory(1.18) give the jump rate Γ:

$$\Gamma = \frac{kT}{h} \frac{Z^*(\xi_S)}{Z(\xi_A)} \tag{1.19}$$

where $Z(\xi_A)$ is the partition function for the hydrogen atom at site A and $Z^*(\xi_S)$ is that for the saddle point subject to the restriction that motion is only allowed in the plane perpendicular to ξ. Inserting the free energy $G^*(\xi)$ where ξ is kept fixed, the rate is

$$\Gamma = \nu_{A\xi} \exp(\Delta s/k) \exp(-\Delta H/kT) = \Gamma_0 \exp(-\Delta H/kT) \tag{1.20}$$

where

$$\Delta S = S^{*}(\xi_S) - S^{*}(\xi_A), \qquad (1.21)$$

$$\Delta H = H^{*}(\xi_S) - H^{*}(\xi_A), \qquad (1.22)$$

$\nu_{A\xi}$ is the vibration frequency along the ξ direction at the equilibrium site, and Γ_o is the renormalized vibration frequency that is measured experimentally.

This is strictly a classical calculation and does not account for quantum effects that may be rather large since the quantum state energies are frequently larger than kT even at room temperature. A true quantum mechanical calculation of the jumping rate in the nearly-classical regime is apparently not available, though attempts have been made to correct this in an ad hoc way by replacing the partition function in equation (1.18) by the corresponding quantum mechanical version(1.17),

$$Z_A = \sum_{\nu} \exp(-E_{\nu}^{A}/kT) \qquad (1.23)$$

and

$$Z^{*}(\xi_S) = \sum_{\nu} \exp(-E_{\nu}^{*S}/kT) \qquad (1.24)$$

with eigenstates E_{ν}^{A} for states around site A and E_{ν}^{*S} at the saddle point. The states at the saddle point are calculated excluding motion along ξ, and including the potential energy difference $U_S - U_A$. We assume that there are three local vibrational modes at the equilibrium site and two at the saddle point and that these are not coupled to lattice vibrations, which are in turn unaffected by the hydrogen being at the minimum or saddle point. If these local mode frequencies are well above kT the result for cubic symmetry is

$$\Gamma = \frac{kT}{h} \exp\left[\frac{-U_S - U_A - 3/2\, h\omega_A + h\omega_S}{kT}\right] . \qquad (1.25)$$

This corresponds to calculating the activation energy by adding the difference in potential energy to the zero-point energy taking into account the decreased number of degrees of freedom at the saddle point. To be done correctly, all the calculations at the saddle point must of course take into account the local lattice relaxation that may occur as the hydrogen passes through it.

1.2.4 Local Modes

The assumption was made above that the local vibration modes are not coupled to the lattice phonons. This assumption is relatively good because the large mass mismatch between the hydrogen and metal atoms prevents the hydrogen optical modes from very strongly driving the metal atoms. For low concentrations where the hydrogens are too far apart to interact these hydrogen vibrations then become local modes(1.19). These exist in addition to the normal band modes where hydrogen is vibrating in phase with the lattice, and with about the same amplitude of hydrogen vibration.

An experiment that can detect the hydrogen optical modes is inelastic neutron scattering. Hydrogen has a very large incoherent and much smaller coherent neutron scattering cross section so that neutron scattering is sensitive to even small amounts of hydrogen and yields the local phonon density of states. Inelastic neutron scattering in crystalline hydrides can frequently be fitted to a sum of Lorentzian peaks representing the vibration frequencies along three axes in each of the hydrogen sites, with reasonably good agreement with model calculations based on knowledge of the site.

Deuterium, on the other hand, has a moderately large coherent and much smaller incoherent neutron scattering cross section, so neutron scattering results yield the structure factor for the spatial arrangement of deuterium atoms. Thus by doing elastic neutron scattering on a deuteride one gets the D - metal as well as metal - metal distance information.

In all the foregoing analysis we have assumed the existence of one or a few fairly well-defined interstitial sites, present in number comparable to N, the number of metal atoms. But as in most material problems, defects may also be important. In particular, deeper wells may exist around dissolved impurities such as oxygen or nitrogen(1.9, 1.20, 1.21), dislocations(1.22, 1.23, 1.24), vacancies or impurity metal substitutional atoms(1.25). Each of these can give rise to an internal friction peak, as will be seen later.

1.3 METALLIC GLASSES

We next turn briefly to another topic of great and fundamental interest, that of amorphous metals. These are materials that display the characteristic properties of crystalline metals but lack their long-range (crystalline) atomic order. These have been prepared in a variety of ways. Historically, the first known examples were produced by vapor deposition and electro-deposition. In 1959 Pol Duwez and associates first produced such a metal by rapid quenching from the liquid phase(1.26). In this case the resulting metal is sometimes called a metallic glass to distinguish it from other preparation methods. More recently, hydriding of a crystalline Zr-Rh alloy(1.27) and thermal treatment of a multilayer sandwich of crystalline metals(1.28) have led to the production of amorphous metals by solid-state reaction for the first time. It is generally found that alloys are much easier to make amorphous than the pure elements. The most common classes of binary glassy metals are alloys of a transition metal with a metalloid (B, C, Si, P), or of an early transition metal with a late transition metal. Ternary and more complex alloys are also common.

Frequently there is a close correlation between the range of composition over which an alloy can be made amorphous and the position of a deep eutectic in its phase diagram. This indicates a relatively large affinity of the two species for each other in the liquid state and indicates a relatively large negative heat of mixing of the liquid as compared to the crystalline structure. Also, in the case of liquid quenching this tends to give a smaller temperature difference between the liquidus line and the temperature at which the atoms become configurationally frozen, (i.e., the glass transition temperature T_g). This allows lower cooling rates to be used while still quenching the alloy to the glassy state without nucleation of crystallites. If the glassy metal is reheated to the vicinity of T_g it will normally crystallize.

1.3.1 X-Ray Diffraction on Amorphous Metals

One of the most dramatic experimental indications that a material at hand is amorphous is its x-ray diffraction pattern. Unlike the quite narrow Bragg peaks seen for a polycrystalline material, the first peak is quite broad. Further, only the first two or three peaks are discernible at all, unlike a crystalline metal where many Bragg peaks can be easily seen. Finally, the fact that no analog of a single-crystal diffraction peak is ever seen in an amorphous diffraction pattern indicates an isotropic structure with no long-range order.

The diffraction pattern of a material is a three-dimensional Fourier transform of its thermally averaged spatial electronic number density. An experimental diffraction pattern can be normalized by the X-ray scattering form factor of the atoms involved, then transformed back to give the radial distribution function (RDF). This is the average distribution of atoms around a typical atom as a function of radius r. When this is computed for amorphous metals it shows a strong primary peak corresponding to the first nearest neighbor of a given atom, with increasingly blurred peaks out to the first several nearest neighbors (see figure 1.3a). However, though in principle this contains a great deal of information about the structure of the metal, in practice surprisingly little useful information can really be gleaned from it. What is obtained from the position and area of the peak is the average distance to the nearest neighbor and the average number of nearest neighbors (the coordination number). For binary ($A_xB_{(1-x)}$) amorphous alloys, if three measurements can be made with differing cross-sections for the two component atoms, the partial RDF's for the A-A, A-B, and B-B

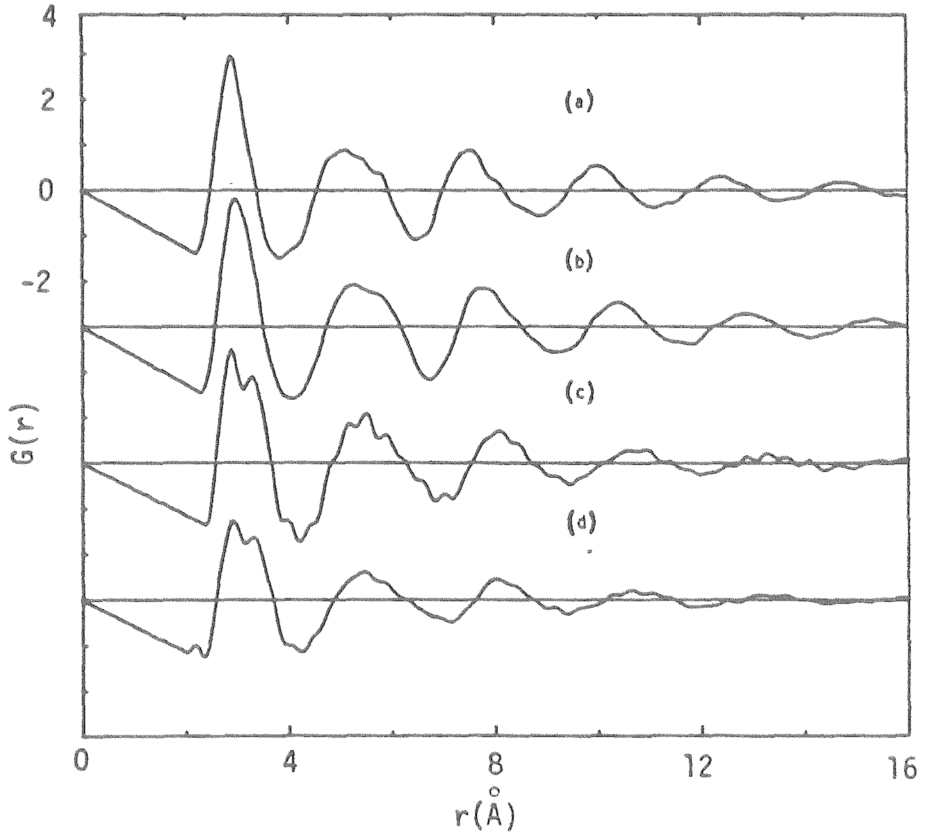

Figure 1.3 Reduced radial distribution functions $G(r) = 4\pi r[\rho(r)-\rho_0]$ for melt-spun glassy metals. a). Zr_2Pd. b). Zr_2Pd annealed for 11 h at 190 C. c). $Zr_2PdH_{2.7}$ hydrogenated in 1 atm. H_2 at 180 C. d). $Zr_2PdH_{3.0}$ hydrogenated in 25 atm. H_2 at 180 C. (Taken from ref. 1.12)

pairs can be extracted along with their coordination numbers.

1.3.2 Models

The first models for metallic glasses involved the dense random packing of hard spheres (DRPHS). More recently softer potentials combined with relaxation of the atomic positions on a computer have yielded much better fits to observed RDF's and to density measurements which give densities higher than DRPHS models(1.29). Inclusion of different atomic radii in the case of alloys and the possibility of including chemical short range order are further advantages. The topological short range order in an alloy does not completely specify the structure: the arrangement of individual atomic species on a given (random) lattice still remains to be specified, and will generally be affected by the chemical affinity of differing atoms relative to their affinity for their own species.

One of the pieces of information coming out of the models that is of particular interest for this study is a counting of the available interstitial sites in a glassy metal. One of the early DRPHS models was constructed by Bernal from steel ball bearings(1.30, 1.31). From the spatial coordinates of the centers of the balls he constructed a ball-and-stick model, and used this to study the holes between spheres. Allowing for up to 20% distortions of the polyhedra, he found he could fit them all into the five categories shown in figure 1.4. 73% of the holes were tetrahedra, 20% half octahedra, and the remaining 7% comprised the other holes. The half octahedron, trigonal prism, and Archimedian antiprism each present four-sided faces to the outside world. These can each be capped with a half octahedron just by adding another

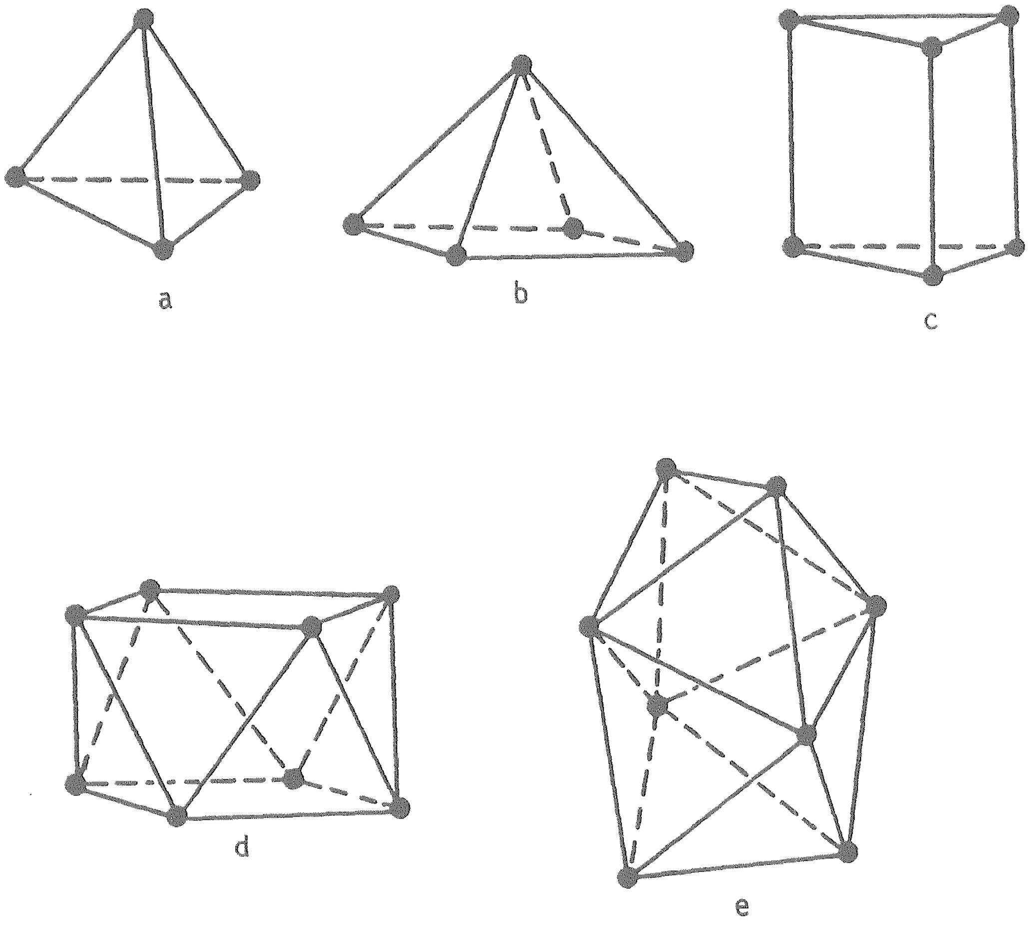

Figure 1.4 Bernal's five hole types. a). Tetrahedron. b). Half octahedron. c). Trigonal prism. d). Archimedian antiprism. e). Tetragonal dodecahedron.

vertex exterior to that face, leaving polyhedra whose surfaces contain only triangular faces. For example, doing this to the half octahedron forms a full octahedron. Arranged this way, the population percentages are 86% tetrahedra, 6% octahedra, 8% other(1.32).

More recently there has been considerable interest in the possibility that the icosahedron may form a significant structural unit in metallic glasses. The icosahedron is a regular polyhedron of 12 vertices (13 if an atom at the center is included) with 5-fold symmetry. For an isolated 13-atom cluster it is generally found to be the structure with the minimum energy. The symmetry is used to partly explain the crystallization barrier, since long-range order is incompatible with 5-fold symmetry. In a glass any icosahedra will certainly be distorted and their identification might have more to do with the eye of the beholder than with any objective criteria, since they can also be described by a collection of distorted octahedra and tetrahedra. Interestingly enough, icosahedral point group symmetry has very recently been experimentally observed for the first time, in grains of 2 μm size in a rapidly cooled Al-Mn alloy and surrounded by an fcc Al matrix(1.33). However, this has never been seen in a metallic glass.

Recently there has been an effort to quantify more objectively the types of interstitial holes in computer models using soft interatomic potentials such as Lennard-Jones or Morse potentials(1.32, 1.34), the latter being the softest. Surprisingly, it was found that the resulting distribution of interstitial sizes shows two peaks corresponding to tetrahedral and octahedral sites as shown in figure 1.5(a,b). These become more clearly differentiated as the potential becomes softer. The long tail at large radius presumably represents larger Bernal polyhedra.

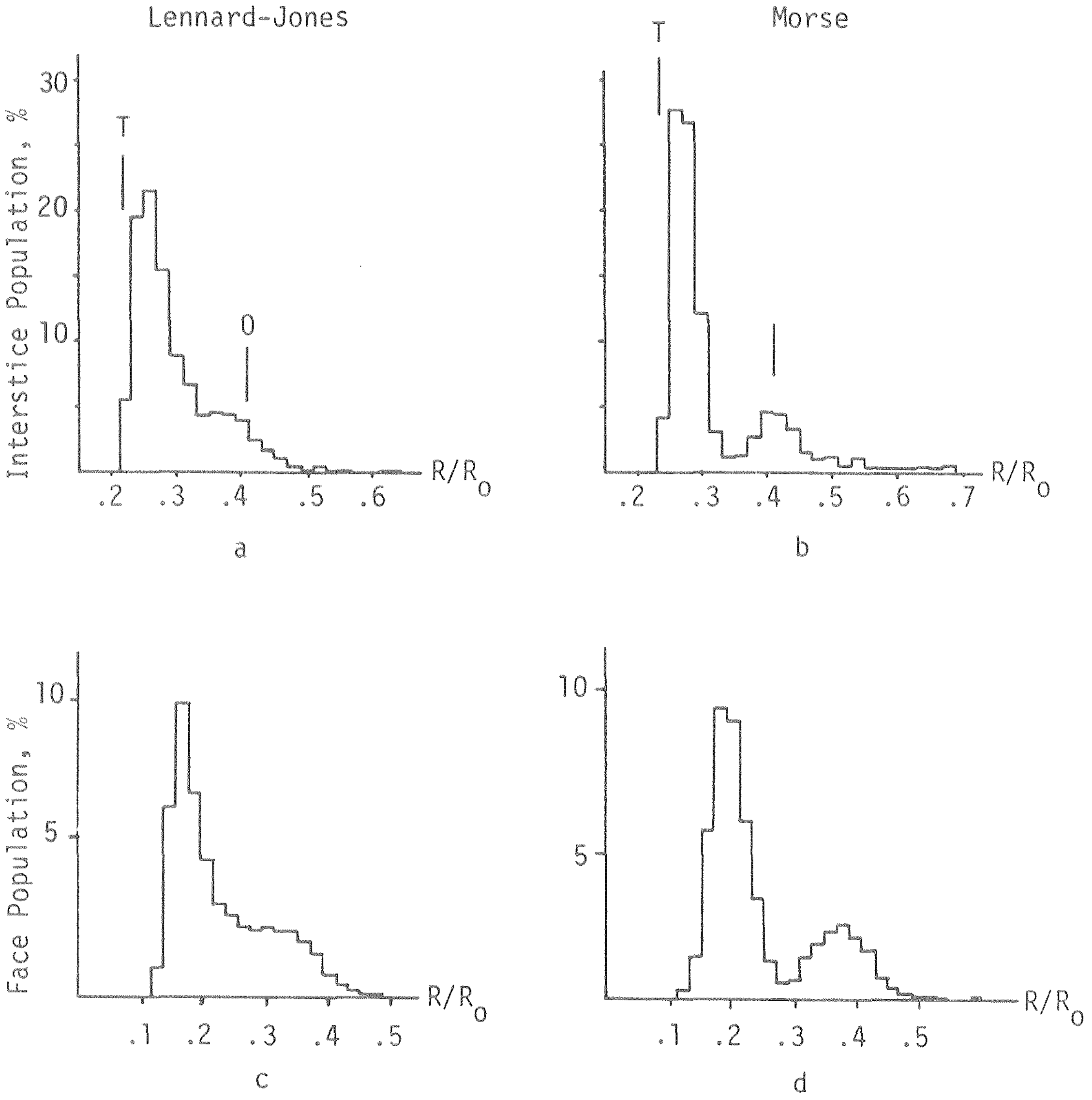

Figure 1.5 Distribution functions for radii of holes in interstitial sites (a and b) and faces (c and d) found in relaxed computer models. A Lennard-Jones pair potential was used for the models on the left, while a Morse potential was used for those on the right. "O" indicates the interstitial site radius for a regular octahedron, "T" for a tetrahedron. (Taken from ref. 1.34).

When the site-site correlation function vs. separation is computed, peaks appear that agree well with the distances calculated if regular polyhedra were connected in different possible ways. For example, two tetrahedra might be joined face to face, edge to edge while each sharing a face with a third intervening tetrahedron that joins them, or edge to edge but sharing faces with an intervening octahedron. A check for possible clusters of atoms that could be represented as a distorted icosahedron was negative.

Distributions of hole radii for the distorted triangular and square faces through which a diffusing atom must jump were also computed for these models. Again a bimodality was observed which was more extreme in the case of the softer Morse potential. These are displayed in figure 1.5(c,d).

Polk at one time proposed that in a transition metal - metalloid (T-M) glass such as $Fe_{1-x}B_x$, the M atoms might fit into the existing Bernal holes of an imagined DRPHS metal structure formed by the T atoms without disturbing it(1.35). He calculated that if the metalloid atoms went only into the three larger holes, excluding the tetrahedral and octahedral sites, the maximum value of x would be 21%, which agrees well with the composition at which it is easiest to form many of these alloys. He also showed that the density of the alloy would agree well with measured values for T-M alloys. It is not obvious why such a model should be valid since the metalloid is present at quenching rather than entering afterward and is not constrained from inducing a different initial structure, particularly in light of the strong directional nature of metalloid atoms' bonding. It was shortly pointed out that Polk had overestimated the size of the holes considerably(1.36). On the other hand, hydrogen can be introduced after quenching and is expected to go into all such sites, as will be discussed below. Thus understanding the nature of the sites is important to a study of hydrogen in amorphous metals. Conversely, hydrogen can be viewed as a microscopic probe of the structure, useful in its elucidation.

1.3.3 Modulus of Elasticity

One final property of glassy metals that is of interest here is the very large reduction in the shear modulus G compared to that in the crystalline version of the same alloy(1.37). The bulk modulus is reduced by only about 5-10% and it correlates with the atomic volume, which in amorphous metals is larger than in crystalline form by 2-3%. The bulk modulus is almost exclusively a function of atomic volume and is very insensitive to atomic-scale structure(1.38). The shear modulus, however, which typically decreases in a glassy metal to something like 75% of its crystalline value, is not associated with a volume change.

Weaire, et al.(1.39) did an early set of calculations of the bulk and shear moduli of metallic glasses, using Morse pair potentials. One simple method was to use calculated (from models) or experimental radial distribution functions to provide the interatomic distance information. The structure was then strained and the pair potential integrated over the strained RDF to provide its energy. This corresponds to moving each atom in a solid as though it were a point in an ideal homogeneous continuum. Thus there are no relative internal displacements of the atoms. The bulk moduli calculated in this way for hypothetical Cu, Al Au, and Ni pure metal glasses were 4-17% lower than in the crystal, in fairly good agreement with the results mentioned above. However, with this constraint of no internal motions the shear modulus is given by $G = 3/5\ B$ so the relative reductions in G are the same as for B.

On the other hand, in actual glasses the atoms may move to a variety of positions around the position calculated above. Several sets of about 100 atoms were taken from the interior of one of Bennet's DRPHS models by the same authors and relaxed using the chosen pair potential. These were then subjected to strains and allowed, or not allowed, to internally relax before calculating the elastic constants. With no relaxation after straining, the results were similar to those already mentioned. If relaxation was allowed, B decreased by about 3% over the unrelaxed value while G decreased by about 33%. This shows that relaxation by internal displacements nicely accounts for the low shear modulus in metallic glasses.

1.4 HYDROGEN IN AMORPHOUS METALS

Hydrogen was first introduced into metallic glasses only relatively recently(1.40, 1.41). Just on the basis of what is known about glassy metals and about hydrogen in metals one should be able to deduce at least some of the resulting properties. If hydrogen continues to exist as an interstitial it must surely go into the Bernal holes mentioned above. The fact that glassy metals tend to have a density several percent below that of the corresponding crystalline form might suggest an increased capacity for hydrogen uptake, and this has often been observed to be the case(1.42, 1.43), though it is not true for ZrNi(1.44, 1.45).

The sites occupied will clearly not all be identical; the number of metal atoms in the polyhedron forming the site, the depth of the potential energy well, the Einstein frequencies of local vibration near the minimum, the height of the activation energy barrier for hopping through the various faces of the polyhedron, the distance to and depth of neighboring wells, and the ellipticity of the site's λ tensor (as mentioned early in this chapter, and to be developed in Chapter 2) will all be different for each site. Therefore, for a macroscopic sample each of these quantities will be distributed over a range of values with some distribution function. Further, some quantities may be correlated with other quantities (e.g., well depth with activation energy).

Inelastic neutron scattering experiments on hydrogen in glassy metals have found an optic peak that has nearly the same energy as that in the corresponding crystalline alloy, but whose width is approximately twice as wide, due to the distribution of kinds of sites in the glass. In a-$ZrNiH_{1.8}$ and a-$Zr_2NiH_{4.4}$ ("a" indicates that it is amorphous) the peaks may show some structure, as does the crystalline alloy(1.46). However in a-Zr_2PdH_3 the peak, measured at 10K with much better accuracy, was much smoother and fit well to a Gaussian(1.47). The fundamental peak was centered at 125 meV with a full width at half maximum (FWHM) of 62 meV, and the second harmonic was centered at 260 meV with a FWHM of 146 meV. For a crystalline $Zr_2PdH_{1.83}$ alloy the peak was centered at 137 meV, with the atoms probably occupying Zr_4 tetrahedral sites but possibly with some Zr_3Pd tetrahedral sites involved(1.48). The similarity in peak positions suggests that hydrogen may occupy tetrahedral positions in the glassy alloy.

X-ray and neutron diffraction measurements on $(Zr_{1-x}Pd_x)(H \text{ or } D)_y$ with x near 0.33 and y near 0 or near 1 show that for $y \simeq 0$ the first maximum at about 2.90 Å in the RDF contains the Zr-Zr, Zr-Pd, and Pd-Pd partial pair contributions. As such the peak already shows some broadening. On hydriding to $y \simeq 1$ the first maximum splits into two peaks, as seen in figure 1.3(c,d). The lower peak at about 2.89 Å appears to represent Pd-Pd and Zr-Pd pairs while the upper peak at about 3.32 Å is due to Zr-Zr pairs(1.12, 1.49). Similar results were observed for $Zr_3RhH_{5.5}$ versus Zr_3Rh, with Zr-Zr pair distances in the hydrided sample being almost identical to those in hydrided Zr_2Pd. This indicates that in the glassy metal the hydrogen initially goes preferentially into sites surrounded exclusively by Zr atoms. The results of elastic neutron scattering on the corresponding deuterides should also be capable of yielding this information directly as the deuterium-metal coordination number, but the data available to date for amorphous Zr-Ni and Zr-Pd deuterides(1.49) are not of very high quality. They do indicate roughly 4-6 neighbors.

Another technique that bears information on hydrogen neighbors is soft x-ray emission spectroscopy (SXES). Results on both $Zr_{.65}Pd_{.35}H_{1.0}$ and $Zr_{.67}Ni_{.33}D_{1.0}$ as compared to the unhydrided or undeuterated alloy show a strong decrease in the Zr L_3 band peak with simultaneous growth of a substantial bump about 7 eV to the low side of the peak(1.50). In contrast there is virtually no change for the Ni or Pd bands. This reinforces the view that at $c = 1$ hydrogen is interacting entirely (or nearly so) with Zr atoms.

The expected distribution of activation energies has been seen for several alloys in NMR measurements of such things as the proton rotating-frame relaxation time $T_{1\rho}$. These measurements are sensitive to the hydrogen residency time τ_d between jumps. When $\ln \tau_d$ is plotted versus inverse temperature on an Arrhenius plot, a straight-line fit to the data (as is found in the case of the crystalline hydrides) indicates a single activation energy. The curved line found for glassy metal hydrides(1.51) indicates a distributed set of contributing activation energies. This will be discussed in more detail later. The hydrogen mobility seen in NMR measurements was also much larger in the glassy metal than in the corresponding crystalline metal.

A final observation (or lack thereof) is that to date no plateau has been seen in P-C (pressure-concentration) isotherms for hydrogen in any glassy metal(1.45, 1.52). It could be that this is because critical temperatures are low and haven't been encountered yet. On the other hand, it may be that the distributed nature of the relevant parameters (such as well depths and effective H-H interaction strengths) causes each local region to require a different critical hydrogen concentration before it reaches its own threshold for the hydrogen low density-high density phase transition. This would result in an overall smearing out of the phase transition expected for a lattice gas in the periodic potential of a crystalline metal.

II THEORETICAL BACKGROUND: INTERNAL FRICTION

The primary experimental technique employed in this research was the measurement of internal friction on thin ribbons of hydrogenated metallic glasses. The theory of internal friction will first be developed for crystalline materials where it is somewhat easier to discuss since hydrogen occupies a single kind of site. Then it will be extended to glassy alloys.

Historically, the first internal friction peak to be explained on a fundamental basis was the Snoek effect in bcc α-Fe with carbon or nitrogen impurities(2.1). It is now known that the impurity is interstitial (rather than substitutional), in the octahedral site (figure 2.1(a)). The six iron atoms around it do not form a regular octahedron. For site 1 in figure 2.1(a) the two atoms sharing the x axis are at a distance of a/2 while the four atoms at the centers of the four adjacent unit cells are at a distance of $a/\sqrt{2}$. Putting an interstitial atom into site 1 will cause a local dilatation; this has already been described in Chapter 1. Because of the irregularity of the octahedron the λ tensor for this site will have two equal principal values along the $\vec{x}_2$ and $\vec{x}_3$ directions, and a larger one along $\vec{x}_1$. Thus the local dilatation will take the form of an ellipsoid of revolution, in this case a prolate spheroid with its long axis along $\vec{x}_1$. Sites 2 and 3 are crystallographically equivalent to 1, but have differently oriented λ tensors.

Next we consider the response of this system to an externally applied strain. Experimentally, a thin strip of thickness t is bent into a slight curve as in figure 2.2(a). Traversing the sample from the inside of the curvature out, the local strain goes linearly from its

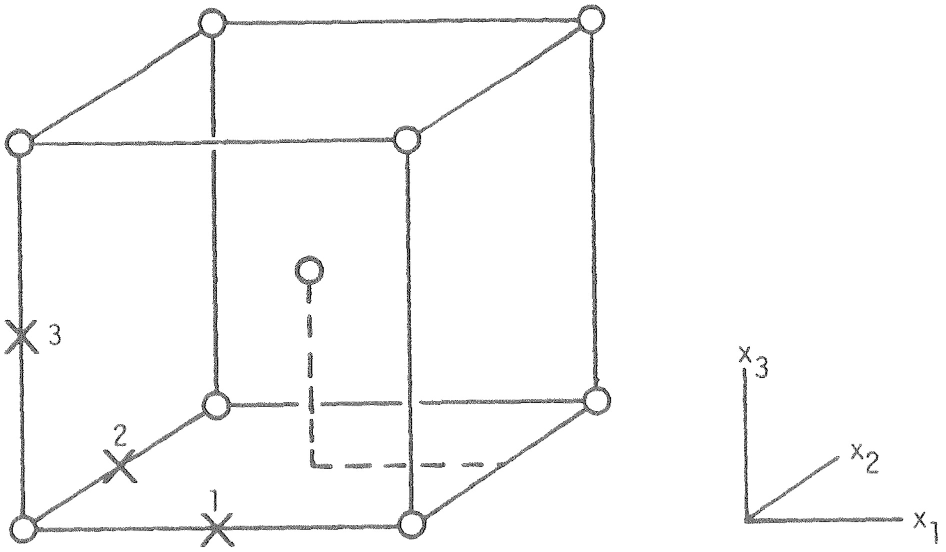

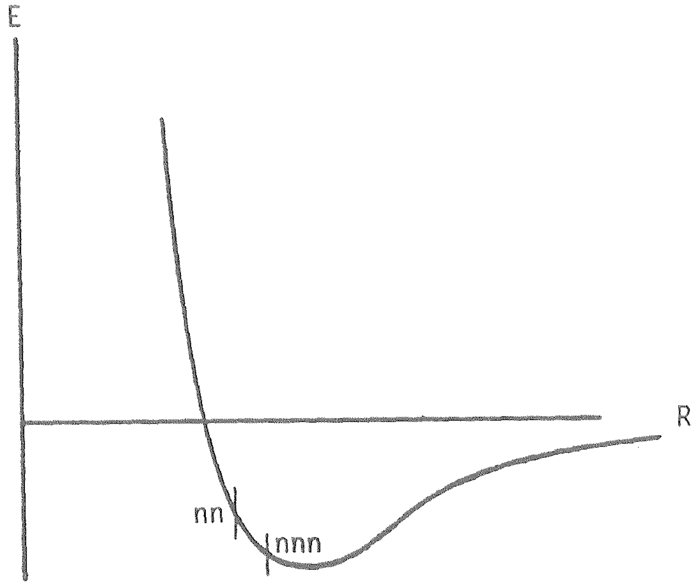

Figure 2.1 a). The three crystallographically equivalent octahedral interstitial sites in the bcc lattice, marked by x's. The lattice points are marked by circles. b). A schematic hydrogen-metal pair potential, showing the positions of the nearest neighbor (nn) and next nearest neighbor (nnn) metal atoms for an octahedral site.

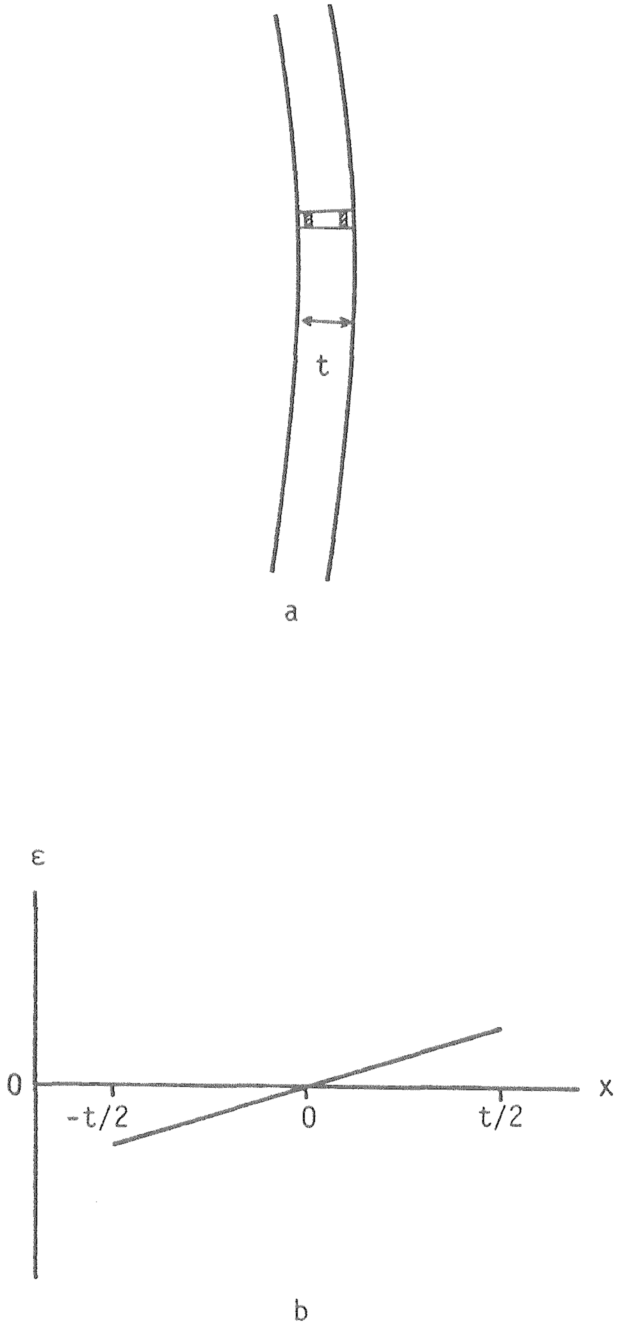

Figure 2.2 a). Edge view of a thin strip bent into an exaggerated curve. The shaded regions are small elements of volume near the inner and outer surfaces. b). The strain as a function of position in the strip.

most negative value at the inside to zero at the center, to an equally positive value at the outside (figure 2.2b). Typical maximum strains are of the order of 10^{-6} or less. In any element of volume with dimensions small with respect to t, the local stress is simply unixial, and hence is related to the strain by Young's modulus E. In other experimental designs a torsional strain can be applied, usually using material in the shape of a wire or rod, to measure relaxation of the shear modulus G.

On a qualitative level it is easy to understand the response of the interstital atoms in a particular small region of the metal to the strain. Since the $n_t = n_d = 3$ crystallographically equivalent types of sites are all degenerate in the absence of strain they will initially be equally populated. When a negative (compressive) strain ε is applied, say along axis $\vec{x}_1$ in figure 2.1, the defects of orientation (1) will have their energy raised more than will atoms in orientations (2) or (3) as shown in figure 2.3. This is due to the displacement of the nearest neighbors. To the extent that the interstitial-metal interaction can be described by a pair potential as shown in figure 2.1(b), the nearest neighbors lie on a steeper or higher-force region of that potential than do the next nearest neighbors of the octahedron. For atoms in orientation (1) it is the nearest neighbors that are moving toward the hydrogen while for orientation (2) and (3) it is the next nearest neighbors.

Now we calculate the anelastic relaxation. Since we will ultimately want to use elastic moduli rather than their inverses, the compliances, we will use the dipole moment $\underset{\sim}{P}$ of the force field rather than $\underset{\sim}{\lambda}$. To simplify the notation we will for the moment consider only a uniaxial strain ε_{11} and the corresponding stress element σ_{11}, and will

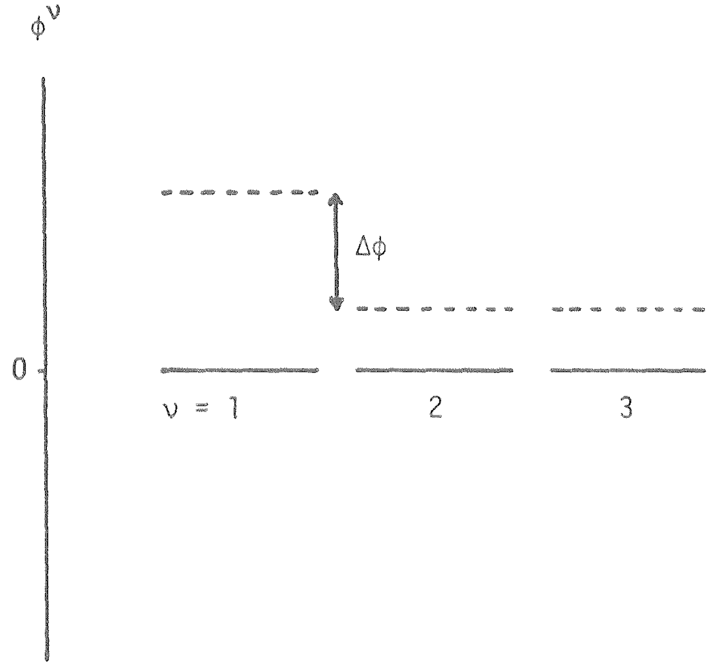

Figure 2.3 Dependence of free energy on uniaxial strain at the three octahedral site orientations in a bcc metal. ——, unstrained values, degenerate. ---, strained values.

drop the subscripts. The total stress will be the stress due to the elastic modulus plus the additional stress described by equation (1.5), resulting in

$$\sigma = M\varepsilon - \frac{1}{V_0} \sum_{\nu=1}^{n_t} p^{\nu} \left(c_{\nu} - \frac{c}{n_t} \right) \tag{2.1}$$

where M is the appropriate modulus of elasticity and the constant $\frac{c}{n_t}p$ has been subtracted so that the definition of the stress will yield a zero value at equilibrium with $\varepsilon = 0$. We see that $c_{\nu} - c/n_t$ is the deviation of the concentration of defects from its mean value for tensor orientation ν. If the defects can jump to sites of a new orientation with a time constant τ, when a change in strain changes the energy levels the concentrations will relax to new values given by the Boltzmann distribution. Thus we have an internal variable whose equilibrium value is a simple function of the external strain and which does not respond instantaneously, but relaxes to the new value with a characteristic time τ. This internal variable also affects the stress associated with the strain via (2.1), so it is macroscopically observable. The stress σ will display an instantaneous elastic response given by the first term in (2.1), followed by the relaxation to a new value given by the second term, as shown in figure 2.4.

As an aside, this general phenomenon can also result from other internal variables that couple to the strain and require a finite time τ to relax to a new value. The thermoelastic effect is one example. The strain at a point in the material in figure 2.2 gives rise to a change in temperature proportional to the thermal expansion coefficient(2.2). The strain gradient results in a thermal gradient which then relaxes in

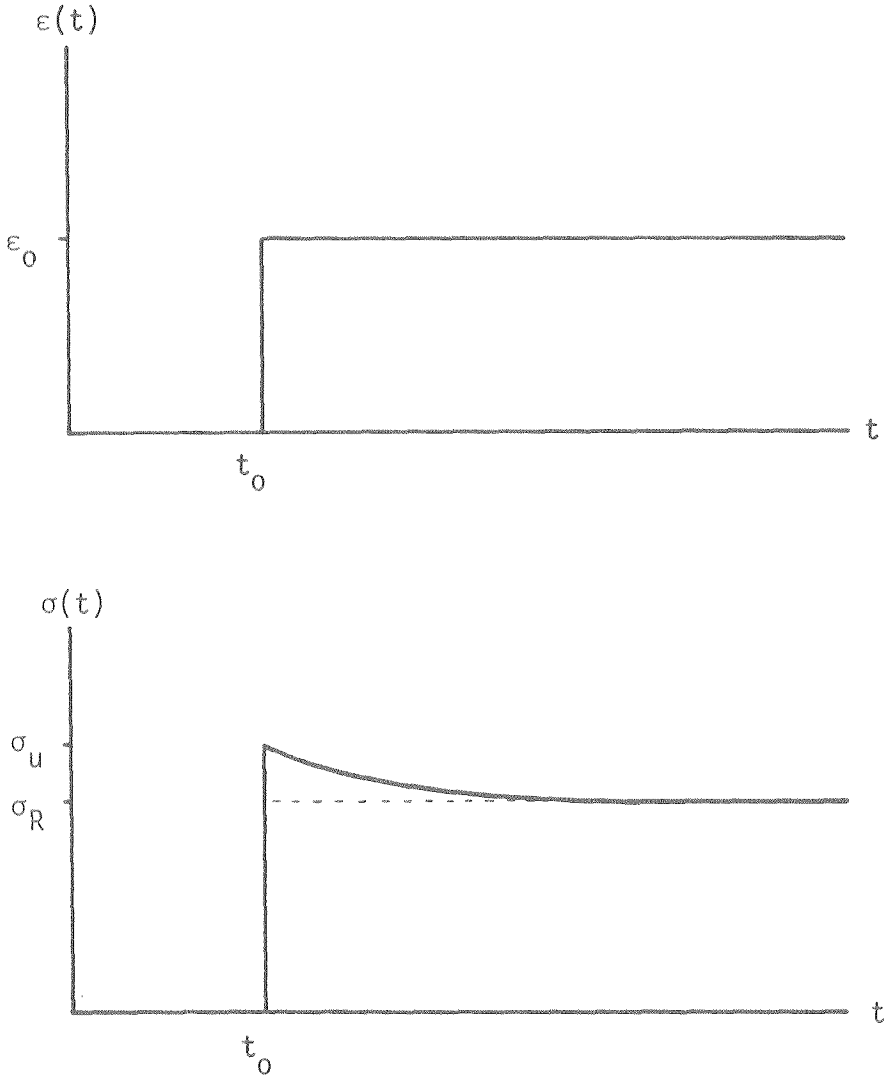

Figure 2.4 a). Application of a strain step function b). The resulting stress is initially the Hook's law unrelaxed value σ_u. This then relaxes to the value σ_R.

a time characteristic of thermal diffusion across the material. This time constant depends on the thermal diffusion coefficient D_{th}. Other examples of internal relaxations include those due to the magnetoelastic effect, grain boundary sliding, and motion of dislocations in the presence of pinning centers, as well as relaxations of point defects more complicated than those of a simple interstitial(2.2). These latter defects could be pairs of interstitial atoms (more common at higher concentrations), interstitial-vacancy pairs, interstitial-substitutional pairs, substitutional-vacancy pairs, substitutional-substitutional pairs, etc. All of these relaxations are seen in the appropriate circumstances. Any such reversible relaxation of the stress (or equivalently, the strain) to a definite equilibrium value which is a function only of the strain (or stress) and the temperature, is termed anelastic. This is to distinguish it from plasticity (which for our purposes is nearly instantaneous in response, but not reversible or linear) and linear viscoelasticity (which like anelasticity is linear and not instantaneous, but is not reversible).

Continuing now with the calculation of the anelastic part of the stress, and following Nowick & Berry's(2.2) analogous development for the strain, we write the differential of the free energy per unit volume f,

$$df = \sigma \, d\varepsilon - s \, dT - \sum_{\nu} A_{\nu} dc_{\nu} \tag{2.2}$$

where

$$A_{\nu} = - \left(\frac{\partial f}{\partial c_{\nu}} \right)_{T,\varepsilon} . \tag{2.3}$$

Then subtracting from f the contribution due to the configurational entropy s_c per unit volume

$$f' = f + Ts_c \tag{2.4}$$

and calculating the change in this modified free energy due to a defect of orientation ν, we define

$$\phi^\nu = \frac{\partial f'}{\partial N_\nu} = V_0 \frac{\partial f'}{\partial c_\nu} \tag{2.5}$$

where N_ν is the number of dipoles of orientation ν per unit volume. Then ϕ^ν is the free energy associated with having a dipole in orientation ν, including the vibrational entropy but not the configurational entropy. From (2.2) we get the Maxwell relation

$$\left(\frac{\partial A_\nu}{\partial \varepsilon}\right)_{T,c_\nu} = -\left(\frac{\partial \sigma}{\partial c_\nu}\right)_{T,\varepsilon} = \frac{1}{V_0} p^\nu \tag{2.6}$$

where the latter equality is just equation (1.7). Then since the configurational entropy in (2.4) depends on c_ν but not on ε, from equations (2.3), (2.5), and (2.6) we have

$$\frac{\partial \phi^\nu}{\partial \varepsilon} = -p^\nu \tag{2.7}$$

which is the relation we seek. The existence of a dependence of stress on defect concentration implies through (2.6) the existence of a dependence of the energy levels on strain. Integrating this for small ε, we get

$$\phi^{\nu} = - P^{\nu}\varepsilon + \phi_1^{\nu} \tag{2.8}$$

where ϕ_1^{ν} could be a function of $c_{\nu} - c/n_t$ and temperature. For small concentrations where defects are too far apart to interact significantly ϕ^{ν} should become independent of $c_{\nu} - c/n_t$ and ϕ_1^{ν} should go to zero:

$$\phi^{\nu} = - P^{\nu}\varepsilon \ . \tag{2.9}$$

Now we are ready to calculate the equilibrium population c_{ν} of defects with orientation ν. Using Boltzmann statistics we have

$$\frac{\overline{c}_{\nu}}{c} = \frac{\exp(-\phi^{\nu}/kT)}{\sum\limits_{\mu} \exp(-\phi^{\mu}/kT)} \tag{2.10}$$

Assuming $\phi^{\mu}/kT \ll 1$, an excellent approximation,

$$\frac{\overline{c}_{\nu}}{c} \approx \frac{1}{n_t}\left[1 - \frac{\phi^{\nu}}{kT} + \frac{1}{n_t}\sum_{\mu}\frac{\phi^{\mu}}{kT}\right] . \tag{2.11}$$

Inserting (2.9) we have

$$\overline{c}_{\nu} - \frac{c}{n_t} \approx \frac{c\varepsilon}{n_t kT}\left[P^{\nu} - \frac{1}{n_t}\sum_{\mu} P^{\mu}\right] . \tag{2.12}$$

We see that the change in population is proportional to the strain, the ellipticity of the double force tensor (in brackets), and the concentration, and inversity proportional to the temperature.

Now putting (2.12) back into (2.1) we get, at equilibrium,

$$\frac{\sigma}{\varepsilon} = M - \frac{c}{V_o n_t kT}\left[\sum_{\nu}(P^{\nu})^2 - \frac{1}{n_t}\left(\sum_{\nu} P^{\nu}\right)^2\right] \equiv M_u - \delta M \equiv M_R . \qquad (2.13)$$

In the second equality M has been identified as the unrelaxed modulus $M_u \equiv M_R(1 + \Delta)$ while the second term is δM, the anelastic part of the modulus, and the dimensionless relaxation strength Δ is defined as $\delta M/M_R$. The unrelaxed and relaxed moduli give the stress at $t = 0$ and $t = \infty$ respectively as shown in figure 2.4. This conpletes the calculation of the equilibrium condition.

We are now ready to consider the differential equations that describe the relaxation process between the initial and final limits just calculated. Nowick and Berry in reference (2.2) have considered a series of increasingly complex models and shown that the simplest mechanical model that exactly reproduces the behavior of an anelastic solid is the one shown in figure 2.5. It is a spring of modulus δM in series with a Newtonian dashpot of viscosity $\eta = \tau\delta M$ paralleled by a second spring of modulus M_R. Upon sudden extension the dashpot is initially not extended at all while both springs are fully extended so the modulus is $M_u = M_R + \delta M$. The dashpot then extends until the stress in the spring in series with it is zero, whereupon the modulus is M_R. The differential equation that follows is(2.2)

$$\sigma + \tau\dot{\sigma} = M_R\varepsilon + \tau M_u\dot{\varepsilon} . \qquad (2.14)$$

This can be solved to give the step response

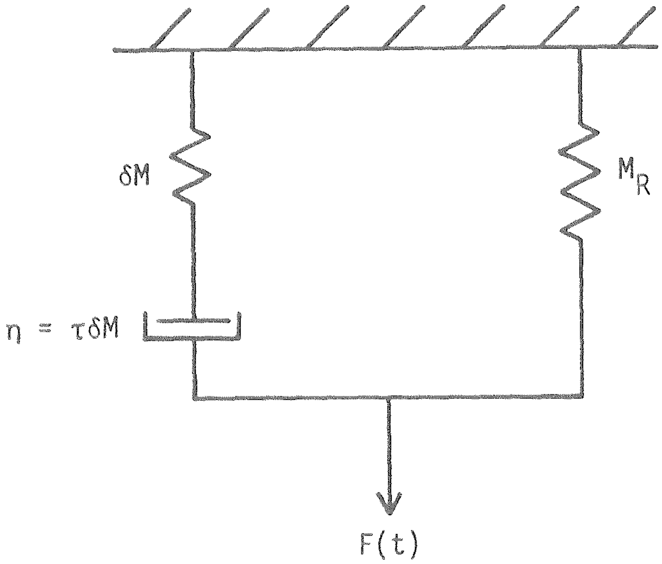

Figure 2.5 Mechanical model for the anelastic modulus. M_R is the relaxed modulus, δM is the anelastic modulus, and η is the Newtonian damping which provides a time constant τ for relaxation.

$$M(t) = M_R + \delta M \exp(-t/\tau) \; . \tag{2.15}$$

The relaxation strength $\Delta = \delta M/M_R$ is frequently small, e.g., 10^{-2} to 10^{-6} or smaller, and hence difficult to measure quasistatically with good accuracy. A better way is to make a dynamical measurement. Assume that a sinusoidal strain is applied. We expect the stress also to be sinusoidal but possibly not in phase:

$$\varepsilon = \varepsilon_0 \exp(i\omega t) \quad \text{and} \quad \sigma = (\sigma_0 + i\sigma_1) \exp(i\omega t) \tag{2.16}$$

Substituting these into (2.14) and separating the real and imaginary parts, we get $\sigma_0 + i\sigma_1 = M(\omega)\varepsilon_0$ where now we have defined a complex modulus $M(\omega) = M_1 + iM_2$. Then

$$M_1 = M_u - \delta M \frac{1}{1+(\omega\tau)^2} \tag{2.17}$$

and

$$M_2 = \delta M \frac{\omega\tau}{1+(\omega\tau)^2} \; . \tag{2.18}$$

We can understand these as follows. For $\tau << 1/\omega$ the internal variable (e.g., the interstitial atoms hopping to more favorable sites) is always nearly in equilibrium with the instantaneous value of the strain. In this limit the real part of the modulus approaches $M_R = M_u - \delta M$, the relaxed modulus. The stress almost keeps up with the strain so the out-of-phase part of the stress approaches zero. At the other extreme, for $\tau >> 1/\omega$ the internal variable barely starts to relax during one half-cycle. The real part of the modulus approaches the unrelaxed modulus M_u, while once again the out-of-phase part approaches zero because the amount of relaxation allowed during one half cycle is small. Finally, for $\tau \simeq 1/\omega$ the real part of the modulus takes an intermediate, partly relaxed value while the phase lag between ε and σ reaches a maximum. Hence M_2 reaches its maximum value of $\delta M/2$ at $\omega\tau = 1$. A peak with the form of equation (2.18) is called a Debye peak and is shown in figure 2.6(a). M_1 is shown in figure 2.6(b). It decreases by δM in passing through the region where $\omega\tau = 1$. Note that this region of decrease is narrower than the width of the M_2 peak. M_1 and M_2 are not independent. Each contains all the information about the anelastic part of the modulus, and they are related by Kronig-Kramers relations$^{(2.2)}$.

For a resonant system composed of a mass and a spring with an anelastic component, the imaginary part of the modulus mimics almost exactly the effect of the damping term in a damped harmonic oscillator. The latter has the differential equation

$$m\ddot{x} + \gamma\dot{x} + Mx = F(t) \quad . \qquad (2.19)$$

Inserting $F = F_o e^{i\omega t}$ and $x = x_o e^{i\omega t}$, this gives

$$\left[(-\omega^2 + \omega_o^2) + i\frac{\omega\omega_o}{Q}\right] x_o = F_o/m \qquad (2.20)$$

where $\omega_o^2 = \frac{M}{m}$ and $\frac{\omega_o}{Q} = \frac{\gamma}{m}$. For an anelastic spring and no Newtonian damping, we have

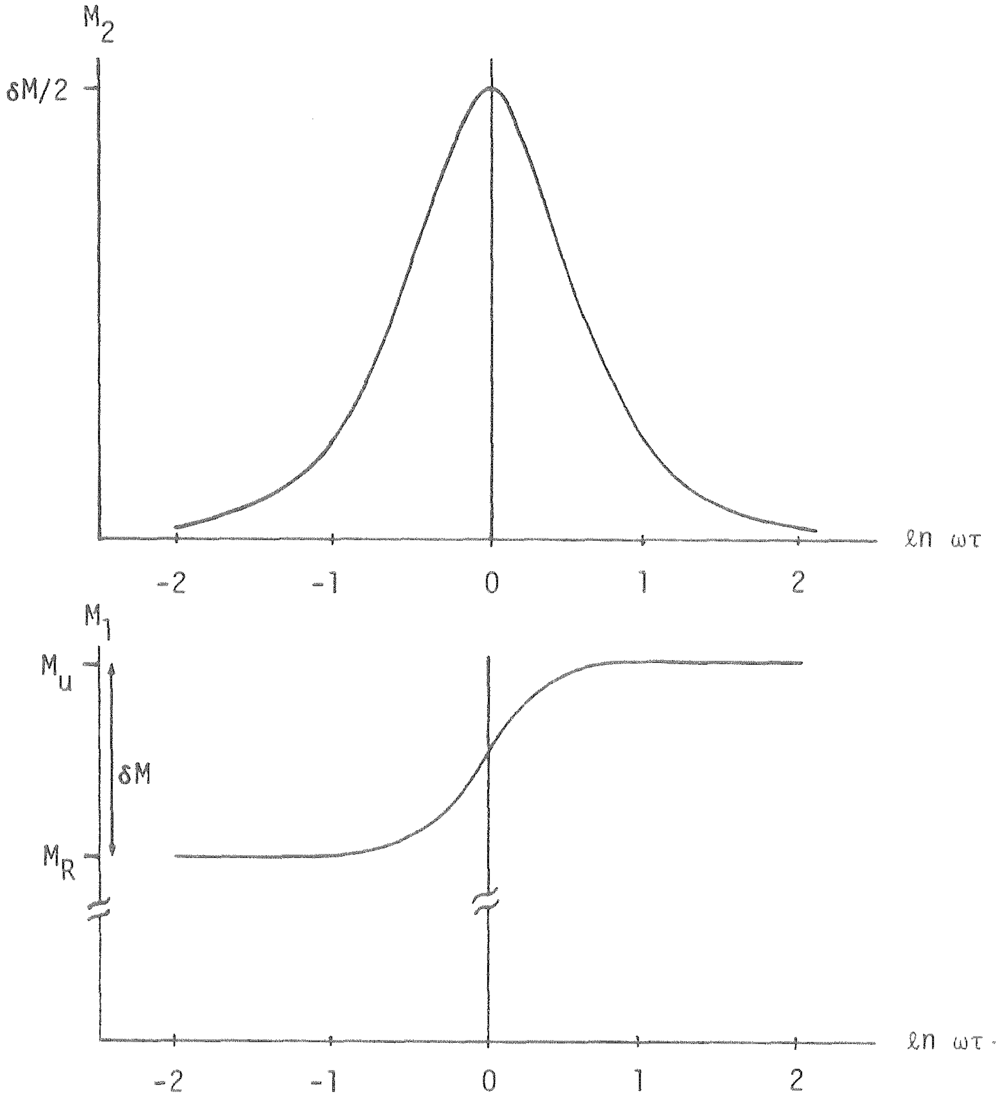

Figure 2.6 a). The imaginary part M_2 of the modulus versus ln($\omega\tau$). b). The corresponding dispersion in the real part M_1 of the modulus. For a thermally activated process the abscissa can be replaced by 1/T, to within the scaling factor E_a/k.

$$m\ddot{x} + (M_1 + iM_2)\, x = F(t) \qquad (2.21)$$

giving

$$\left[(-\omega^2 + \omega_o^2) + i\,\frac{\omega_o{}^2}{Q}\right] x_o = \frac{F_o}{m} \qquad (2.22)$$

where in this case

$$\omega_o^2 = \frac{M_1}{m} \quad \text{and} \quad \frac{\omega_o^2}{Q} = \frac{M_2}{m}\,. \qquad (2.23)$$

For small Q^{-1} these are almost indistinguishable. The phase lag of the response causes an energy loss proportional to the imaginary part of the modulus. As was just pointed out this loss term is a function of $\omega\tau$ and peaks at $\omega\tau = 1$, while ω_o is also a function of $\omega\tau$ and goes through a decrease near $\omega\tau = 1$.

In internal friction measurements the mass of the material itself is used or else an additional mass is introduced, to create a resonant system. Efforts are made to eliminate damping from any other sources such as air or the clamping mechanism that holds one end of the specimen. In the vibrating reed method depicted in figure 2.2(a) no added mass is normally used, allowing excitation of the first several flexural modes having 0, 1, 2, ..., nodes beyond the clamped end. Frequencies range from perhaps 50 Hz to 10 KHz or more. In a torsion pendulum a mass is added to a wire to establish a single frequency of vibration, typically of the order of 0.1 to 1 Hz.

In either case two methods are available to measure the relaxation strength Δ. The system can be driven into oscillation, the driving force removed, and the free decay of oscillation observed. Alternatively, from (2.22) we see that the steady state response to the driving force is

$$x(\omega) = \frac{F_0}{m} \frac{\omega_0^2-\omega^2 - i\omega_0^2/Q}{(\omega_0^2-\omega^2)^2 + \omega_0^4/Q^2} . \qquad (2.24)$$

The imaginary or 90° part of this expression is an approximately Lorentzian peak that can be measured and fitted to values of ω_0 and Q^{-1} to yield the elastic and anelastic moduli. The measurements in the present work were made in this way. As an alternative to internal friction, another common type of measurement is ultrasonic attenuation. Here a sample is driven at ultrasonic frequencies at one end and the loss term is measured from the attenuation of the vibration amplitude with distance along the specimen.

Next we consider the specific case of a thermally activated time constant for relaxation, $\tau = \tau_0 \exp(E_a/kT)$, the inverse of equation (1.20). Writing the imaginary part of the modulus in terms of $\ln \omega\tau$, it then becomes

$$M_2 = \frac{\delta M}{2} \operatorname{sech}(\ln \omega\tau) = \frac{\delta M}{2} \operatorname{sech}(\ln \omega\tau_0 + E_a/kT) . \qquad (2.25)$$

In this case the peak could be traversed experimentally either by varying ω or by varying τ via the temperature. From an experimental point of view the latter is usually much easier since only discrete (and widely spaced, in the case of a vibrating reed) values of ω are available without changing the dimensions of the sample under study. When plotted versus 1/T (figure 2.6), M_2 is symmetrical about the point where $-\ln \omega\tau_o = E_a/kT$, with a width inversely proportional to E_a. Since in an experiment both E_a and τ_o are unknown and of interest, at least two sets of measurements are needed to allow their computation. Q^{-1} must be measured versus temperature for two or more discrete frequencies ω. Then, since at the peak $\omega\tau = 1$, one could plot $\ln \omega = -\ln \tau_o - E_a/kT_{peak}$ versus $1/T_{peak}$. The slope gives E_a and the intercept gives τ_o. However this is very wasteful of the data since only the peak value is being used. It is better to use all of the data, as will be discussed in Chapter 4. Furthermore, the position of a peak is always difficult to estimate accurately from experimental data, and calculated values of τ_o and E_a depend very sensitively on the (relatively small) shift in peak temperature.

Now in general it may be the case that more than one relaxation is present, each possibly with its own relaxation strength δM and relaxation time τ. For n relaxations the complex modulus $M(\omega)$ is then given by(2.2)

$$M_1 = M_u - \sum_{i=1}^{n} \frac{\delta M_i}{1+(\omega\tau_i)^2} \tag{2.26}$$

and

$$M_2 = \sum_{i=1}^{n} \delta M_i \frac{\omega\tau_i}{1+(\omega\tau_i)^2} \tag{2.27}$$

where for the thermally activated case $\tau_i = \tau_{oi}\exp(E_{ai}/kT)$. Each term in the sum in (2.27) produces its own Debye peak, which will be clearly separated from the others only if its time constant τ is separated from the other peaks' time constants by a ratio of the order of the width of a Debye peak. The Debye peak's full width at half maximum (FWHM) is given by $\tau_+/\tau_- = (2 + \sqrt{3})^2 = 13.9$, where $\tau_\pm$ are the values at the upper and lower half-amplitude points.

In a single-crystal sample substantially more information is available from the symmetry properties of the defects$^{(2.2)}$. In order to have anelastic relaxation the defect symmetry must be lower than the crystal symmetry which it breaks, allowing more than one orientation of the strain dipole tensor. Thus a defect with cubic symmetry (i.e., a spherical dipole tensor) can not be detected by internal friction, and a tetragonal defect can be detected only if it exists in a cubic crystal. Furthermore, even a defect of lower symmetry than the crystal may have certain directions about which all defect orientations are symmetrical. A strain along that axis then affects them all equally, leaving them degenerate in energy. Finally, a spherically symmetric strain field (uniform compression) will not split the energy levels of any defect type: the bulk modulus cannot have an anelastic component if only one defect type is present.

In general the angular dependence of the anelastic relaxation strength can be computed by simply putting the equivalent of equation (1.12) for the stress dipole tensor into the full tensor form of equation (2.13). Then by measuring the anelastic relaxation strength as a function of orientation with respect to the crystal axes the defect symmetry can be deduced. In fact it is usually sufficient just to measure it along two or three high-symmetry directions. Nowick and Berry present in reference (2.2) the selection rules along important symmetry axes for defects of each symmetry system occurring in each crystal symmetry type.

We see from equation (2.13) that internal friction gives a measure of the shape factor $\sum_{\nu}(P^{\nu}_{ij})^2 - (\sum_{\nu}P^{\nu}_{ij})^2 = \sum_{\nu}(P^{\nu}_{ij}-\overline{P}_{ij})^2$, which reduces in each particular case to an expression involving squares of differences of the principal values P_i, such as $(P_1 - P_2)^2$ or $(P_1 - (P_2 + P_3/2))^2$, etc. Hence the data can only give the magnitude and not the sign of these differences. We have seen in Chapter 1 that measurement of the change in lattice parameter with concentration yields the trace of λ, and therefore $\mathrm{Trace}P = P_1 + P_2 + P_3$ through equation (1.8). Frequently with a knowledge of the defect site the sign of the shape factor can be guessed. If so, putting this information all together can give numerical values for the principal values of the strain dipole tensor.

In metallic glasses, of course, the above single crystal symmetry measurements are no longer possible, and in general as already mentioned in the case of hydrogen interstitials the well depths, activation energies for hopping, values of τ_o, and size and ellipticity of the strain dipole tensor will all be distributed quantities. The sums in equations (2.26) and (2.27) will be replaced by integrals over the distributed quantities. Because the overall size of the strain dipole tensor as well as its degree of ellipticity are variable, even sites such as regular octahedra with a symmetric tensor will contribute to internal friction. Two such adjacent sites with different values of λ would experience different changes in their potential energy with strain and contribute to the anelastic relaxation.

Internal friction peaks due to hydrogen have been seen in both metal-metalloid and metal-metal glasses in recent years, and have in each case shown a peak 2-4 times broader than a peak due to only one Debye peak, with a much broader tail on the low-temperature than the high-temperature side(2.3). This can be explained by a distribution of relaxation times with a shape crudely similar in form to that of the internal friction peak. The question then is whether this distribution is due to a distribution in τ_o or E_a. This will be discussed in detail in Chapters 4 and 5.

Brief mention should be made here of the Gorsky effect, for it is a very useful technique that is closely related to internal friction measurements of point defect relaxations. The latter measure the shape factor or ellipticity of the dipole strain field and involve "local" reorientation of the defect, where local in this case means that the defect moves only by distances of the order of the lattice parameter in the process of reorienting. On the other hand, the Gorsky effect depends on the overall size or trace of the dipole strain field and involves long-range diffusion. Typically a rod or foil-shaped sample is subjected to a constant bending strain. The uniaxial strain gradient across the specimen has a pure dilatational component which causes a gradient in the chemical potential. Relaxation occurs by diffusion of the defects from one side of the sample to the other. Relatively rapid diffusion is required even for very thin samples in order to allow a reasonable measuring time, so this has been used mostly on hydrogen in metals.

III APPARATUS AND EXPERIMENTAL TECHNIQUES

3.1 SAMPLE PREPARATION AND HYDROGENATION

3.1.1 Apparatus

The apparatus used for introducing hydrogen from the gas phase into amorphous Zr_2Pd ribbons is shown in figure 3.1. It is not sophisticated but since it worked well for the present alloy it was not upgraded. The cold trap was used to remove impurities from the H_2 gas, though this does not help with O_2 or N_2, which were present in the bottled H_2 gas at less than 5 ppm. The pressure gauge was a large dial gauge with a sensitivity of better than 0.2 torr. The pump used was a small mechanical vacuum pump which was run continuously when the system was not in use to keep outgassing rates down. The valves were Circle Seal O-ring stopcock type valves, whose original O-rings were replaced by ones of superior hydrogen imperviousness. The plumbing was all soldered copper tubing except for the specimen holders, which were made of pyrex or quartz glass and were connected to the rest of the system with an O-ring flange joint. The furnace was a vertical electrical furnace which could be moved down and away from the specimen holder to let it cool. The outgassing rates were typically such that the pressure due to extraneous gases rose by about 5×10^{-2} torr/day. At this rate, and especially if a rough correction was made, the slow increase in pressure did not cause an appreciable error in the calculation of hydrogen uptake by the metal.

The furnace temperature was controlled to within about ±1 K. The vertical temperature profile in the furnace was measured. It had a maximum near the center of the furnace, with a region 3 cm long over

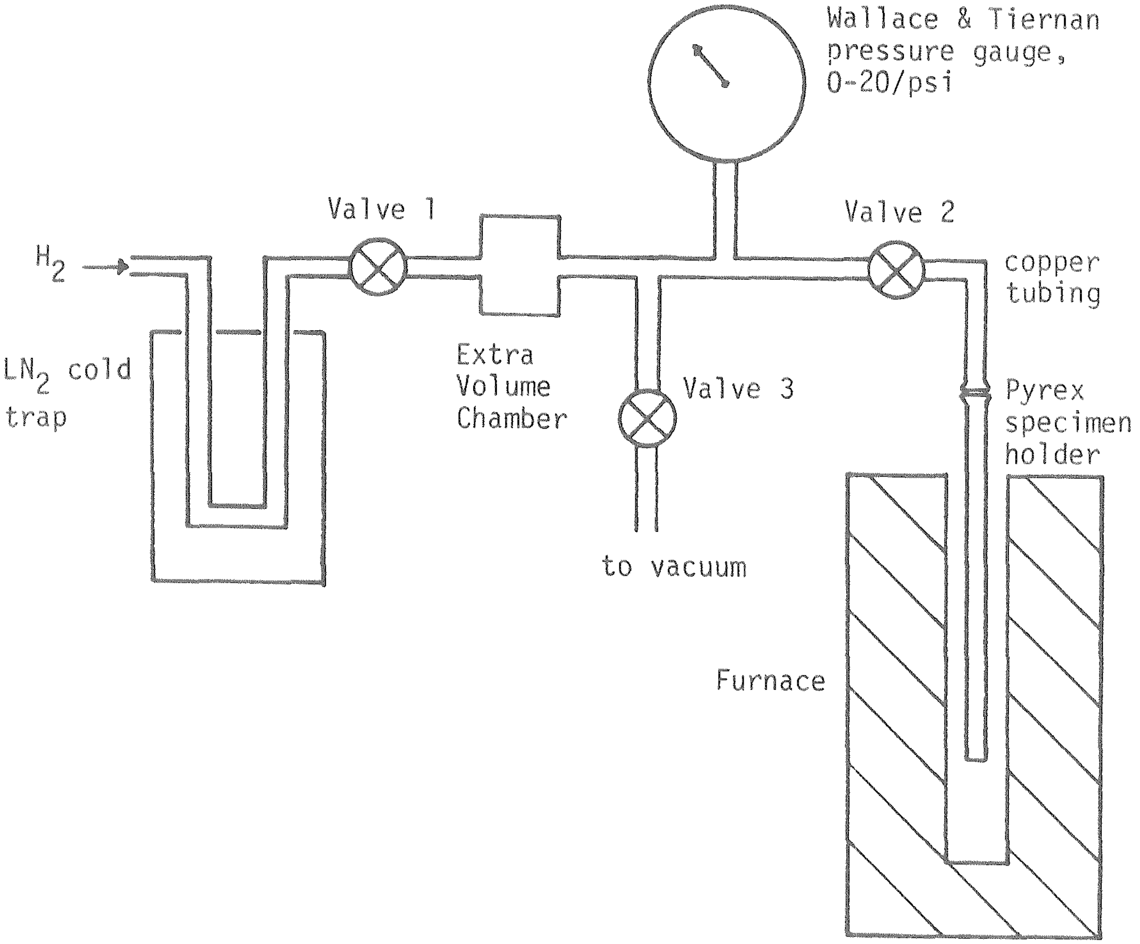

Figure 3.1 The hydrogenation apparatus.

which the temperature variation was ±1/2K. The sample holder was adjusted to hold the samples, which were usually 1-2 cm long, centered at the maximum.

In order to measure pressure vs. composition (P-C) isotherms, H_2 gas was introduced into the apparatus with the sample either at room temperature (T_r) or at the temperature of the furnace (T_f). The volume of the system was known, so pressure and temperature readings yielded the quantity of hydrogen. Then the metal was allowed to absorb the gas until equilibrium was reached, whereupon the quantity of remaining H_2 gas was measured. The difference divided by the amount of metal gave the concentration, and this was plotted vs. the equilibrium pressure. Then more hydrogen was introduced and the above measurements repeated. In this way a set of points on the P-C diagram was obtained for that temperature. For amorphous Zr_2Pd the uptake of hydrogen was limited by the condition of the surface. The rate of uptake was always initially relatively slow, and increased by many orders of magnitude as further absorption and/or desorption occurred. This is commonly the case for Zr alloys(3.1). Further, just cleaning the surface with methanol in an ultrasonic cleaner significantly reduced the hydrogenation time.

The details of the procedure are only slightly more complicated than just described. In order to measure the pressure accurately it must be constant, necessitating very slow uptake of hydrogen, or measurement before introducing it into the specimen chamber. The former was usually feasible with the sample at 200 C only when first introducing hydrogen. Later, after the surface became activated, the absorption rates became very high, in one case so high that a new charge of hydrogen would be absorbed in 2-3 sec., and absorption was visible on the gauge even at room temperature. Therefore, valve number 2 in figure 3.1 was introduced and the total volume V_T and the chamber volume V_c (beyond the valve) measured. Then, before introducing a new charge of gas, the existing gas quantity in the chamber was calculated, valve #2 was closed, more gas was introduced into the gauge side and measured, and the quantity of gas in the new charge added to that in the chamber.

A second complication arises from the fact that it is necessary to keep the sample at T_f while making the pressure reading for the P-C diagram, for use both as the pressure value on the diagram and in calculating the amount of hydrogen just absorbed. If this reading were made at room temperature the properties of the isotherm at T_f would not be measured. In order to calculate the quantity of gas present in the apparatus the detailed temperature profile would be needed. However, the assumption was made that the profile had a shape independent of the values of T_r and T_f but that it was proportional to them. Then the pressure with the chamber at T_f was calibrated against the pressure at T_r to check the above assumption, which was found to be good in the temperature range of interest. Mathematically this is just equivalent to having a certain volume at T_f, and the remainder at T_r.

A final correction had to be made due to the fact that the volume in the pressure gauge changed significantly with pressure. This functional dependence was measured by using a fairly large chamber, filling the total volume with gas, isolating the chamber with valve # 2, pumping out the gauge side, then opening the valve and reading the new lower pressure. This gave the ratio of V_T to V_C. Repeating this process gave V_T versus pressure. Programs for the calculation of various quantities from other quantities were written for a hand-held calculator.

All the actual hydrogenation of samples was carried out at 200 C to maximize the rate of absorption while avoiding crystallization, which may occur at 215 C in a-Zr_2PdH_3(3.2). For the present study only the isotherm at 200 C was measured since it did not show any interesting behavior such as a plateau like that seen in crystalline metal-hydrogen systems, though this fact is of interest in itself and will be discussed later. The isotherm is shown in figure 3.2. The pressures were too small to measure with the present apparatus up to C = 0.73, a result consistent with other Zr alloys with their large negative heat of mixing with hydrogen(3.3). The isotherm was used to predict the amount of gas needed to hydrogenate a sample to a given concentration, while having enough gas left over to supply the equilibrium pressure.

3.1.2 Samples

The a-Zr_2PdH_x samples that were used for internal friction were made by the melt-spinning method. Briefly, the molten alloy is squirted under pressure onto a rapidly spinning copper wheel, where it forms a thin layer. The cooling rate, of the order of 10^6 °C/s, is sufficiently high to bring the liquid below the glass transition temperature before crystallization takes place. The resulting ribbon is typically approximately 40 μm thick, 1-2 mm wide, and can be many meters long. The ribbons were all checked by x-ray diffraction for the presence of any crystallization, and only completely amorphous specimens used. They were then held flat in a clamp between pieces of glass to prevent curling, and hydrogenated. Finally they were checked again to make sure that no crystallization had occurred. The initial sample used was not hydrogenated at all, though it was annealed three hours at 200 C in

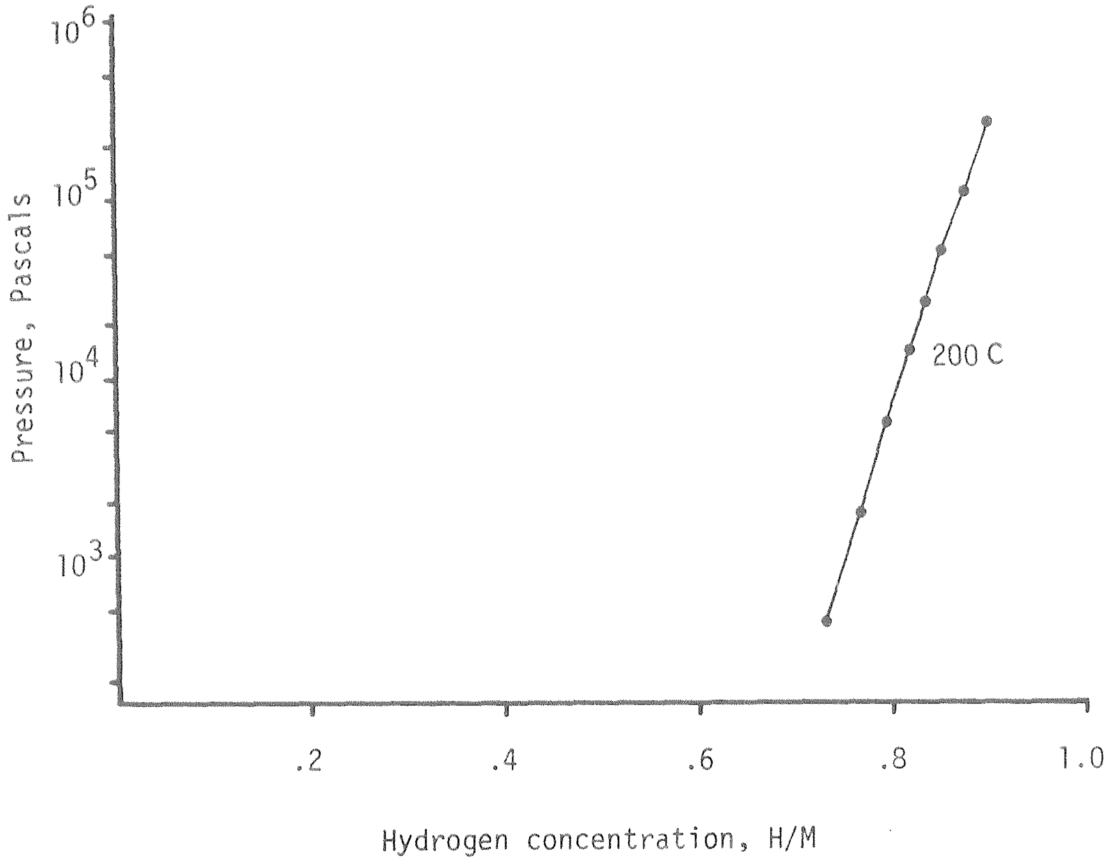

Figure 3.2 Pressure versus concentration isotherm at 200 C for hydrogen in amorphous Zr_2Pd for pressures below 1 atmosphere.

vacuum after having been stored in air for about 3 months.

After an internal friction peak was seen in this sample the decision was made to hydrogenate further samples and observe the behavior of the peak. This showed, as has been the case with internal friction peaks in other unhydrogenated amorphous alloys(3.4, 3.5), that the peak was due to hydrogen. It may be that it was already present as an impurity in the Zr or Pd parent metals, was introduced in the alloying or melt-spinning process, or was absorbed from the air afterward.

The Zr_2PdH_x internal friction specimens each came from different ribbons. They were prepared at concentrations of 0.23, 0.64, and 0.86 H/M. The $c = 0.23$ and $c = 0.64$ ribbons were made from high purity (99.999%) Zr and Pd starting metals. Normally two or three strips about 1.5 - 2 cm in length were used. This was done both to raise the hydrogen pressures needed for these small samples, thus improving the relative accuracy of pressure measurement, and to ensure a better choice of sample in the common event that significant curling occurred in spite of the clamping procedure. In the case of the 0.23 concentration the two 1.5 cm strips were cut from a 3 cm piece of ribbon before hydriding. Soon after hydriding them it was realized that this was a mistake because for this concentration the equilibrium pressure is very low. If one sample were to start absorbing before the other and take up more than its share of hydrogen, there would be no effective way for equilibration to occur by hydrogen transfer from one to the other. However, DSC and x-ray diffraction measurements carried out following the internal friction measurements showed that the hydrogen concentrations in the two samples were approximately equal(3.6). Nevertheless, the concentration for this sample is slightly uncertain, to the extent of

±1 at. %.

The c = 0.86 sample was exposed to air for 1 minute at 200 C after hydrogenating in an attempt to inactivate the surface and seal in hydrogen. Internal friction measurements on a particular vibration mode of this sample repeated several months later agreed with each other to a fraction of a percent, the normal error level. This shows that no hydrogen had escaped in spite of the fact that the H_2 gas pressure in equilibrium with this concentration is 0.14 atm at 200 C and roughly 0.10 atm at 25 C. This exposure to air was not repeated for the c = 0.64 and c = 0.23 specimens hydrogenated later because their equilibrium H_2 pressures are exceedingly small. All the specimens were hydrogenated at 200 C for a period of several days.

The $Y_{64}Fe_{36}$ samples were made by the piston-and-anvil technique(3.7) as 1-2 cm diameter foils. Strips were cut from the center of each foil for internal friction measurements. The surface was sanded with fine sandpaper to relieve surface stresses which otherwise caused the specimens to curl with time and thermal cycling.

3.2 INTERNAL FRICTION APPARATUS

The internal friction apparatus is shown in figure 3.3. The specimen, almost 2 cm in length to leave about 1.3 cm hanging free, is clamped between the two halves of a stainless steel clamp machined to have sharp, clean corners at the point where the specimen emerges. This is to minimize any losses that may occur due to friction at the clamping point. Three spring washers were used below the head of each of the two stainless steel cap screws that clamp the two halves together. The screws were tightened to the point where the spring washers were

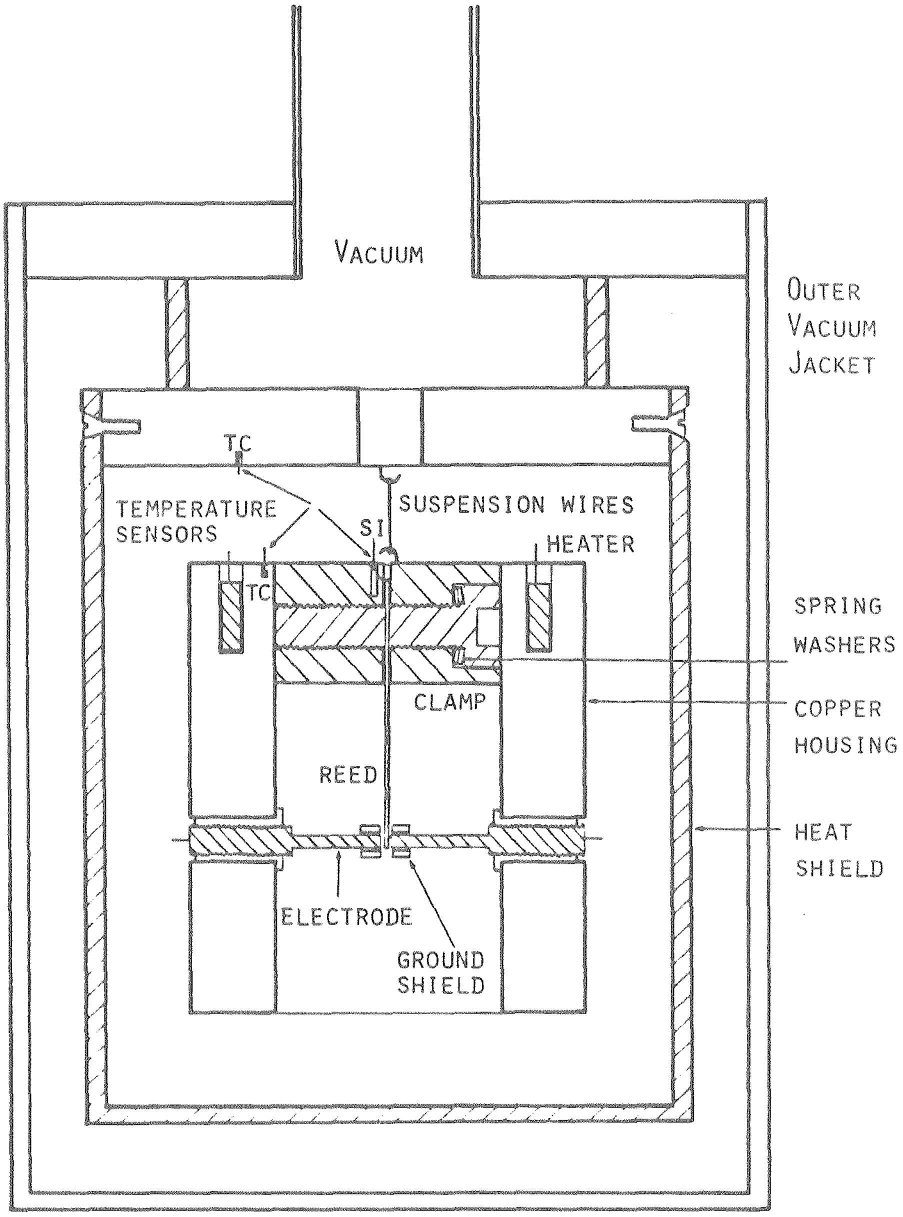

Figure 3.3 Vertical cross section through the bottom end of the internal friction probe. The two temperature sensors marked TC are thermocouples used to measure the temperature difference between the copper housing and the heat shield. The temperature sensor marked Si is a silicon diode sensor used to control the sample temperature.

completely flattened, then released about 1/4 turn. This provides a clamping force which is relatively constant over the several hundred degree temperature range of measurement. If springs were not included differential thermal expansion could cause much more radical changes in clamping force. In addition to the protruding sample a second ribbon is laid into the clamp perpendicular to it (forming a tee shape) to provide stability from rocking motions of the clamp halves over the sample.

The entire probe was evacuated by a diffusion pump which ran continuously. A simple calculation based on molecular flow shows that the pressure at which the gas will cause an error of 1% at a Q^{-1} of 10^{-3} in the lowest vibration mode, the worst case, for a typical vibrating reed sample is about 10^{-3} torr. Pressures were not measured in the probe but were probably well below 10^{-4} torr when the probe was immersed in LN_2.

The sample in its clamp was then held in a thick square-tubular copper housing which is split lengthwise to allow positioning of the clamp at any position along its vertical axis, accommodating different sample lengths. The housing also serves to support the drive and receiver electrodes, to maintain a thermal shield around the sample and to provide isolation from vibrations. The electrodes are threaded to allow adjustment of their distance from the reed, and mounted in Teflon sheaths for electrical isolation. The mechanical isolation comes from suspending the housing from two small wire loops. Surrounding the copper housing is a heat shield which is maintained within a few degrees of the housing's temperature. Its top part serves as a platform from which the housing is suspended, and has a hole in its center for wires (and vacuum) to pass through. Finally, the outer can maintains the vacuum seal and conducts heat out to the LN_2 or LHe bath. The experiments were conducted primarily from 80 K upwards in a LN_2 dewar, but some measurements were made down to 10 K in a LHe dewar to check for the presence of any lower-temperature peaks (which were not found).

The housing, clamp and sample were heated by heaters in each half of the housing. The temperature was measured by a silicon diode temperature sensor mounted in a hole in the clamp about 1 mm from the sample. A Lakeshore DTC-500 temperature controller was used to maintain the temperature constant to within about 10 mK. The sensor was calibrated against a platinum resistance thermometer (prt). The prt was calibrated by measuring its resistance at 4.2K, 77.36K, and 273.15K. The first and third values were used in a two-point prt calibration method published by Besley and Kemp(3.8).

The heat shield was heated separately using a pair of thermocouples operating between the sample housing and the heat shield to measure the temperature differential between them. The temperature was controlled using a Harwell temperature controller, which was turned off while operating below 95 K to allow temperature stabilization.

The one-dimensional vibration isolation provided by the two-wire suspension of the housing is parallel to the direction of vibration of the reed. Vibrations along the vertical or the other horizontal axis lie along the length or width of the reed and should not couple to the vibrations of interest. Further isolation from external vibrations was provided by the fact that the probe is suspended from a collar at its top end, 1.5 meters above the reed. It was found necessary to use a thin foam between this collar and the supporting stand, and to put the entire stand and dewar on an 8 cm thick foam cushion. In addition the wires from the instrument rack and the rubber hose from the diffusion pump had to be mechanically secured, in the latter case to the wall, then to the support stand, before going to the top of the probe. This eliminated all external vibration sources except for that due to the bubbling in the cryogenic liquid, which could be reduced by a factor of 3 or 4 by filling it up to a high level so that the bursting bubbles were well above the position of the reed. Also, at temperatures above about 150 K where the bubbling got worse, this problem could be reduced significantly by lifting the probe above the level of the cryogenic liquid while still retaining enough cooling to be able to maintain a stable temperature. The mechanical vibration problem falls off radically for reed vibration modes higher than the fundamental, as will be explained below.

3.3 ELECTRONICS

3.3.1 Drive System

The overall block diagram for electronic measurement and control is shown in figure 3.4. As was mentioned in Chapter 2, Q^{-1} was measured by recording the response (equation 2.24) versus frequency at nine points over an interval of twice the FWHM. The reed was driven electrostatically by a sine wave voltage applied to the drive electrode. The vibrating reed and the receiver electrode form a capacitor. A relatively large DC voltage, usually about 50 V, applied to the receiver electrode induced an oscillating charge on the electrode, and this current was amplified and measured. Using a lock-in amplifier, one can measure either the real or imaginary part of the response, or any linear combination of them by setting the phase. The imaginary part, which is close

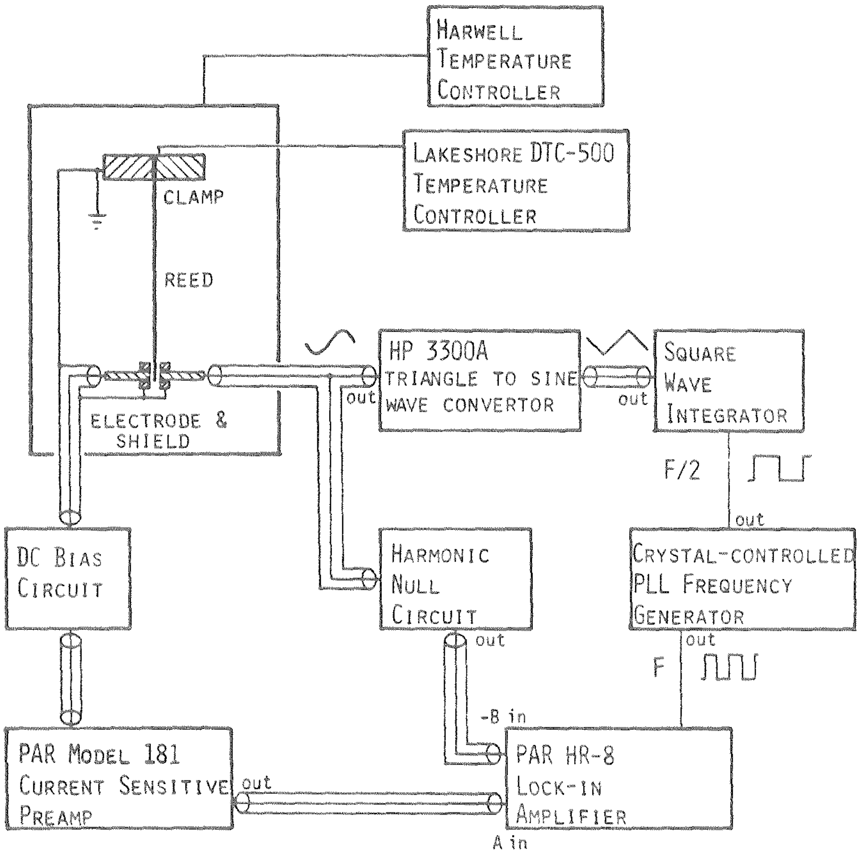

Figure 3.4 Block diagram for the internal friction drive and detection electronics, as well as the temperature control.

to a Lorentzian, was used because it is superior for measuring Q^{-1}. As we will see below the current measured is then given by

$$I(\omega) = I_{max} \frac{\omega\omega_o^3/Q}{(\omega_o^2-\omega^2)+\omega_o^4/Q^2} . \tag{3.1}$$

We consider first the drive electronics. The most stringent requirements on the frequency stability occur on the steep side of the Lorentzian response when the width Q^{-1} is small. Taking the derivative of $I(\omega)$ and evaluating at the half-amplitude points $\omega = \omega_o(1 \pm \frac{1}{2Q})$, to first order we have

$$\left.\frac{\partial I}{\partial \omega}\right|_{\omega_o(1\pm \frac{1}{2Q})} \approx I_{max} \frac{Q}{\omega_o} \tag{3.2}$$

where I_{max} is the value at $\omega = \omega_o$, yielding

$$\frac{\delta I}{I_{max}} = \frac{1}{I_{max}} \frac{\partial I}{\partial \omega} \delta\omega = Q \frac{\delta\omega}{\omega_o} \tag{3.3}$$

The smallest values of Q^{-1} ever measured were 2×10^{-4} and the smallest measurable response increment $\delta I/I_{max}$ was about 10^{-3} so the maximum frequency stability needed was $\delta\omega/\omega_o = 2 \times 10^{-7}$, over a measuring period of the order of minutes. This required the use of a crystal oscillator. A phase-locked loop was built with three user-settable divide counters. The 10 MHz crystal frequency was divided by N_1, multiplied by N_2, then divided by N_3 where N_1 and N_2 range from 1 to 100 and N_3 goes to 10^6. This ensured that some combination of the three numbers could be found which will yield a frequency satisfactorily close to any desired value. The numbers were calculated by a small calculator program. The frequency drifts observed were about 2×10^{-6} overnight, less than 4×10^{-7} over an hour, and perhaps 10^{-7} over a few minutes.

A square wave at frequency $\omega/2$ went to an integrator which was built with automatic gain control (AGC) to adjust the integration rate to yield a constant-amplitude triangle wave at any frequency in the range 10 Hz - 10 MHz. This was built into a plug-in unit for an HP 3300A function generator whose triangle to sine wave converter was used to yield the drive signal. The drive had a maximum amplitude of 10 V rms and showed an amplitude stability of about 5×10^{-4}. Harmonics at ω, $3\omega/2$, . . . are also present at a low level. The close proximity of the drive and detector electrodes unfortunately allows the latter to capacitively pick up the drive frequency in addition to detecting the reed motion. One advantage of the present arrangement is that the drive voltage is at $\omega/2$ and hence is filtered out by the lock-in amplifier. However any $\sin \omega t$ drive harmonic looks like a signal and if it varies with time it adds noise to the response. The dual AGC feedbacks in the square-to-triangle converter seem to generate just such a low level harmonic whose amplitude varied at frequencies below about 0.1 Hz, which was a minor annoyance. Coaxial ground shields at the electrode tips reduced the capacitive pickup by over a factor of 200, unless the reed (which is at ground) was narrower than the electrode, allowing the drive's electric field to leak around it to a greater extent.

The force on the reed due to the electric field is given by the gradient of the electric field energy. For a drive voltage given by $V = V_1 \sin(\omega t/2)$, the force is

$$F = \frac{1}{2} \varepsilon_o \frac{A}{d^2} V^2 = \frac{\varepsilon_o A}{4d^2} V_1^2 (1+\cos \omega t) \tag{3.4}$$

where A is the area of the electrode facing the reed, ε_o is the permittivity of free space, and d is the reed-electrode spacing. The reed is driven at twice the frequency of the voltage.

A small asymmetry in noise level was consistently noticed between the low- and high-frequency sides of the response peak. This can be explained by an interference between the effects of two harmonic terms, as follows. Writing

$$x(t) = x_o + x_1 \sin \omega t + x_2 \cos \omega t \tag{3.5}$$

and

$$\begin{aligned} V_1(t) = V_1 \sin (\tfrac{\omega}{2} t) &+ V_{21} \sin \omega t + V_{22} \cos \omega t \\ &+ V_{31} \sin \tfrac{3}{2} \omega t + V_{32} \cos \tfrac{3}{2} \omega t + \ldots \end{aligned} \tag{3.6}$$

we have

$$F(t) = \frac{1}{2} \frac{\varepsilon_o A}{(d_1(t))^2} (V_1(t))^2 - \frac{1}{2} \frac{\varepsilon_o A}{(d_o(t))^2} V_o^2 \tag{3.7}$$

where d_o and d_1 are the time-varying distances to the receiver and drive electrodes,

$$d_1(t) = d_1 - x(t) = d_1 - x_o - x_1 \sin \omega t - x_2 \cos \omega t \tag{3.8}$$

and likewise

$$d_o(t) = d_o - x(t). \tag{3.9}$$

Inserting (3.5) into the left side of equation (2.21) and (3.7) into the right, keeping terms only to second order, and throwing out all terms on the right (in the force expression) that do not have a time dependence of sin ωt, cos ωt, or a constant to match those on the left, we get after some algebra

$$x_o = \frac{-1}{m\omega_o^2}\left(F_o - F_1\left(1 - \frac{x_2}{d_1'}\right)\right), \tag{3.10}$$

$$x_1 = -\frac{F_1}{m}\,\frac{\frac{\omega_o^2}{Q}\left(1 - \frac{2V_{31}}{V_1}\right) + \frac{2V_{32}}{V_1}\left(\omega_o'^2 - \omega^2\right)}{\left(\omega_o'^2 - \omega^2\right)^2 + \frac{\omega_o^4}{Q^2}}, \tag{3.11}$$

and

$$x_2 = -\frac{F_1}{m}\,\frac{\left(\omega_o'^2 - \omega^2\right)\left(1 - \frac{2V_{31}}{V_1}\right) - \frac{2V_{32}}{V_1}\frac{\omega_o^2}{Q}}{\left(\omega_o'^2 - \omega^2\right)^2 + \frac{\omega_o^4}{Q^2}}, \tag{3.12}$$

where

$$\omega_o'^2 \equiv \omega_o^2 - \frac{2}{m}\left(\frac{F_o}{d_o'} + \frac{F_1}{d_1'}\right), \tag{3.13}$$

$$F_1 \equiv \frac{\varepsilon_0 A V_1^2}{4 d_1'^2} \quad \text{and} \quad F_2 \equiv \frac{\varepsilon_0 A V_0^2}{2 d_0'^2} , \tag{3.14}$$

and

$$d_0' \equiv d_0 + x_0 \quad \text{and} \quad d_1' \equiv d_1 - x_0 . \tag{3.15}$$

Typical values of x_1, the quantity measured, are 2.5 µm for the lowest mode at about 100 Hz, which gives a maximum strain of about 5×10^{-7}.

The noise asymmetry can now be explained. It results from the second term in the numerator of the response, equation (3.11). This term results from the cos $3/2\,\omega t$ harmonic and changes sign as ω goes past ω_0. The V_{21} sin ωt component, which is capacitively picked up as already mentioned, is independent of ω. If V_{32} is correlated in time with V_{21}, they will add on one side of the peak and subtract on the other.

Actually (3.10) and (3.11) are more useful than their use above suggests, as they display several other more important effects. First, the mean position d_0 (or d_1) of the reed is changed, as indicated by (3.15), because of the DC forces F_0 and F_1 from the two electrodes, with $F_1 < .04 \cdot F_0$ for the voltages used. If the electrodes are positioned wrong initially or the reed curled slightly with time, this force can pull it completely over to the receiver electrode and short it out, or at least bend it so close that the forces become nonlinear due to $x(t)$ becoming a large fraction of d. In this case the reed sees a significantly larger force when it is close to an electrode than it does 1/2 cycle later, providing a (nonlinear) feedback. This can be tested for by reducing the voltage and looking for changes in the response, or simply by observing a poor fit to the theoretical form of the response.

Another frequently used test was to trade the connection to the drive and detector electrodes, thus exchanging their functions. If $d_o \neq d_1$, ω_o' will change according to (3.13). This results from the fact that both DC forces (equations 3.14), being proportional to $\pm x$ to first order in x, just mimic the elastic modulus and both reduce it. Applying the larger voltage, V_o, to the smaller of d_o or d_1 results in the largest modulus reduction. Interchange of electrodes was used, then, to test for reed centering. If ω_o' was very much higher for one connection than for the other, the electrode positions were adjusted. If not, the connection with higher ω_o' was used.

The modulus shift was primarily a problem for the first mode, whose effective one-dimensional spring constant is by far the smallest. This is because higher modes involve greater curvature of the reed for the same deflection. The full calculation of the mode shapes and frequencies are given by Timoshenko et al.(3.9) and will not be treated here. The frequencies for the sequence of modes n = 1, 2, 3, ... are in the ratio 1 : 6.267 : 17.55 : ... and quickly approach limiting values of $(2n-1)^2$, if the frequency for mode 1 is assigned the value 1.425. The mode shape is independent of sample properties or dimensions, provided the sample is a rectangular bar, and when that is not true it is still uniquely determined by the shape of a given sample. Then the entire motion is determined by that of a single point and can be treated as a one-parameter oscillator with an anelastic spring. The effective elastic spring constant is proportional to ω_o^2, which for the first two frequencies has a ratio of 39.3 : 1. Thus the shift in apparent modulus due to the electrode static forces will be only 4% as large in the second mode as in the first. Since the modulus shift varies if the electrodes or reed move even slightly, with temperature or other factors, a plot of apparent modulus vs. temperature is not reliable for the lowest mode.

The strong increase in effective spring constant with mode is also part of the reason for the fact mentioned previously that external vibrations are not as important for higher modes. In making measurements the same maximum response current I_{max} (at $\omega = \omega_o$) was generally used where possible. Then $x_{max} \sim \omega^{-1}$ but from equation (2.22) or (3.11) the driving force increases with vibration frequency since $F \sim \omega^2 x \sim \omega$. Thus the apparent forces due to external vibrations become relatively smaller at higher frequencies. The other reason is that for higher modes they do not couple to the vibration as efficiently because the inertial force is constant along the reed, but the mode shape dictates that portions between successive modes move in opposite directions. This increasingly cancels out the effective noise forces with frequency. In this connection it should also be noted that the required electric driving force F goes up faster than ω in high vibration modes. As the last node approaches the end of the reed where the electrodes are and passes into the area between them, the effective driving force falls off.

3.3.2 Signal Detection

The changing charge on the receiver electrode is given by

$$I = \frac{dQ}{dt} = V_0 \frac{dC}{dt} = V_0 \frac{d}{dt}\left(\frac{\varepsilon_0 A}{d_0 + x_1(t)}\right) \approx \frac{-i\omega\ \varepsilon_0 A V_0}{d'^2}\ x \qquad (3.16)$$

to first order in x. The term in x^2, which was dropped, yields Fourier components at dc and 2ω which are filtered out. With $x \ll d_0$, I is just proportional to ωx, as asserted in (3.1).

The signal was sent to a bias box where the DC receiver bias was added while the signal was capacitively coupled through to the PAR Model 181 current-sensitive preamp where the current was converted to a voltage at a gain of up to 10^9 V/A. This was then sent a PAR HR-8 lock-in amplifier. Its reference signal was taken from an output on the frequency generator.

The time-varying harmonics mentioned above, occurring in the drive voltage and capacitively picked up by the receiver, became increasingly bothersome for higher modes due to the increased drive voltage required along with the proportionality to ω inherent in capacitive pickup. This was nulled by using a portion of the drive voltage as a subtractive input to the lock-in amplifier. This also had the effect of subtracting off most of the ω/2 Fourier component that was picked up capacitively, thereby reducing signal overload in the input stages of amplification.

One other source of systematic error should be mentioned. There was a tendency for the electrodes to move toward each other at low temperatures. An error in the calculation of such changes due to thermal expansion had originally indicated an insignificant amount of motion, so the brass electrodes were not replaced. In fact, the change in total gap is expected to be about 14% from 77 K to 300 K due to thermal expansion, and the electrodes should have been replaced with copper ones. In any case, whether it was due to this or some other reason, consistent long-term drift of frequency ω_0 was noticed with time, particularly after heating to a new temperature in certain temperature regions. The most likely reason for this was a slowly changing position of either the reed or the electrodes. With measurements being made over a span of several minutes from one side of the Lorentzian peak to the other, if the peak drifts by a significant fraction of its width in this time the calculation of the peak width is biased to larger or smaller values, depending on the relative directions of drift and measurement. This is at its worst for very narrow (small Q^{-1}) peaks, and could cause errors of several percent. Thus it was always checked for by repeating the measurement at the two half-amplitude points, and if any drift was found a second set of measurements was taken in the opposite direction and the resulting Q^{-1} values averaged.

IV RESULTS AND MATHEMATICAL ANALYSIS

4.1 FITTING ω_o AND Q^{-1}

The data taken on a sample in a given vibration mode at a given temperature consisted of measurements of the amplitude of response to a constant amplitude driving force at nine frequencies spaced over an interval about twice as wide as the FWHM of the Lorentzian. This was then repeated at a set of temperatures selected to sample the internal frequency spectrum at intervals of 1/2 the FWHM of an internal friction Debye peak (not to be confused with the above Lorentzian peak!). This procedure was repeated for each of the lowest three modes of the sample.

The data for each temperature were least-squares fit to the mathematical form

$$f(\omega) = A \left\{\cos \phi \ \mathrm{Im} \left[I(\omega_o,Q^{-1},Q_L)\right] + \sin \phi \ \mathrm{Re} \left[I(\omega_o,Q^{-1},Q_L)\right]\right\} + a \tag{4.1}$$

where Q_L is the Q setting of the lock-in amplifier's signal filter, which was used at settings of 5 or 10. $I\ (\omega_o,Q^{-1},Q_L)$ is the complex response as modified by the lock-in amplifier's transfer function. The offset, a, is required because of the presence of small constant instrumental offsets. The lock-in phase setting was adjusted to maintain ϕ near zero. Then there are 5 parameters to fit: ω_o, Q^{-1}, A, a and ϕ.

After initially developing the program a number of data sets were generated consisting of the (approximately) Lorentzian peak plus a small normally distributed pseudorandom error, with a standard deviation of either 1% or 0.1%. This was done for n_d = 5, 9, and 15 point fits with $n_p = 4$ fit parameters (ω_o, Q^{-1}, A, a). The standard deviation s_Q of the fitted value of Q^{-1} was found to be approximately given by

$$\frac{s_Q}{Q^{-1}} \approx 6 \frac{\sqrt{SSE}}{\sqrt{n_d - n_p}\, A} \tag{4.2}$$

where SSE is the sum of the squares of the errors for the fit. This was used in estimating the error in Q^{-1} for subsequent actual data. The average magnitude of the errors depends on several factors. First, we see that they tend to be a fixed fraction of Q^{-1} so the absolute errors are higher for higher internal friction. They also tended to be somewhat larger for the lowest mode where vibrations and frequency drift were serious problems, the latter only being noticeable at small Q^{-1}. Errors were also larger for the third mode where capacitive pickup of the drive voltage became worse. Data taken later, after more improvements were made, were generally better unless the reed was too narrow (as mentioned previously). A rough average estimate for S_Q/Q^{-1} based on (4.2) would range from 0.5 - 1% for most of the sets of data. Estimates of the error from the differences between Q^{-1} values when two or more measurements were made under identical conditions agree well with this estimate. In one or two cases the entire peak was remeasured 2-3 months later with excellent agreement, indicating in addition that no hydrogen had been lost or gained.

4.2 INTERNAL FRICTION RESULTS

For a continuous distribution of activation energies equations (2.26) and (2.27) become

$$M_1 = M_u - \frac{1}{T}\int_0^\infty g(E)\,\exp(-\ell n\,\omega\tau_0 - E/kT)\,\mathrm{sech}(\ell n\,\omega\tau_0 + E/kT)\,dE \qquad (4.3)$$

and

$$M_2 = M_1 Q^{-1} = \frac{1}{T}\int_0^\infty g(E)\,\mathrm{sech}(\ell n\,\omega\tau_0 + E/kT)\,dE \qquad (4.4)$$

where from equation (2.13) we see that the expected 1/T dependence has been put in explicitly, while the distribution function g(E) contains the factor $c(\Delta P)^2/V_o n_t k$. Note that due to the presence of $(\Delta P)^2/n_t$, g(E) is not just the number of defects per unit energy found in an interval dE about an activation energy E, which we might properly term the distribution of activation energies and refer to as n(E). Instead, it should probably be called the distribution of relaxation strengths over activation energy. Actually, the situation may be even more complex than this, due to the distribution in the sites' ground state energies or well depths E_g. If this distribution covers an energy range much smaller than kT for temperatures of interest, no further change results. If not, g(E) contains a site occupation factor. Since any site can contain only 0 or 1 hydrogen atom, this factor is just the Fermi-Dirac distribution $F(E_g) = (1 + \exp((E_g - \mu)/kT))^{-1}$, where μ is the chemical potential for hydrogen. Then $g(E) = ((\Delta P)^2/n_t)F(E_g)n(E)$. In spite of these complication, g(e) will frequently be referred to as the distribution of activation energies for the sake of verbal economy.

Note also that Q^{-1}, though widely used in the literature, is not really the best parameter to use, especially when it is large, because it is just M_2/M_1, and M_1 not only decreases with temperature but displays the further decrease around the M_2 peak illustrated in figure 2.6. The decrease is proportional to the M_2 peak strength. M_2/M_1^m has been used throughout rather than Q^{-1} (though it is frequently referred to as M_2 for brevity), where M_1^m is $M_1(T_{peak})$.

4.2.1 The Q^{-1} and ω_o Data

The internal friction data for the four Zr_2PdH_x samples are shown in figures 4.1 - 4.4 plotted as E_2 versus 1/T, the modulus M of interest being Young's modulus E. Note the shift to higher temperature with increased measurement frequency as expected. The data for the unhydrided sample was taken earlier while more attention was being paid to improving the apparatus and reducing noise than to data collection. Measurements were made using the second and third vibration modes but unfortunately the third mode data were not quite carried past the peak. The elastic modulus E_1, which is proportional to ω_o^2, is shown in figure 4.6 for the C = .86 sample, normalized to its maximum value. It displays the behavior described above. The mode 1 frequency also has imposed on it the additional effective modulus change due to slowly changing static electrode forces mentioned at the end of chapter 3, largest at low T, which act to cancel the normal decrease with T also described in Chapter 3.

Most of the data were taken from about 80 K to 370 K. For the second mode of the C = .86 sample, however, measurements were extended down to 10 K to check the low temperature behavior. These data, shown in figure 4.5, show that the internal friction decreases to a background level almost identical with that seen just above the peak. Note that in figures 4.2 to 4.4 the high temperature minimum level increases with

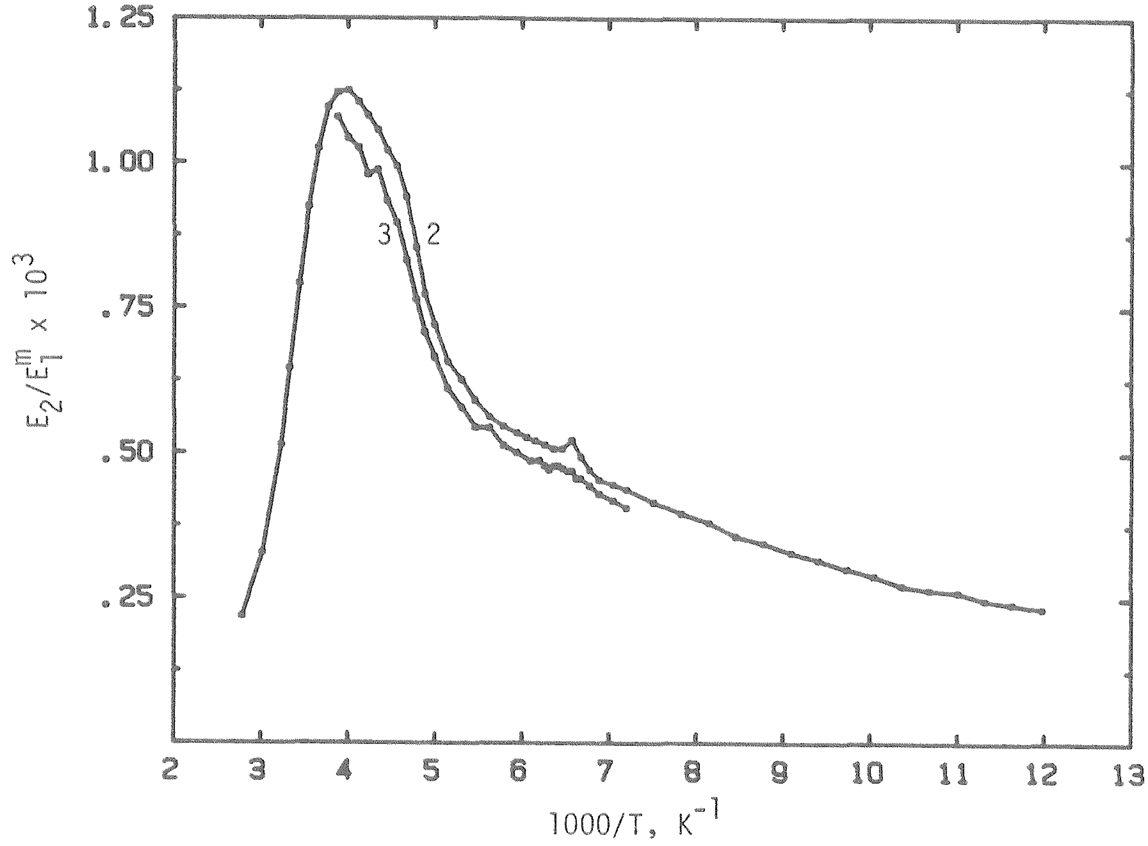

Figure 4.1 Internal friction for the second and third vibration modes of the unhydrogenated a-Zr_2Pd sample, with mode numbers labeled on the figure. Peak frequencies: Mode 2, 252.42 Hz. Mode 3, 706.95 Hz. Errors are smaller than the diameter of the dots.

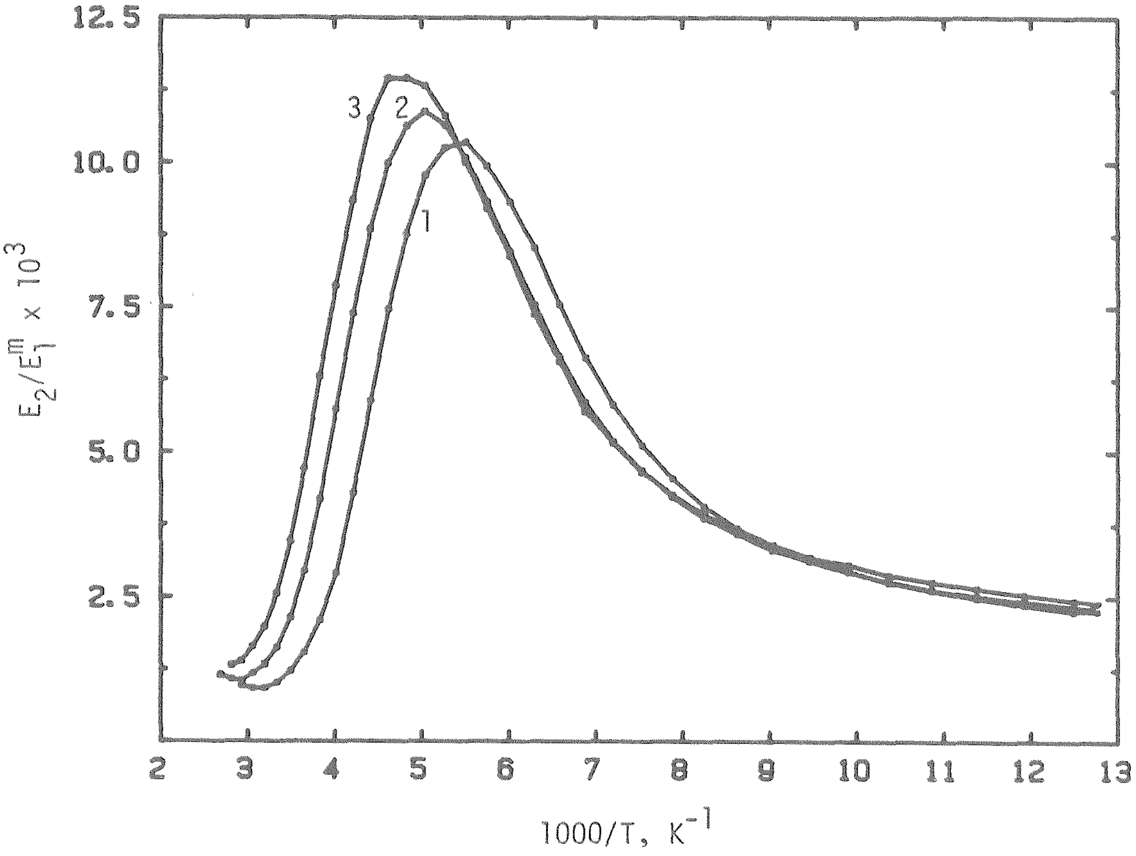

Figure 4.2 Internal friction for the first three vibration modes of $(Zr_2Pd)_1H_{.23}$. The mode is indicated by a number near each curve. Peak frequencies: Mode 1, 130.47 Hz. Mode 2, 813.99 Hz. Mode 3, 2227.0 Hz. Errors are smaller than the dots.

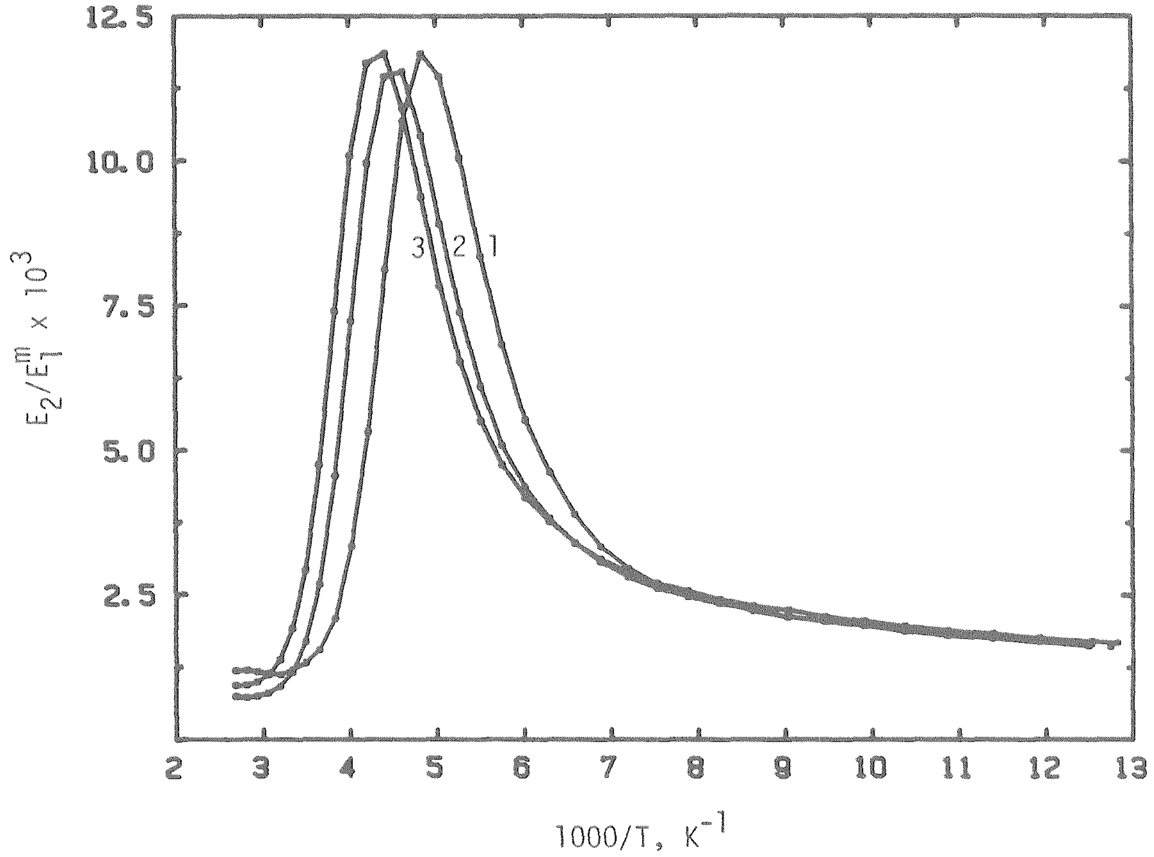

Figure 4.3 Same as figure 4.2 for c = 0.64. Peak frequencies: Mode 1, 108.56 Hz. Mode 2, 707.05 Hz. Mode 3, 1978.8 Hz.

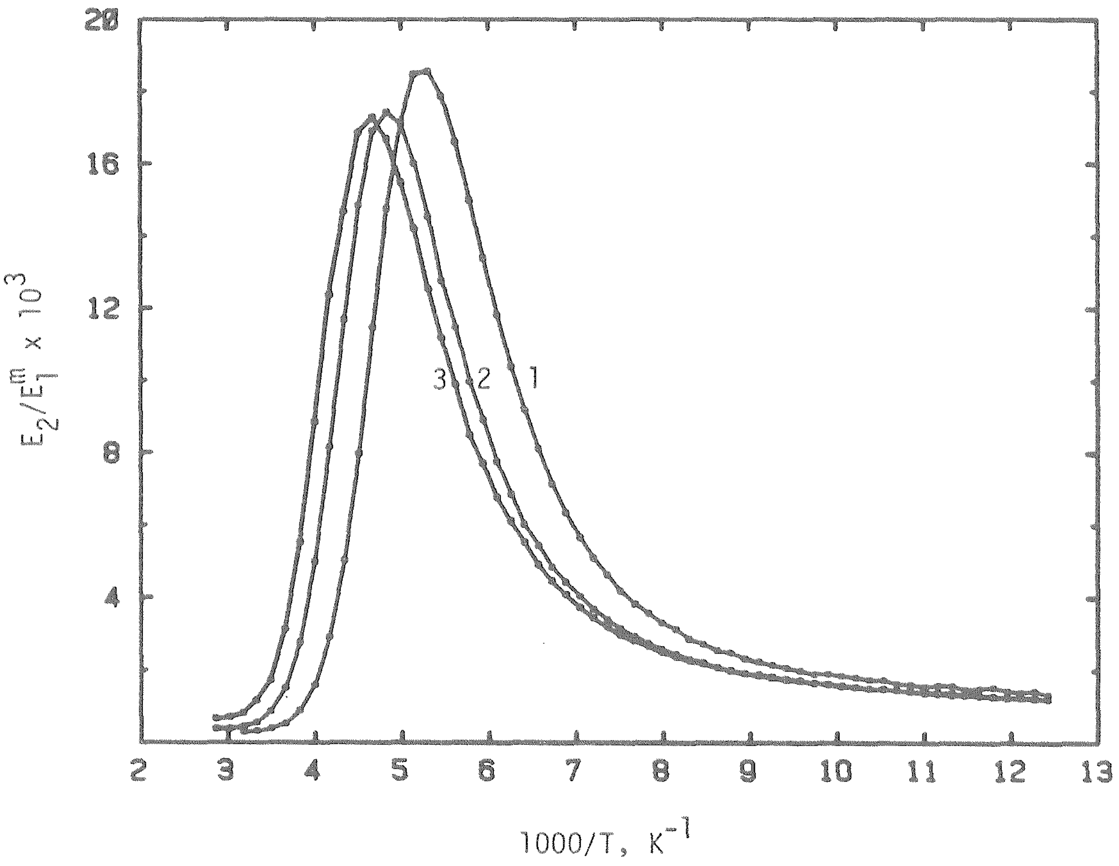

Figure 4.4 Same as figure 4.2 for c = 0.86. Peak frequencies: Mode 1, 125.43 Hz. Mode 2, 852.92 Hz. Mode 3, 2354.0 Hz.

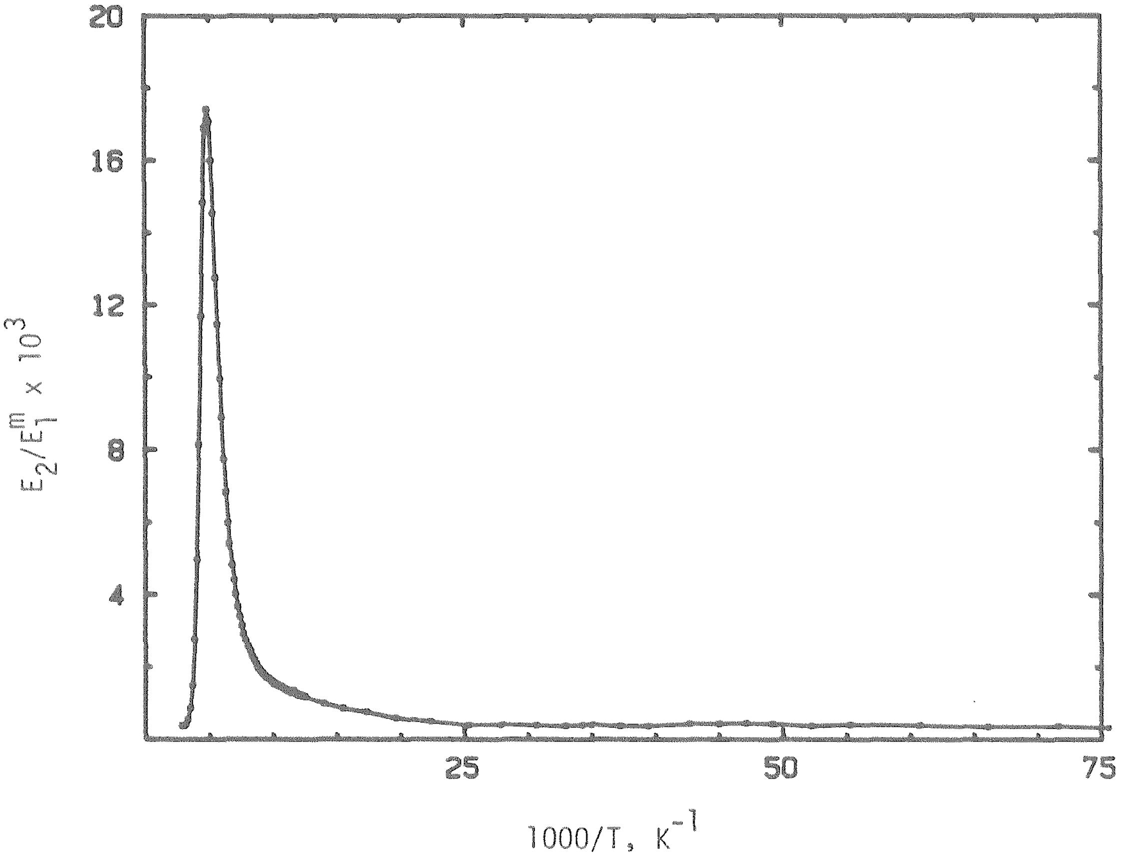

Figure 4.5 Internal friction from 10 K to 350 K for the second mode of the c = 0.86 sample. Peak frequency: 852.92 Hz.

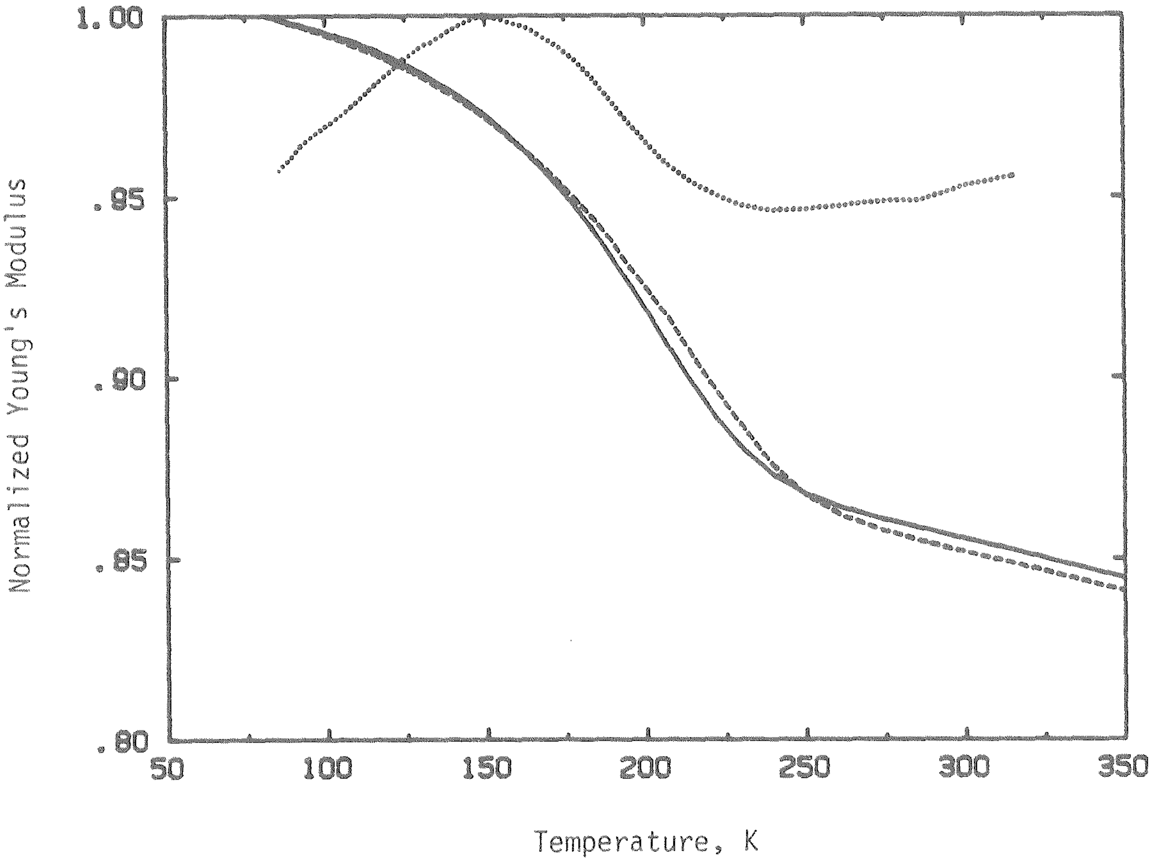

Figure 4.6 Young's modulus for the 3 modes of the c = 0.86 sample, normalized to its maximum value. ...., mode 1, 125.43 Hz. ——, mode 2, 852.92 Hz. ---, mode 3, 2354.0 Hz.

increasing frequency, indicative of a thermoelastic internal friction contribution.

Data taken on a $Y_{64}Fe_{36}$ alloy are shown in figure 4.7. The peaks look very similar to those seen by Kunzi, et al.(4.1) in $Y_{64}Co_{36}$, which were later found to be due to a hydrogen impurity(4.2). The peaks in the present data occur roughly 35 K lower in temperature, and there is an additional bump in the tail region. The high-temperature rising background looks like that found in many other metallic glasses as the glass transition temperature is approached; see below for further discussion. These data were taken early on and have much larger error levels than the later data, of the order of 5%, or 5 - 10 times that of the Zr_2PdH_x data. Further, unlike the Zr_2Pd alloys this sample was not pre-annealed and showed considerable annealing behavior when heated to 100 C during measurement. As can be seen in figure 4.6, the internal friction background went down greatly from run 1 to run 2 on the lowest mode, but further annealing took place in run 2, accounting for some high-temperature fall off.

4.2.2 Q^{-1} Backgrounds

The portion of the background due to air damping and clamping losses will (hopefully) be fairly constant over temperature. In any case this is the assumption that is commonly made in the absence of any better information, and even if incorrect this part of the background forms only a few percent of the size of the present peaks. The strength of the contribution from thermoelastic damping is(4.3)

$$\delta M = \frac{\alpha^2 T M_u^2}{C_\sigma} \qquad (4.5)$$

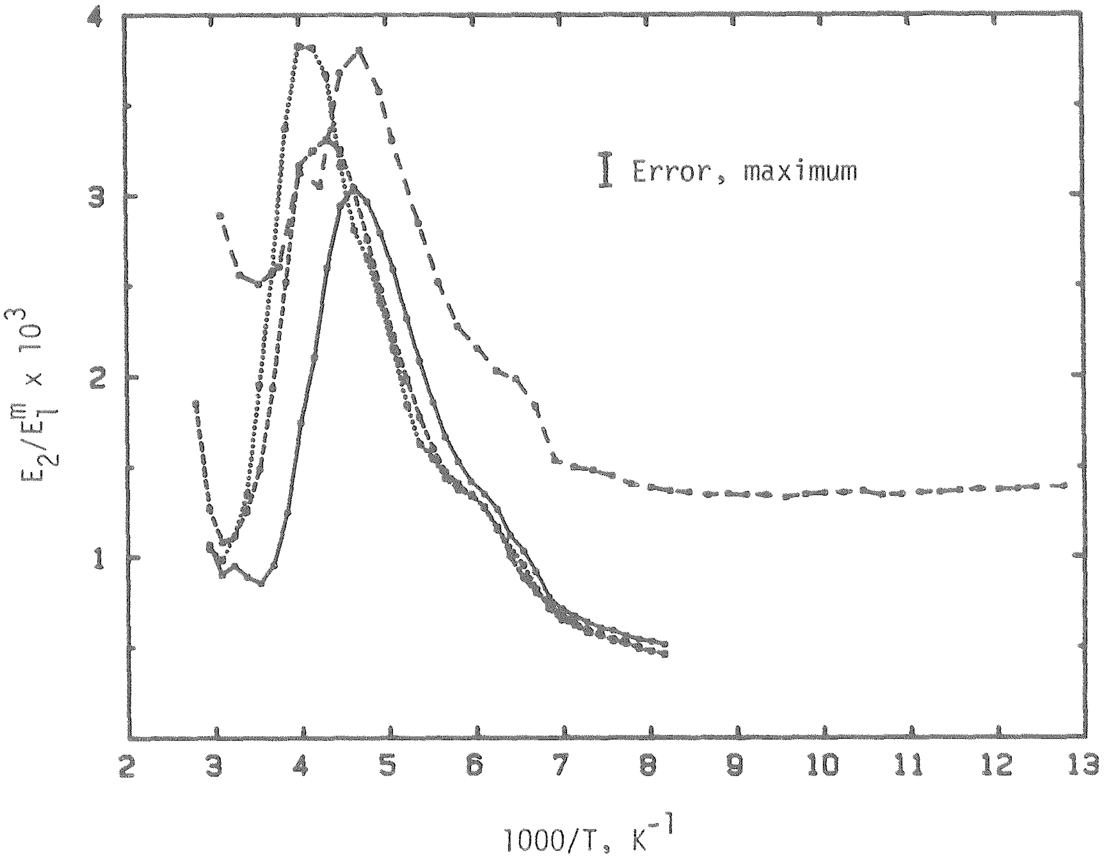

Figure 4.7 Internal friction for the first 3 modes of $Y_{64}Fe_{36}$. The first mode was measured twice: — — —, first measurement, in which significant annealing occurred, 106.96 Hz. ——, second measurement of first mode, 107.08 Hz. ----, second mode, 589.45 Hz. ...., third mode, 1560.7 Hz. Errors are proportional to Q^{-1}; the error bar shown is for the peak.

where α is the thermal expansion coefficient and c_σ is the specific heat per unit volume with the stress constant. Typical values for $\Delta = \delta M/M$ are around $1\text{-}2 \times 10^{-3}$. The relaxation time is

$$\tau = \frac{d^2}{\pi^2 D_{th}} \qquad (4.6)$$

where d is the reed thickness, $D_{th} = K_{th}/c_\sigma$ is the thermal diffusion coefficient, and K_{th} is the thermal conductivity. In the temperature region of interest $D_{th} \sim 1/T$ while c_σ and α are roughly independent of T, so τ and δM both depend approximately linearly on T. If $\omega\tau \ll 1$ the Debye peak

$$M_2 = \delta M \frac{\omega\tau}{1+(\omega\tau)^2} \qquad (4.7)$$

goes as $\delta M \cdot \omega\tau$, so M_2 might be expected to go very roughly as T^2. For pure Zr and Pd with reeds of thickness 25-40 μm (the thicknesses actually used), the peak frequencies would be 62 - 24 KHz and 31 - 12 KHz, respectively. Accounting for perhaps a factor of 2-5 increase in τ (and therefore the same decrease in peak frequency) due to the decreased thermal conductivity of glassy relative to crystalline metals(4.4), this still leaves $\omega\tau < 1$ in all cases. However, published data where a background has not yet been subtracted often show something closer to a linear dependence of the thermoelastic component on T. Since even the amorphous unhydrided Zr_2Pd alloy showed a strong Q^{-1} peak in the present data (figure 4.1), no direct information is available on the thermoelastic component's temperature dependence, and a linear T dependence was assumed. The relative thermoelastic and constant background levels were estimated by extrapolating the changing background at the high temperature minimum to zero frequency. Then each was subtracted from the data over the full temperature range.

4.3 MEASURING E_a AND τ_o

Once the Q^{-1} data are in hand the question arises of values for τ_o and E_a, and of whether the distribution of τ is based on a distribution of one or both of these parameters. The calculation of E_a and τ_o is done by measuring the 1/T shift between data taken at two different frequencies, and needs to be done assuming either a τ_o or an E_a distribution. For a τ_o distribution with E_a constant we see from equation (2.25) that, for a given point on the Debye peak, i.e., M_2 = const., we have

$$\ell n\ \omega\tau_o + E_a/kT = C \tag{4.8}$$

where C is a constant. Then for two sets of data taken at different frequencies, the shift in inverse temperature

$$\frac{1}{T_2} - \frac{1}{T_1} = \frac{k}{E_a}\ \ell n(\omega/\omega_2) \tag{4.9}$$

is independent of T or τ_o. Each point on the entire broadened peak shifts by the same amount and computing E_a merely requires fitting the two sets of data to each other by shifting one of them versus 1/T.

If E_a is distributed and τ_o is not, the data at each temperature will result from a contribution at a certain E_a and a small range of nearby values. The central value of E_a is given by (4.8) with C = 0, and is proportional to T. Solving (4.9) with this condition we find T_2 is related to T_1 by a multiplicative factor

$$\frac{T_2}{T_1} = \frac{\ln(\omega_1\tau_0)}{\ln(\omega_2\tau_0)} = \frac{\ln\,\omega_1 + \ln\,\tau_0}{\ln\,\omega_2 + \ln\,\tau_0} \quad . \tag{4.10}$$

Note that this shift ratio is a constant, independent of T or E_a. When plotted versus 1/T, peaks at low T (hence low E_a) shift more than peaks at high T (and E_a), as can be seen more easily from (4.9). The 1/T shift is proportional to $1/E_a$. Thus on going to higher frequency the broadened peak as a whole becomes more compact. The increased overlap of neighboring relaxation peaks means that not only does the overall peak become narrower but its shape changes; i.e., it does not scale, making the job of fitting the value of τ_0 much more difficult. In the limit of infinite T it collapses into a simple Debye peak, which will in general bear little resemblance to the original overall peak shape. This increased overlap also causes the peak height to increase, and in fact this just cancels the 1/T dependence of the relaxation strength, as we will see below.

A computer program was written to use data from a selected temperature window about the peak for the data of a second frequency, scale its amplitude, shift it versus 1/T, and thus fit it to a first peak. An interpolation scheme was needed because a given datum from the shifted set will in general not fall exactly on top of any of the first peak data. A Lagrangian interpolation was used between points on the first peak, using the six points centered on the interval of interest. For each temperature-shifted second peak datum this interpolation was done at the same temperature in the first peak, and the sum of the squares of the differences (or SSE) between these values computed. Then SSE was minimized with respect to the two parameters.

To analyze the shape changes that occur for an E_a distribution we return to (4.4) and consider a single value of E_o and the peaks it produces in each data set. The temperature at the top of these peaks will be labeled by T_i, where i refers to data set 1 or 2. Writing β for 1/kT,

$$\beta_i = -\frac{\ell n(\omega_i \tau_o)}{E_a} \tag{4.11}$$

and from (4.9) we have

$$\beta_2 = \frac{\ell n(\omega_2 \tau_o)}{\ell n(\omega_1 \tau_o)} \beta_1 \equiv C\beta_1 \tag{4.12}$$

where typically C is about .93 for mode 2 versus mode 1 and about .89 for mode 3 versus mode 1. Now consider the ratio $M_2(\beta_2,\omega_2)/M_2(\beta_1,\omega_1)$, which is the ratio of the anelastic moduli of the two data sets at these corresponding temperatures:

$$f(C,\beta) \equiv \frac{M_2(C\beta,\omega_2)}{M_2(\beta,\omega_1)} = C\,\frac{\int_0^\infty g(E)\ \mathrm{sech}(\ell n\omega_2\tau_o + C\beta E)\ dE}{\int_0^\infty g(E)\ \mathrm{sech}(\ell n\omega_1\tau_o + \beta E)\ dE} \tag{4.13}$$

$$= C\,\frac{\int_0^\infty g(E)\ \mathrm{sech}[C\beta(E-E_0)]\ dE}{\int_0^\infty g(E)\ \mathrm{sech}[\beta(E-E_0)]\ dE}\ . \tag{4.14}$$

Further, we could replace $C\beta(E-E_o)$ in the numerator and $\beta(E-E_o)$ in the denominator by x:

$$f(C,\beta) = \frac{\int_{-C\beta E_o}^{\infty} g(E_o + \frac{x}{C\beta}) \text{ sech } x \, dx}{\int_{-\beta E_0}^{\infty} g(E_o + \frac{x}{\beta}) \text{ sech } x \, dx} . \qquad (4.15)$$

The lower limit can be replaced by $-\infty$ because $\beta E_o = -\ln \omega_1 \tau_o$ is a large number. In this form the cancellation of the explicit 1/T dependence by the increasing overlap is apparent. For example, if g(E) = const. then f = 1, independent of anything. Sech x peaks at x = 0, so it selects the values of g(E) around E_o with a width given by $\Delta x/C\beta$ for the numerator and $\Delta x/\beta$ for the denominator, where $\Delta x = 2.63$ is the FWHM of sech x. This expresses in a different way the fact that any point in the numerator has more overlap from nearby values in $g(E_a)$ than does the same point in the denominator, since $C < 1$.

Now let us expand g(E) in a power series about E_o to examine the effect of slope and curvature on $f(C,\beta)$. Introducing

$$g(E) = g_o + g_1 (E-E_o) + g_2 (E-E_o)^2 + \ldots \qquad (4.16)$$

into (4.15) the odd powers of $E - E_o$ give zero because sech x is an even function of x. Then

$$f(C,\beta) = \frac{\frac{g_o}{\beta} I_o + \frac{1}{2} \frac{g_2}{C^2\beta^3} I_2 + \ldots}{\frac{g_o}{\beta} I_o + \frac{1}{2} \frac{g_2}{\beta^3} I_2 + \ldots} = \frac{1 + \frac{g_2 I_2}{2 g_o C^2 \beta^2 I_o} + \ldots}{1 + \frac{g_2 I_2}{2 g_o \beta^2 I_o} + \ldots} \qquad (4.17)$$

where

$$I_n = \int_0^\infty x^n \operatorname{sech} x \, dx \qquad (4.18)$$

and the first several values of $I_{2n}/(2n)!$ are 1.2377, 1.2683, 1.2727, and 1.2732, which rapidly converge to 1.2733. Notice that if fourth-order and higher terms are small, and the second derivative g_2 is positive, then $f > 1$, while $g_2 < 0$ results in $f < 1$. This should be obvious since, if the curvature is positive, increased overlap will tend to raise the local value of M_2 while negative curvature (as in the region of a peak) will do the opposite. A constant slope in g(E) has no effect because with more overlap the increasing contributions from the high-g side are cancelled by the lower contributions from the low-g side.

An attempt was made to estimate the first two or three even-power derivatives of g(E) from g itself (see below) or from the M_2 data, for use in calculating f. This would then be used in the fitting program to improve the quality of fit and the accuracy of the fitted parameters. The calculation from the M_2 data was made by making the crude approximation that $\operatorname{sech} x = \delta(x)$, which becomes good only in the limit where g(E) is slowly varying on the scale of the width of $\operatorname{sech}[\beta(E - E_0)]$. For calculations from both g and M_2 the derivatives were estimated by fitting a polynomial to a region around E_0 and extracting the derivatives of the polynomial. However, neither the resulting series in the numerator nor the denominator of (4.17) nor the overall expression converged, but seemed to experience increasingly wild oscillations as terms were added. This was then given up. However, figure 4.8(a) shows the second peak shifted onto the first, where its increase in regions of positive

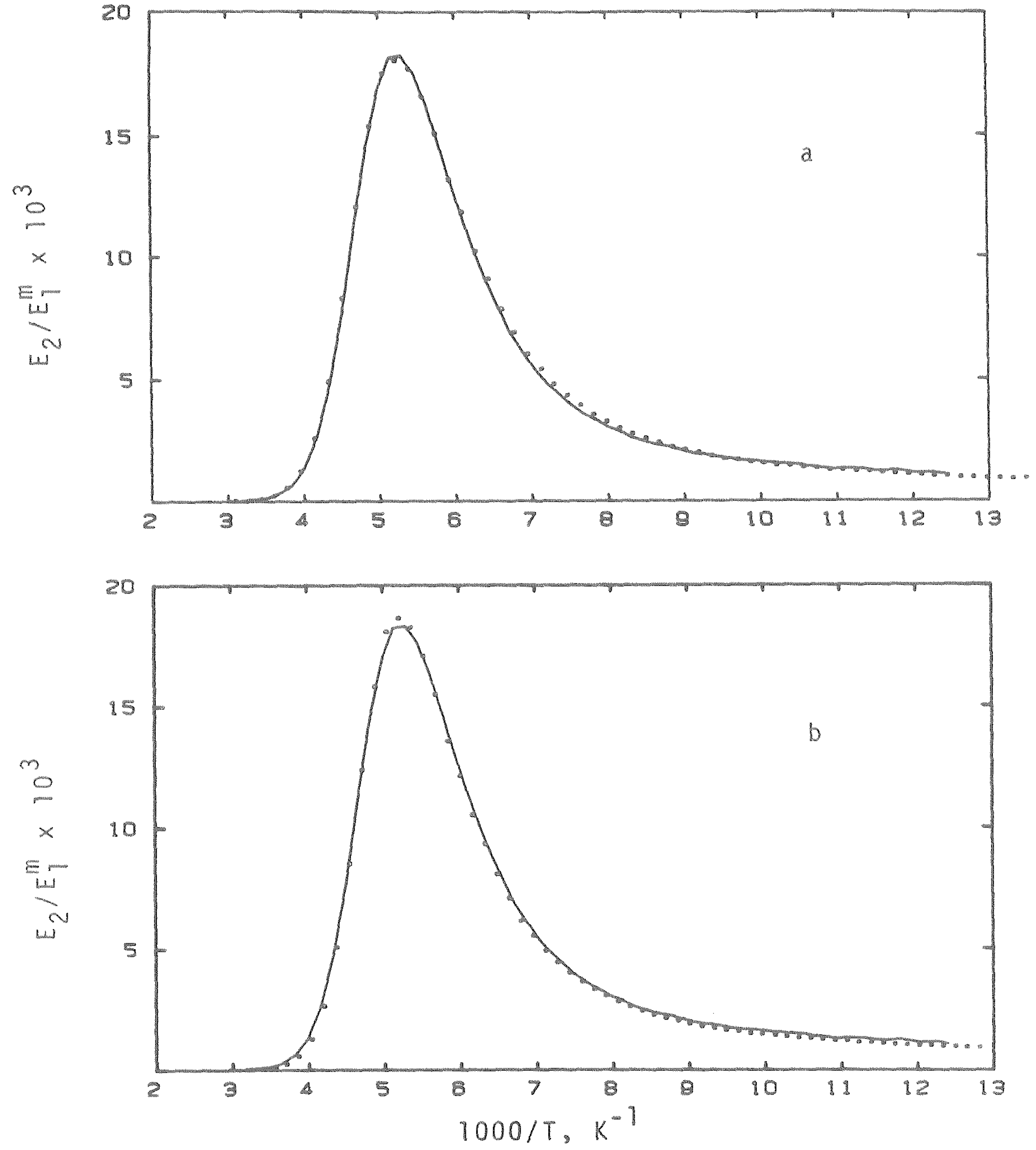

Figure 4.8 a). Internal friction of the c = .86 sample. ____, unshifted mode 1 data. ...., mode 2 data points scaled and shifted to best fit the mode 1 data over the top 40% of the peak, assuming a distribution of E_a and a single value of τ_o. b). The same as (a) but shifted assuming a distribution of τ_o with a single value of E_a.

curvature and decrease near the peak are visible. The relative standard error of fit was usually about 1-2%.

In order to better estimate the temperature shifts, then, the window in the fitting program was varied. At the minimum only about the top 5 points in the high frequency or second peak were kept, corresponding to only about the upper 15% of the data (between 85% and 100% of the peak height) being kept. At the maximum window width about the top 80% of the peak was kept. The plots of the resulting values of ln τ_o are shown in figure 4.9 versus percentage of the peak height included. If the M_2 peaks were symmetrical the plots should be flat (apart from random scatter). The value of τ_o used was that where roughly the top 40% of the peak is included in the window. If the window is narrower the statistics are not good, while if it is wider there may be significant bias due to errors in the estimation and subtraction of background levels.

In the case of the unhydrided a-Zr_2Pd sample the lack of complete data over the second measured peak meant that no reliable estimate of τ_o could be made. An attempt was made to estimate it by fitting only the 1/T shift and supplying an assumed relative amplitude externally, but the τ_o value calculated this way was so sensitive to the relative amplitude that even a 1% change shifted τ_o by 2-4 orders of magnitude! Finally, in the absence of any better information the τ_o value was extrapolated from the values for higher c, to 4×10^{-15}s, which is unlikely to be incorrect by more than a factor of 2.

Table 4.1 displays a variety of data for each sample. The temperature, natural vibration frequency, and internal friction value at the peak are given for each mode. The Young's modulus values at 80K are

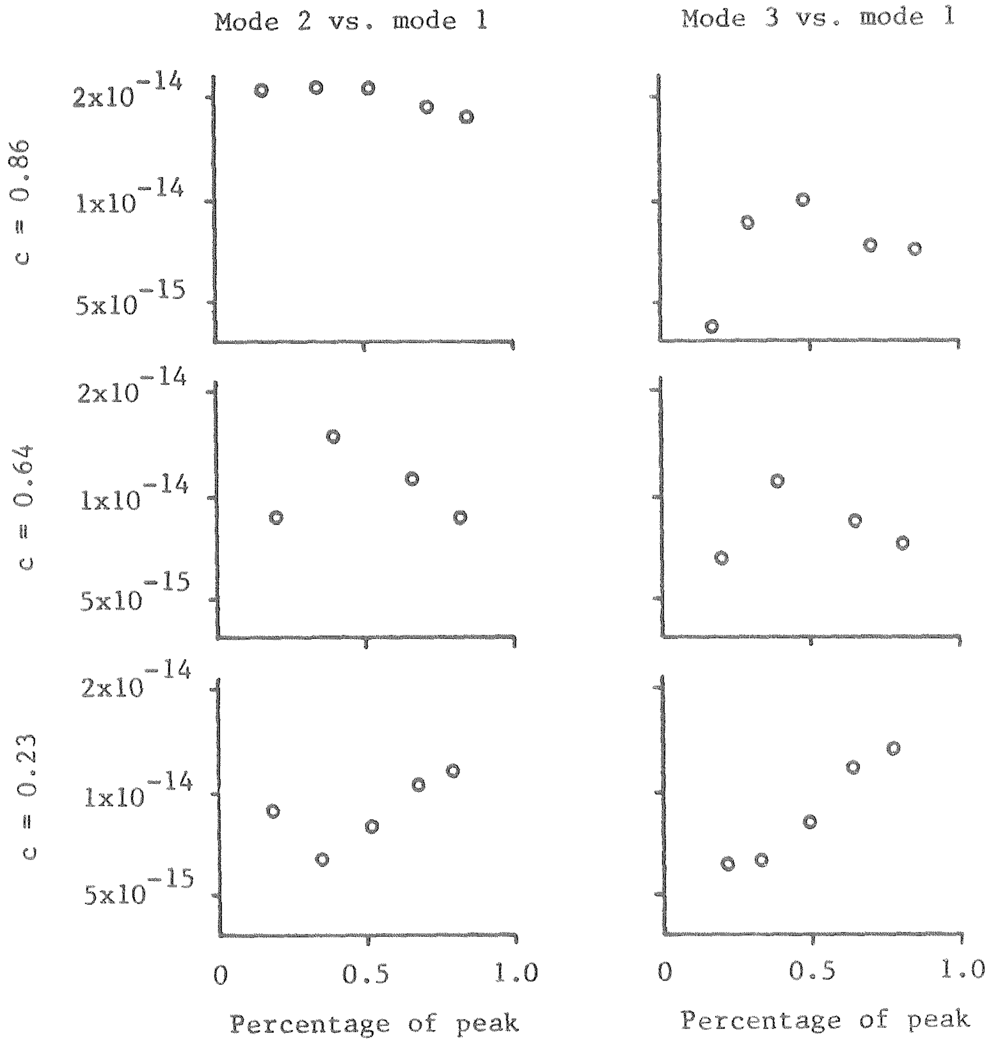

Figure 4.9 The fitted values of τ_o plotted against window width, parameterized by percentage of the peak height included. Figures on the left are for mode 2 data fit to mode 1 data, those on the right for mode 3 to mode 1. The top row of figures is for c = 0.86, the middle row for c = 0.64, and the bottom row for c = 0.23.

TABLE 4.1

Internal friction peak parameters, Young's modulus E, and τ_o values for the peaks measured in $(Zr_2Pd)_1H_c$ and $Y_{64}Fe_{36}$.

		$(Zr_2Pd)_1H_c$				$Y_{64}Fe_{36}$
	c =	~0	0.23	0.64	0.86	
	mode					
T_{peak}, K	1		184.1	204.9	190.9	214.7
	2	252.4	197.9	220.8	206.4	231.3
	3		211.0	230.1	214.9	245.2
f_{peak}, Hz	1		130.47	108.56	125.43	107.08
	2	252.42	813.99	707.05	852.92	589.45
	3		2227.0	1978.8	2354.0	1560.7
$Q^{-1}_{peak} \times 10^3$	1		9.5	11.4	19.4	3.04
	2	1.05	9.9	11.0	17.1	3.31
	3		10.2	11.0	16.7	3.88
FWHM/Debye FWHM	2	5.0	5.1	3.1	3.2	3.5
Asymmetry Ratio	2	2.2	1.8	1.6	1.7	1.5
$E(80\ K) \times 10^{-12}$, dyne/cm^2	2	0.6	0.8	0.9	1.3	—
$\tau_o \times 10^{14}$, s	2	—	0.6	1.3	1.5	10

computed from$^{(4.5)}$

$$E = \frac{12\rho\omega^2\ell^4}{t^2 n_i^4} \qquad (4.19)$$

where ρ is the density, ℓ is the length, and t is the thickness of the reed. The n_i are the numbers mentioned in Chapter 3 that give the ratios of the mode frequencies, and the first three values are 1.875, 4.694, and 7.855. The resulting values of E are only accurate to perhaps 10% in absolute value, a common problem with this type of measurement on glassy metals, due mostly to uncertainty in the reed thickness. Other quantities given in the table are the value of τ_o, the FWHM of the peak compared to that of a single Debye peak, and the asymmetry ratio of the peak as defined by Berry and Pritchet$^{(4.6)}$. This is the ratio of the half-width at half-maximum on the low temperatures side of the peak to that on the high temperature side. The asymmetry ratios previously seen in metal-metalloid and metal-metal glasses have been in the range of 1.6-1.8, while the peak width seen has been 2-4 times larger than that of a Debye peak$^{(4.2,4.6)}$. Qualitatively, the hydrogen peaks seen in most metallic glasses to date look remarkably similar in shape, suggesting perhaps a common basis related to the structural nature of the hydrogen sites in the glass.

The typical E_a values found at the peaks, in the range .42 - .59 eV, with τ_o of the order of 10^{-14}s, are just what are expected for hopping of single H atoms, as opposed to a collective relaxation mode, for example. If τ_o were the distributed variable, on the other hand, by using the value of E_a found at the peak we find that the τ_o distribution would range over an interval from about 10^{-11}s to something like

10^{-49}s, which is an obviously unphysical value. Since E_a varies as ln τ_o (if all else is constant), even if τ_o is distributed over a range of perhaps a factor of 5 or 10, as might be expected, that will leave almost all the responsibility for the variation in τ to a distribution in E_a. Nevertheless, fits were also attempted assuming a τ_o rather than E_a distribution. The quality of fit was typically twice as poor, though there would have been a much greater discrepancy in fit quality if the correction $f(C,\beta)$ for the curved regions of $g(E)$ could have been calculated in the former case. Figure 4.8(b) shows the same data as in figure 4.8(a) but with the shift calculated in this way, and the lack of compatibility is apparent. The fit should have been exact.

Incidentally, this may also explain an effect that has been seen with internal friction in glassy metals (not hydrogenated) approaching the glass transition temperature. There, the magnitude of the internal friction is commonly found to start rising exponentially with temperature(4.6, 4.8, 4.9, 4.10), apparently due to thermally activated hopping of the metal atoms. Berry(4.9) has noted that when E_a and τ_o values are computed from the temperature shift between data taken at two frequencies the τ_o values (e.g., 10^{-25}s) are unreasonable. He later suggested an explanation(4.11) which is mathematically incorrect, based on the idea that E_a is not truly a constant but depends on the temperature. This by itself is certainly to be expected on the basis of thermal expansion of the lattice. This expansion should be expected to affect the hopping saddle point energy more than the energy at the minimum. However, rather than making the linear expansion about the value of 2.6 eV calculated at T_o = 593K, as follows

$$E = E_0 - \alpha\ (T-T_0) \tag{4.20}$$

so that at $T = T_0$ the measured value E_a would be recovered, Berry used

$$E = E_0\ (1-\alpha t) \tag{4.21}$$

which does not have this property. Then arguing that τ_0 should be of the order of 10^{-13}s, he calculated the value of E_a which this implies, $E_a = 1.2$ eV. He then used this to calculate α. To put it another way, τ is then given by

$$\tau = \tau_0 \exp \left[\frac{E_0(1-\alpha T)}{kT}\right] = \left[\tau_0 \exp \frac{-\alpha E_0}{k}\right] \exp \frac{E_0}{kT} = \tau_0^* \exp \frac{E_0}{kT}\ , \tag{4.22}$$

τ_0^* is set equal to 10^{-25} s and τ_0 to 10^{-13} s. Unfortunately, this does not change anything, because τ is now given by $\tau_0^*\exp(E_0/kT)$ and when τ_0^* and E_0 are calculated from the data at 593K they will yield the same values as before.

In fact, the explanation for the unphysical values of τ_0 may lie in equation (4.14). An internal friction spectrum rising exponentially with T implies a g(E) of roughly similar shape which certainly has positive curvature. Then on going to a higher frequency, $f(c,\beta) > 1$ everywhere: the internal friction at the higher frequency is too high. If this is not accounted for it will result in a smaller 1/T shift and hence from (4.9) a larger value of E_a and smaller value of τ_0. Approximate calculations of this correction brought E_a down from 2.6 eV to 2.2 eV. This is not enough, as $\tau_0 = 10^{-14}$ s requires $E_a = 1.3$ eV. Thus further explanation is needed. However, the above discussion may explain the data in some of the other reported cases, which have not yet been analyzed for the $f(C,\beta)$ correction.

4.4 EXTRACTION OF g(E)

The obvious next item on the agenda would be an inversion of the integral equation, (4.4), to compute $g(E)$ from $M_2(\omega,T)$. It might seem surprising that no one has to this point attempted to do this in a non-parametric way for internal friction data. On the other hand, good numerical algorithms have only become available during the last decade. The only methods used to date have been to assume a given mathematical form for a relaxation strength distribution function, calculate M_2, then adjust the distribution parameters to get the best fit$^{(4.3)}$. One function used for M_2 was of the form $\mathrm{sech}(\alpha \ln \omega\tau)$. For $\alpha = 1$ this becomes just the Debye peak, while for $\alpha < 1$ the peak becomes broadened, while still symmetrical. Other distributions such as a simple rectangular one and a Gaussian in $\ln \tau$ have also been discussed and used. To better fit asymmetric internal friction peaks a distribution function composed of two half-Gaussians of equal magnitude but different widths have also been used$^{(4.12)}$. This worked fairly well in the peak region but did not reproduce the low temperature tail.

Consider now the problem of inverting (4.4). The internal friction data exist in the form of a discrete set of m measurements at temperatures T_i, $i = 1, \ldots, m$. To do a numerical inversion it is necessary that the energy spectrum also be discretized. This done (with n evenly spaced energy intervals), an interpolation scheme can be used between points $g_j = g(E_j)$, $j = 1, \ldots, n$. This forms a continuous function $g(E)$

parameterized by its values at the E_j, which if known could be inserted into (4.4) to calculate M_2 at any desired value of ω and T. Since there is no reason to believe that g(E) is not a reasonably smooth function, it was decided to use a smooth interpolation scheme rather than a simple one such as a trapezoidal or two-point rule. The aim was to try to do all calculations to an accuracy of the order of 0.1%. Simulations were carried out on a couple of smooth well-known peaked curves. They were approximated by Lagrange interpolation between discrete points. These points were chosen at intervals whose relation to the peaks' FWHMs was similar to those of the data at hand. It was found that 2p = 6 was the smallest even number of points that gave the desired accuracy of the interpolate to the actual curve near its peak. Therefore six points were used, centered about the energy interval of interest, and the interpolation used only in its central segment. In the pair of intervals at the beginning and end of each data set, the interpolation order 2p was reduced to 4 and 2 points as necessary.

Putting this form of g into (4.4) we get

$$M_2(\omega,T_i) = \frac{1}{T}\sum_{k=1}^{n-1}\int_{E_k}^{E_{k+1}}\left[\sum_{j=k-p+1}^{k+p} g_j \prod_{\substack{\ell=k-p+1\\ \ell\neq j}}^{k+p}\left(\frac{E-E_\ell}{E_j-E_\ell}\right)\right]\operatorname{sech}\left(\ell n\omega\tau_0+\frac{E}{kT}\right)\,dE. \tag{4.23}$$

The integrals were done by Simpson's rule, and again simulation was used to select the number n_s of intermediate points used between E_k and E_{k+1} to yield a Simpson integral of the desired accuracy. Then after interchanging the order of summation on j and k we finally get

$$M_2(\omega,T_i) = \sum_{j=1}^{n} A_j\,(\omega,T_i)\;g_j \qquad (4.24)$$

or

$$M_{2i} = A_{ij}\;g_j \qquad (4.25)$$

where

$$A_j(\omega,T_i) = \sum_{k=j-p}^{j+p-1}\;\sum_{r=1}^{n_s} S_r\;\mathrm{sech}\left(\ell n\omega\tau_0 + \frac{E_r}{kT}\right)\prod_{\substack{\ell=k-p+1\\ \ell\neq j}}^{k+p}\left(\frac{E_r-E_\ell}{E_j-E_\ell}\right) \qquad (4.26)$$

and S_r is the Simpson coefficient, $\left[\frac{2 \text{ or } 4}{3n_s}\right]\Delta E$.

If we take n = m and try to solve this by inverting the matrix A_{ij}, the result is nonsense. The reason is that (4.4) is a Fredholm equation of the first kind with a kernel, sech x, which is quite smooth. The result is that it is ill-conditioned. The meaning of this can be seen by supposing that to start with we have no errors in the M_2 data and we have the corresponding "correct" solution $g_0(E)$. To this solution we then add a function δg which is highly oscillatory, varying rapidly over the width of the kernel. The more rapidly it oscillates the lower will be its contribution to the integral, if its amplitude is constant. Conversely, if we start again with no errors but now allow the presence of computational or experimental errors in M_2, this will cause the appearance of oscillating components in g(E) whose magnitudes rise with frequency for a given magnitude of errors in M_2. The maximum observable frequencies are limited by the energy sampling interval. As a result, if part of the M_2 data were weeded out to leave $m' = n$ points and m' was increased from a small value, the calculated distribution g would remain reasonably smooth up to some value m^*, then would start acquiring increasing amounts of spurious oscillations. The number m^* would be approximately the true rank of the matrix A, as we will see. The problem with this approach is that it wastes a lot of data, not using the additional data to provide statistical improvement.

A better approach is to write $Ag \simeq M_2$, where A is our original m x n matrix with m > n and the symbol $\simeq$ means that the norm of the residual vector

$$r = Ag - M_2 \tag{4.27}$$

will be minimized. Using the Euclidean norm, this becomes just a least-squares minimization of an over-determined problem. There are at least three principal methods of solving this problem(4.13, 4.14). The earliest and most common method has been to left multiply by A^T. Since the residual vector $Ag - M_2$ must be orthogonal to the column space of A, we have

$$A^T (Ag - M_2) = 0 \quad \text{or} \quad (A^TA)\, g = A^TM_2 \,, \tag{4.28}$$

which are called the normal equations. The matrix A^TA is square with rank n. Since it is symmetric and nonnegative definite, it can be solved by the efficient Cholesky elimination method(4.10). However, this requires twice the precision in computation that two other methods require which deal direcly with the matrix A.

One method is a relatively recent modification of the well-known Gram-Schmidt orthogonalization procedure and involves a decomposition $A = QR$ with Q an orthogonal matrix and R a triangular matrix. This method requires choosing in advance a value for the rank n, then solving the system. This is fine for a problem where n is known, but that is not the case here. Another approach, the Singular Value Decomposition (SVD) method, has stability properties almost identical with those of the modified Gram-Schmidt orthogonalization, while requiring somewhat fewer arithmetic operations and slightly less storage(4.14). The main reason the SVD method was chosen, however, was that after choosing a value of n larger than needed and solving the system, solutions to the system corresponding to any rank (or more properly pseudorank) are available without further work. In addition there are then available good criteria on which to base the selection of the correct pseudorank.

It can be shown that the matrix A can be decomposed as

$$A = USV^T \tag{4.29}$$

where S is diagonal and is arranged so that its elements are nonnegative and in nonincreasing order(4.14). These elements are the singular values. U and V are orthogonal matrices of rank m and n, respectively, with $m > n$ and computing them comprises the main effort in the SVD method. The columns of V are the singular vectors, which span the space of the solution g. Now the Euclidian length of a vector is unaffected by multiplying it by an orthogonal matrix, so we want to minimize

$$|r|_2 = |U^T r|_2 = |Sp - q|_2 \tag{4.30}$$

where

$$p = V^T g \quad \text{and} \quad q = U^T M_2 \,. \tag{4.31}$$

In expanded form,

$$\begin{bmatrix} s_1 & & & \\ & s_2 & & \bigcirc \\ & & \ddots & \\ \bigcirc & & & s_n \\ \hdashline & \bigcirc & & \end{bmatrix} \begin{bmatrix} p_1 \\ p_2 \\ \cdot \\ \cdot \\ p_n \end{bmatrix} \cong \begin{bmatrix} q_1 \\ q_2 \\ \cdot \\ \cdot \\ q_n \\ q_{n+1} \\ \cdot \\ q_m \end{bmatrix} . \tag{4.32}$$

For the original case considered where n = m we see that the singular value decomposition must give a matrix S which is ill-conditioned, since A is but U and V are both well-behaved. The condition number, which is a measure of the ill-conditioning, is given by the ratio of the largest to smallest (i.e., first to last) singular values, and it was commonly 10^9 or larger for the present data even with n relatively small. It is generally found that the smallest singular values correspond to the most oscillatory singular vectors.

Now consider the minimization problem in (4.32). Computing the norm of the residual vector (the difference between the two sides of the equation), we get

$$|r|_2 = \sum_{i=1}^{n} (s_i p_i - q_i)^2 + \sum_{i=n+1}^{m} q_i^2 \ . \tag{4.33}$$

Clearly, the norm will not be smaller than the second sum on the right side above, but it can be kept no larger than that by setting each term in the first sum on the right to zero:

$$p_i = \frac{q_i}{s_i} \ , \ i = 1, \ldots, n. \tag{4.34}$$

However, the oscillatory components are still included. We now need to use our estimate of the level σ of error in the data M_2, and hence in q (since q is only a rotation of M_2 by the orthogonal matrix U^T, equation (4.31)). Then the uncertainty in each p_i will be given by

$$\Delta p_i = \frac{\sigma}{S_i} \tag{4.35}$$

from (4.34). Generally, it is found that for some number k the first k elements of p will exceed their uncertainty while the remaining ones will not. These last elements might well be zero or of the opposite sign due to the errors in the M_2 data. Consider the possibility of replacing them with some other value, e.g., zero. This changes the solution, but it was not good anyway. The last elements of p control the amount of the last, most oscillatory singular vectors introduced. This is because g = Vp from (4.31) so p_i controls the amount of the ith singular vector contributed to g. We are not introducing arbitrariness into the solution vector g beyond that already present due to data uncertainty. Although the p_i for i = k + 1. ..., n could be set to some nonzero value within the uncertainty limits, zero values have the attraction of being simple, eliminating the most oscillatory components from g, and minimizing the norm $|p|_2 = |g|_2$. Note from (4.34) and (4.35) that if $p_i < \Delta p_i$ then $q_i < \sigma$, so the cutoff value of k can be found simply be scanning down the q vector until the elements get smaller than σ. Other methods exist for choosing k(4.14) but they are related to those above and usually give about the same answer.

The SVD subroutines of Lawson and Hanson(4.14) were used after generating the matrix A. The singular values, p and q vectors, the norms of the g and residual vectors, and the latter normalized by $1/(m-k)^{1/2}$ were all displayed, along with the V matrix if desired. In addition the g vectors were computed and displayed for each choice of k from 1 to n. Typical solutions g_k for several k values with the mode 1 data of the $c = 0.86$ sample are shown in figure 4.10. The continuous curves are the same interpolated curve actually generated in the computation.

Estimation of the uncertainty in the data is complicated by the fact mentioned earlier that the error tended to be a given fraction of M_2, hence largest in magnitude at the peak. It is possible to scale each equation in (4.25) by the inverse standard deviation of M_{2i} so that all M_{2i} have the same resulting error. However, this emphasizes the accuracy of the solution g in the low-amplitude tails at the expense of accuracy at the peak, while we are at least as interested in the behavior near the peak as in the tails. On the other hand, when this is not done the error in g contains large- and small-error components mixed together, complicating the choice of k. The error was at first conservatively estimated as that of the peak, but the k value chosen on

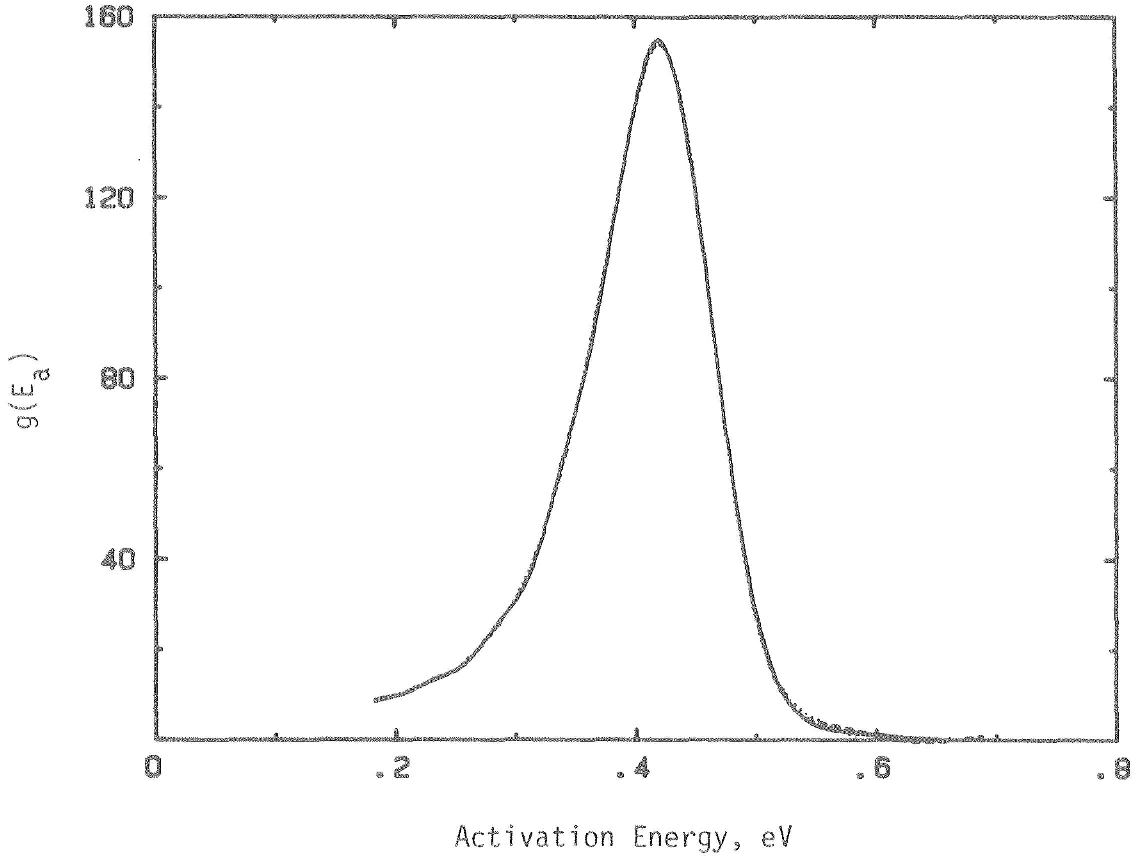

Figure 4.10 Computed solutions g_k for the distribution of activation energies for mode 1 on $(Zr_2Pd)_1H_{.86}$, using pseudorank values k as follows. ——, k=13. ---, k=14. ..., k=16.

this basis was usually smaller by 2-4 than what seemed to be the optimal solution based on examination of the solutions. For example, it was frequently found that for both lower and higher than optimal k values the solution went significantly negative in places and was more oscillatory than for one or a few optimal solutions. Negative probabilities or distribution functions normally being frowned on, their avoidance where possible was finally settled on as a criterion supplementary to those described above in deciding on k. Actually, since for reasonable k values the (slightly) negative values only occurred at the highest energies where g(E) had essentially gone to zero, this criterion was nearly equivalent to looking for minimally oscillatory solutions in that region. Any negative excursions were required to be smaller relative to the peak height than the relative uncertainty level. There exists an SVD algorithm which incorporates linear inequalities as constraints which could have been used to ensure that all solutions were nonnegative at the points E_j(4.14), but it does not seem to be perfected yet(4.15).

The selected pseudorank values for the various data sets taken from 77 K up lie in the range 13 -18. The question of which initial value of n should be used still remains. It was found empirically that n needed to be greater than k by at least 1 or 2 to avoid introducing spurious behavor, and that as (n-k) got large, the solution at a given k very gradually became slightly oscillatory. For all the data taken from 77 K to 370 K, n was set at 20.

To check the inversion another program was written to recompute $M_2(\omega,T)$ from the calculated g(E). Comparison of the results with the original data for the first mode of the c = 0.86 sample showed that the maximum error was 0.5% of the peak height, while the average error was about one-half of that. The sum of the squares of the errors agreed exactly with the value computed by the SVD routines. This showed that the SVD program worked correctly and provided quite accurate solutions.

The final Zr_2PdH_x g(E) solutions are shown in figures 4.11 to 4.14. Note the generally good agreement of the calculated g(E) for the three frequencies of each sample. They should be identical apart from uncertainty in the data, assuming the sample to be homogeneous. Sample inhomogeneities would be reflected in the data since for different vibration modes the nodes and regions of maximum curvature occur in varying locations. The $Y_{64}Fe_{36}$ samples cut from foils might be expected to display more of this while the melt-spun Zr_2Pd ribbons should be relatively homogeneous. Those that were hydrogenated should also be fairly homogeneous with respect to hydrogen content due to its high mobility.

The exact energy scale for the unhydrogenated Zr_2Pd is uncertain because it depends on the assumed value of τ_0. A change by a factor of 2 in τ_0 causes only about a 3% change in the position of the $g(E_a)$ peak, however.

For some reason the inversion of the unhydrogenated sample's data was much less stable than for any of the other data. It is clear even from the internal friction data, figure 4.1, that there is a low temperature shoulder on the peak and this shows up in g(E), but there is significant oscillation with an amplitude of about 3.5% in all solutions, making the distinctness of the two sub-peaks uncertain. For no value of k is there a region where several adjacent k values give very nearly the same curve to within a small fraction of 1%, as for the other data sets. A value was chosen which seemed to generally minimize this

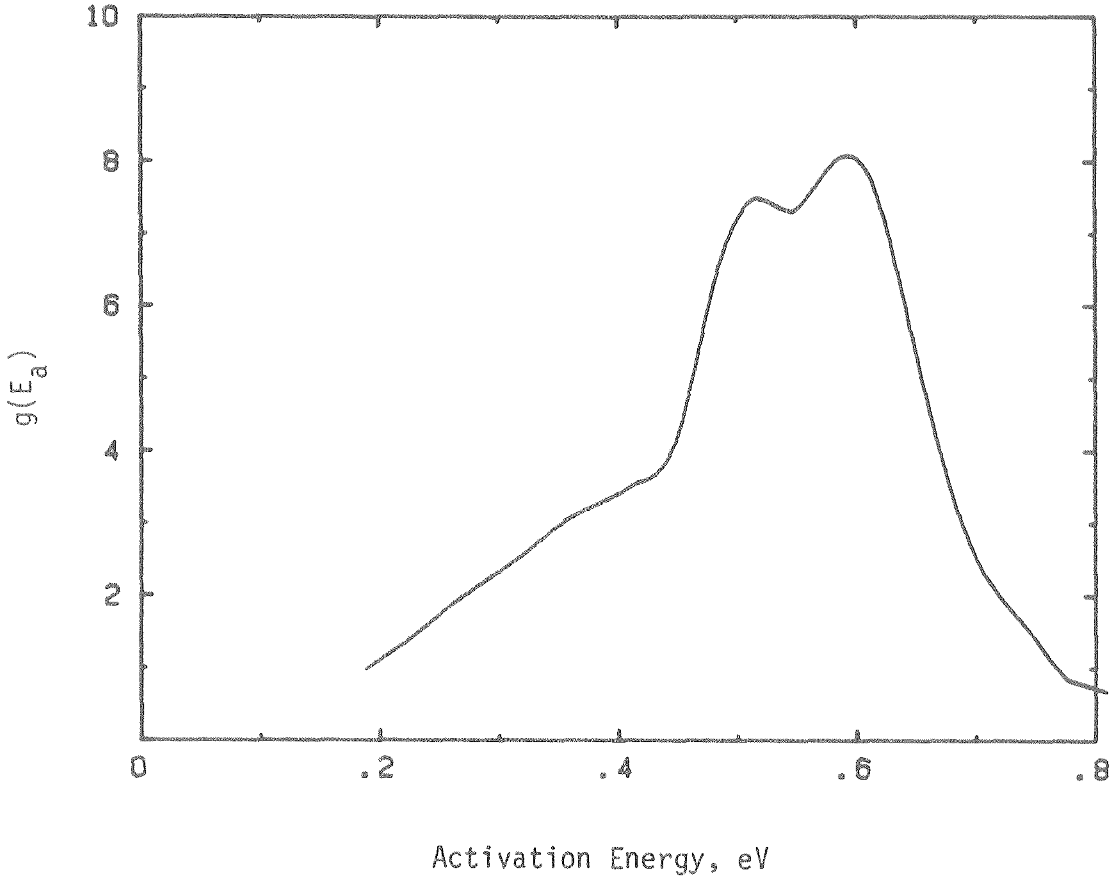

Figure 4.11 Distribution of activation energies for the relaxation strength due to hydrogen hopping in unhydrided a-Zr_2Pd, second vibration mode. Error is approximately the linewidth.

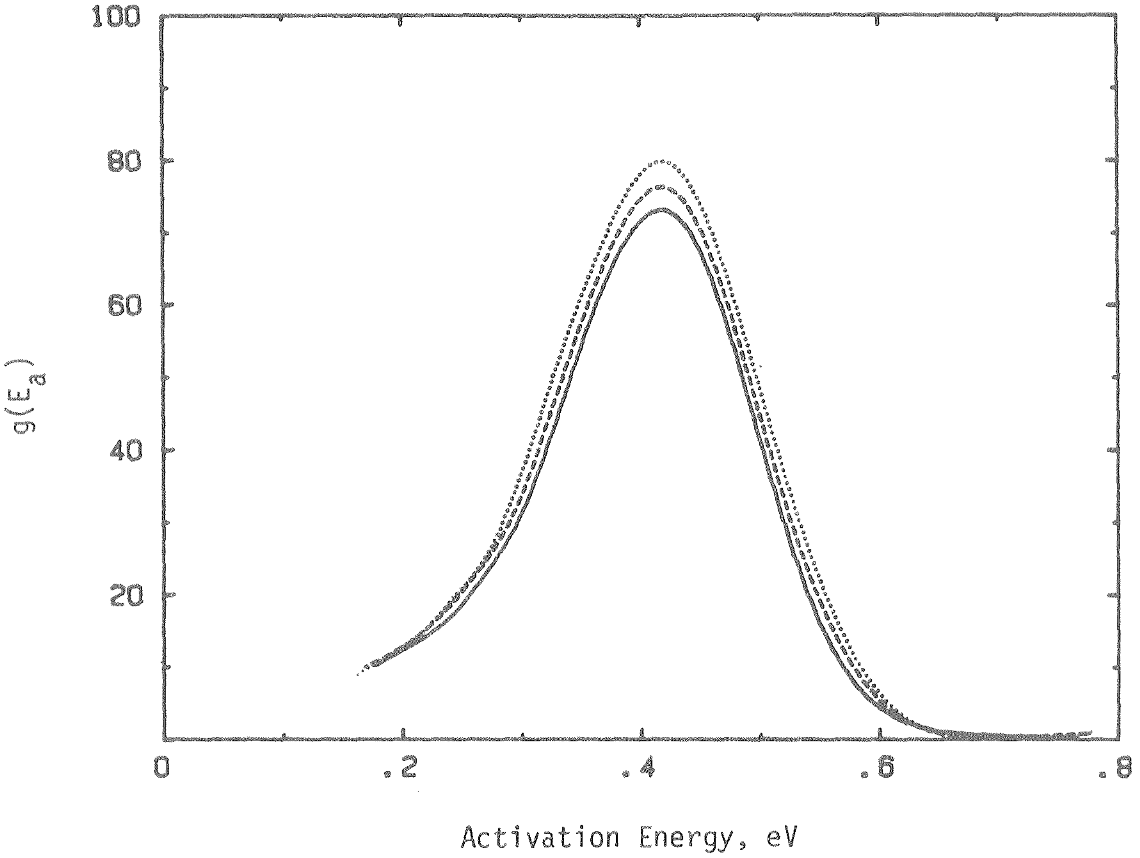

Figure 4.12 Same as figure 4.11 for the first 3 vibration modes of $(Zr_2Pd)_1H_{.23}$. ——, first mode. ---, second mode. ...., third mode.

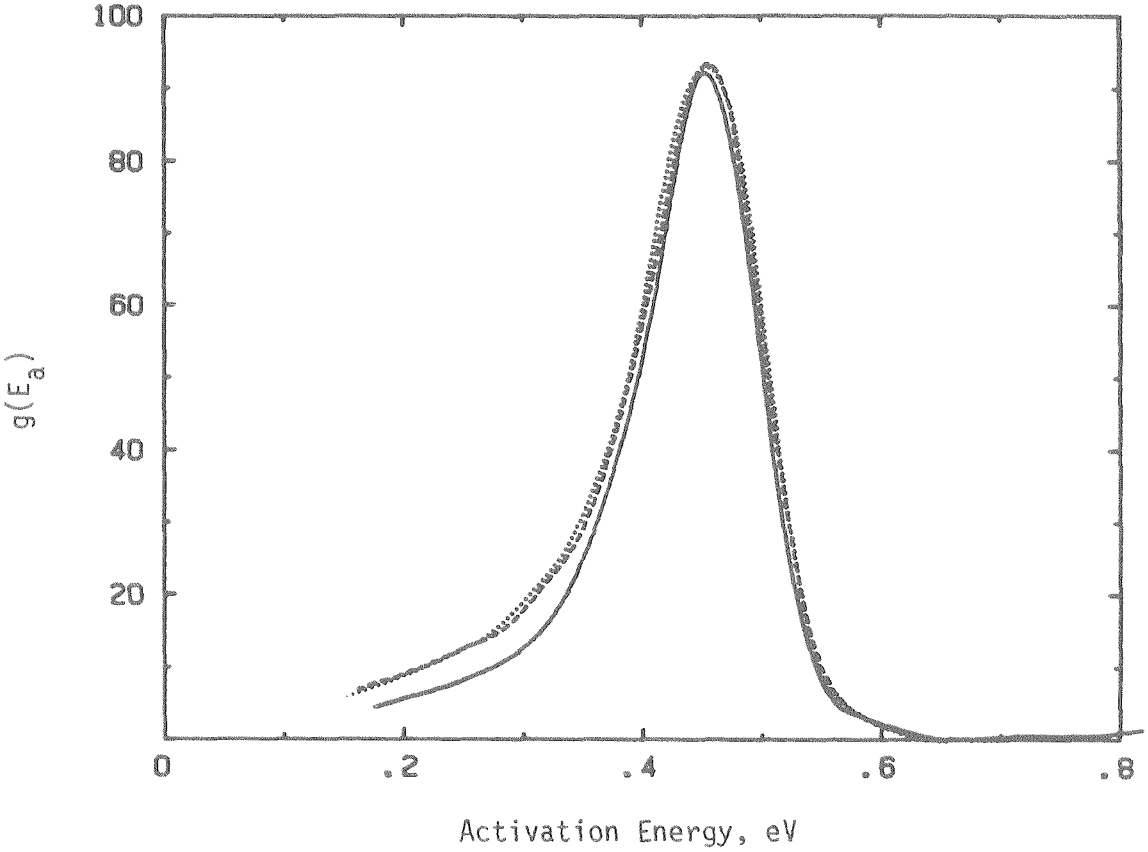

Figure 4.13 Same as figure 4.12 for $(Zr_2Pd)_1H_{.64}$.

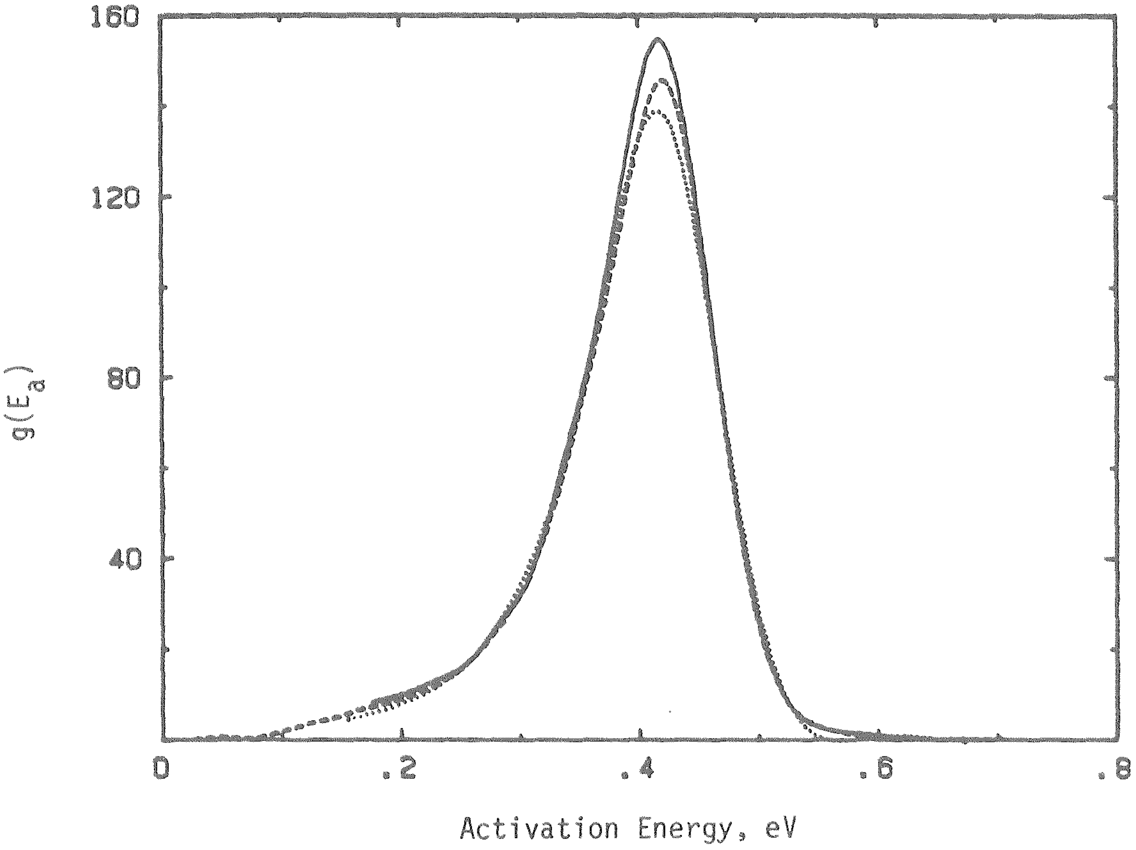

Figure 4.14 Same as figure 4.12 for $(Zr_2Pd)_1H_{.86}$.

oscillation. The oscillation is most likely due to the significantly higher uncertainty in this early data.

For the $Y_{64}Fe_{36}$ data the peak falls squarely on the lower end of a rapidly rising exponential background, apparently of the type discussed earlier in this chapter, resulting from the metal atoms themselves beginning to become mobile. Attempts were made to self-consistently subtract off the background, but there was a fair amount of uncertainty because the measurement did not really go high enough to reach the region where the rising background was completely dominant. Even worse, annealing was taking place at the upper temperatures, causing the background to change rapidly. When inversion of the data was carried out, the resulting g(E) was naturally sensitive in the high-energy region to the details of the background subtraction. Hence the results are not very meaningful and are not reproduced here.

V INTERPRETATION

5.1 PEAK REGION OF ACTIVATION ENERGY DISTRIBUTION

5.1.1 Type of Relaxation Observed

Probably the most fundamental question about the internal friction peaks observed in Zr_2PdH_x is the source of the relaxation. Figure 5.1 displays g(E) for the second mode of each of the four Zr_2PdH_x alloys, drawn to the same scale. The second mode was chosen because it generally has the smallest level of uncertainty, as mentioned before. In addition that comprises the only complete set of data for the unhydrided a-Zr_2Pd and the most complete set (down to 10K) for the c = 0.86 alloy. Clearly, the relaxation is related to the presence of hydrogen, but there are still several possibilities. The relaxing defect could be a single hydrogen atom hopping between sites with elliptical strain dipole tensors oriented in different directions (a Snoek relaxation), a pair of hydrogen atoms (a Zener relaxation), or a hydrogen-impurity pair such as H - O or H - N reorienting by the the hopping of the hydrogen atoms to a different but still neighboring site. All of these point defects are seen in crystalline hydrides. In addition, it could conceivably be related to other relaxations seen in crystalline materials such as those due to hydrogen dragged by moving dislocations (if one accepts the possibility of dislocation-like defects in amorphous metals). To answer this question we must look at certain features of the data.

Toward this end, a number of parameters calculated from the data are displayed in table 5.1. The values of τ_0 were calculated by least-squares fit to the 1/T shift for different vibration frequencies as

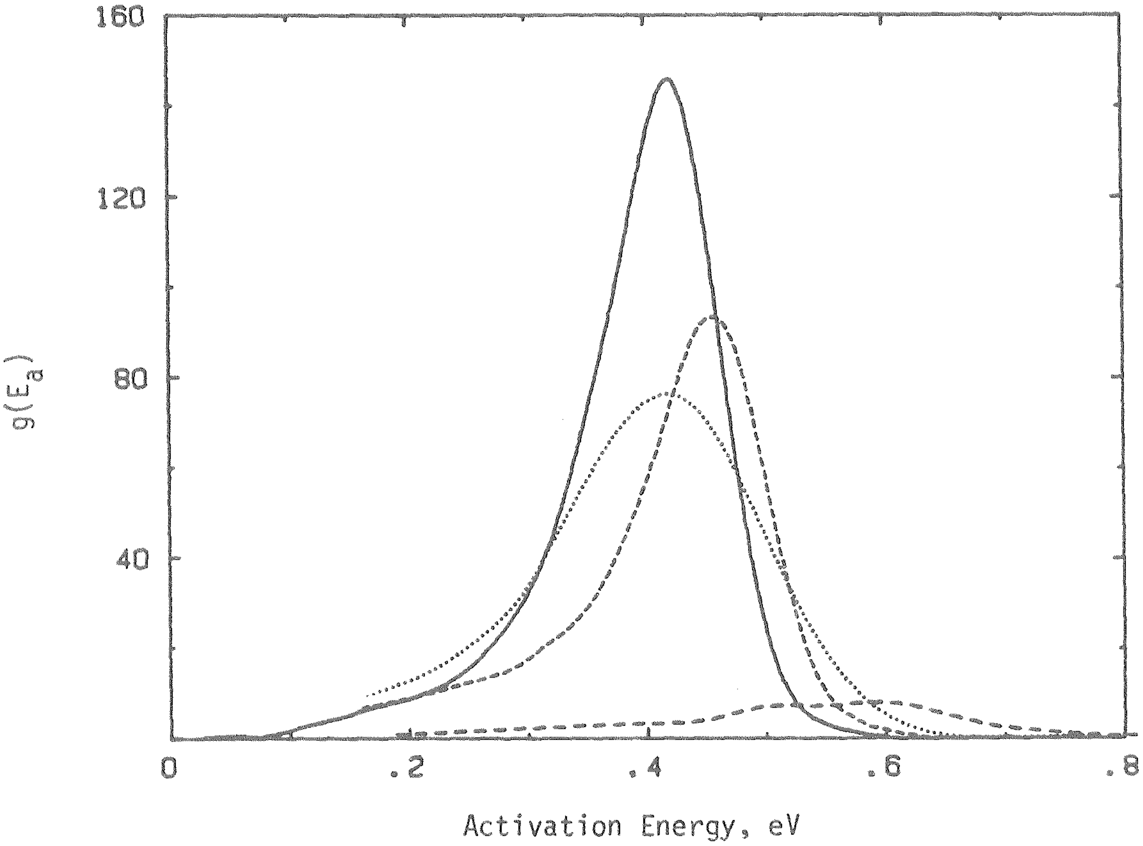

Figure 5.1 Comparison of the distribution of activation energies for the second vibration mode of four $(Zr_2Pd)_1H_c$ alloys. — — —, c ≈ 0. ....., c = 0.23. ----, c = 0.64. ——, c = 0.86.

TABLE 5.1

Parameters for the distribution of relaxation strength over activation energy in $(Zr_2Pd)_1H_c$ for the second vibration mode measurements.

c	~0	0.23	0.64	0.86
$\tau_o \times 10^{14}$, s	0.4	0.6	1.3	1.5
E_{max}, eV	0.52, 0.59	0.42	0.45	0.42
$g(E_{max})$, eV^{-1}	8.1	76	93	146
FWHM of $g(E_a)$, eV	0.22	0.20	0.12	0.12
$\Delta\lambda$	—	0.08	0.04	0.03
pseudorank k used:				
mode 1		11	15	13
mode 2	15	11	17	22
mode 2		10	18	14

described in chapter 4. As already mentioned, the value for the hydrided sample is an assumed value. The value E_{max} is where g has its peak. For the double peak of the unhydrided sample both peak positions are shown, without correction for the presence of the other peak since the peak shapes were unknown. The maximum relaxation strength $g(E_{max})$ and full width at half maximum of the g(E) peak are given next, followed by an estimate of the ellipticity of the strain dipole tensor, and the pseudorank k used for calculation of each g.

The strain dipole ellipticity was calculated from the total integrated relaxation strength as follows. We can write equation (2.13) for a single relaxation as

$$\Delta = \frac{\delta M}{M_R} = \beta \frac{c}{M_R V_o kT} (\Delta P)^2 = \beta \frac{cV_o M_u}{kT} (\Delta\lambda)^2 \qquad (5.1)$$

where ΔP or $\Delta\lambda$ are a measure of the ellipticity of P or λ, respectively, and β is a geometrical factor that includes $1/n_t$ and the details of the term in the square brackets of equation (2.13). For polycrystalline metals β falls around 0.1, within a factor of less than 2, and this value has been suggested by Berry and Pritchet for amorphous metals(5.1). For a distribution of relaxations Δ becomes $\frac{1}{T}\int g(E)dE$. Then we have

$$(\Delta\lambda)^2 = \frac{k}{cV_o M_u \beta} \int g(E)dE \,. \qquad (5.2)$$

The value of the modulus is taken from Table 4.1, since its inaccuracy is less than that of β, and in any case it is the only estimate presently available. If the uncertainty in β is a factor of 2 the uncertainty in $\Delta\lambda$ is a factor of 1.5.

From the density measurements of Bowman, Rosker, and Johnson(5.2) on the alloys Zr_2Pd and $(Zr_2Pd)_1H_{.94}$ the change in volume is $\Delta V/V = 0.12$. If $\lambda_1 = \lambda_2 = \lambda_3 \equiv \lambda$ as it should in an isotropic material, we get $\lambda = .042$. If λ is a function of c (it frequently is in crystalline materials, falling off at high c by an amount of the order of 10%), it may be larger at low c. For the c = 0.86 specimen we see that the value calculated for $\Delta\lambda$ is 0.03, while for c = 0.23 it is 0.08, larger than λ itself. We recall from Chapter 1 that λ is a macroscopic parameter defined by the change in strain per change in defect concentration. In a single crystal λ_{ij} can be anisotropic but in an isotropic polycrystalline material the measured value will be isotropic. In the same way glassy metals must have locally anisotropic hydrogen strain dipole tensors or there would be no internal friction peak. In this case it is not constant over a crystal domain but describes only one defect site. Since $\Delta\lambda$, which is an averaged measure of its local asymmetry, is as large as λ we see that locally some components may be roughly twice the average value. It is interesting to note that the present values of $\Delta\lambda$ are a factor of 3-6 smaller than the value 0.2 calculated by Berry and Pritchet(5.1) in the same way for amorphous Nb_3Ge.

Returning now to the question of the type of relaxation seen here, we see from the table that the τ_0 values are of the order of 10^{-14} s, increasing slightly with hydrogen concentration. These are in the range expected and commonly observed as the attempt frequency for a point defect relaxation, and rule out any other type of relaxation. Given this, then, we still have several possibilities to decide among. We now examine the dependence of the defect concentration on temperature and hydrogen concentration.

For a hydrogen pair (H-H) or higher (n-atom) cluster defect in the dilute limit, the defect concentration will be(5.3, 5.4)

$$c_{nH} = \alpha\ c_H^n \exp\ (-\Delta g_{HH}/kT) \tag{5.3}$$

where α is a constant related to the coordination number for hydrogen sites about each other, Δg_{HH} is the hydrogen-hydrogen binding energy caused by the lattice-mediated attractive interaction discussed in Chapter 1, and C_H is the concentration of single hydrogen atoms.

For a hydrogen-impurity (H-I) pair, also in the dilute limit for both hydrogen and the impurity,

$$c_{HI} = \alpha'\ c_H c_I \exp\ (-\Delta g_{HI}/kT) \tag{5.4}$$

where c_I is the impurity concentration. However, things are really more complicated than this. As the hydrogen concentration approaches and surpasses the impurity concentration, the number of H-I pairs will saturate. Each impurity may be surrounded by z hydrogen sites but each of these can be occupied only by either 0 or 1 atoms, giving a maximum of zc_I pairs. Further, the interaction energy Δg_{HI} is a negative energy that causes hydrogen to be bound or trapped by the impurity, and it will be a distributed quantity. The distribution is likely to cover a range of energies greater than kT at temperatures of interest. Thus, a Fermi-Dirac distribution is needed to describe the occupation of sites. Finally, as long as we are discussing trapping of hydrogen by impurities in these deeper than average wells we might as well include all traps, such as the larger interstitial holes discussed in Chapter 1. These sites may have a lower potential energy since they have a larger radius. The local dilatation induced by hydrogen and hence the lattice strain energy will then be smaller, provided that the metal atoms involved are the same. If they are not, for example if Zr_4Pd_2 octahedra but no Zr_6 octahedra can be found, this would not necessarily be the case. Furthermore, the increased coordination number in the larger polyhedral holes may have an effect on the ground state energy, due to chemical bonding effects for an interstitial such as hydrogen.

Actually, there is no reason not to go ahead and include all sites, tetrahedral, octahedral, or impurity traps. The computer models of Finney and Wallace$^{(5.5)}$ and Ahmadzadeh and Cantor$^{(5.6)}$ show that the distribution of hole sizes is bimodal, apparently resulting from the existence of only tetrahedral and octahedral sites in their relaxed soft potential monatomic computer models, as we recall from figure 1.5. This should yield a bimodal distribution n(G) for the density of sites with ground state free energy G. The total hydrogen concentration will be

$$c = \int \frac{n(G)}{1+\exp\left(\frac{G-\mu}{kT}\right)} \, dG \; . \qquad (5.5)$$

If kT is small compared to the energy range of n(G), the Fermi-Dirac distribution can be replaced by a step function.

Interestingly, Kirchheim, Sommer, and Schluckebier$^{(5.7)}$ have made electrochemical measurements of the chemical potential of hydrogen in several metal-metalloid glasses. They analyzed their data assuming a Gaussian for n(G) and were able to fit their data at higher H concentrations by adjusting its center value G_0 and standard deviation σ. The calculated values of σ were in the range of .14 to .18 eV. However, at concentrations below $c = 10^{-3}$ the results deviated strongly from the theoretical curve, indicating excess deep traps numbering about 0.1% per metal atom. It is interesting to speculate that these may represent a few larger hydrogen sites left over after the metalloid atoms fill most of these large sites.

Next we consider the case of H pairs at high concentrations where (5.3) is no longer valid. The best treatment to date stems from Le Claire and Lomer(5.8), who considered binary crystalline disordered (substitutional) alloys of elements A and B. This analysis can be applied to the present case by allowing A and B to refer to empty or full hydrogen sites. Although next nearest neighbors appear to be frequently at least as important as nearest neighbors for Zener relaxations(5.3), Le Claire and Lomer originally used only nearest neighbor interactions. For each of the z/2 directions i to a nearest neighbor, where z is the coordination number, the fraction σ_i of AA bonds is used as an order parameter. The fraction of AB and BB bonds along direction i can be expressed in terms of σ_i, and these can be used to build a calculation of the anelastic relaxation strength just as in Chapter 2, by substituting them for the concentrations c_ν of the simple defects oriented in direction ν. The only difference is that the sum of the σ_i along different axes is not conserved as in equation (1.1). Instead the quasichemical approximation

$$\frac{n_{AA}\, n_{BB}}{(n_{AB})^2} = \frac{\sigma_i\,(1-2c+\sigma_i)}{(c-\sigma_i)^2} = \exp\,(-\Delta g/kT) \qquad (5.6)$$

is used to give the dependence of the order parameter on temperature. Here, g is the free energy G per atom. The final result is

$$\delta M = \frac{1}{V_o} f(\sigma_o, c) \frac{c^2(1-c)^2}{kT} \sum_{\nu} (P^{\nu})^2 \tag{5.7}$$

with σ_o the value of the σ_i at zero stress, which is similar to (2.13) but with c/n_t replaced by $f(\sigma_o, c)c^2(1-c)^2$. $f(\sigma_o, c)$ is a function which is zero for complete long-range order and 1 for complete disorder, and it shows an $\exp(-\Delta g/kT)$ behavior because of its dependence on σ_o. Other improvements can be made but this is sufficient for the data at hand.

We are now prepared to examine the question of which type of defect causes the main peak in the anelastic relaxation seen here. Impurity traps can be ruled out as an explanation of the main peak in g(E) because the number of such pairs saturates at the impurity concentration, while no such saturation is seen up to c = .86. To check for hydrogen pairs we need to check the height g_{max} of the peak in g(E) as a function of T and c. We expect a binding energy of the order of 0.1eV for the H pair. Values from .065eV to 0.22eV have been reported, for example, in crystalline N_b(5.4, 5.9). Figure 5.2 shows the value of g_{max} plotted versus $1/T_{peak}$ for the three modes of the c = 0.23, 0.64, and 0.86 hydrides. The very slight temperature dependences and the wrong sign of the slope for c = 0.23 argue against the pair hypothesis. A quick calculation of Δg shows that its magnitude would be less than 0.01 eV for all samples. Even more striking is figure 5.3 which does not agree well with a $c^2(1-c)^2$ dependence. We conclude that we are most likely seeing a Snoek relaxation, as have other workers with $Pd_{80}Si_{20}$, $Nb_{40}Ni_{60}$, $Pd_{77.5}C_{46}Si_{16.5}$ and other glasses.(5.10, 5.11, 5.12)

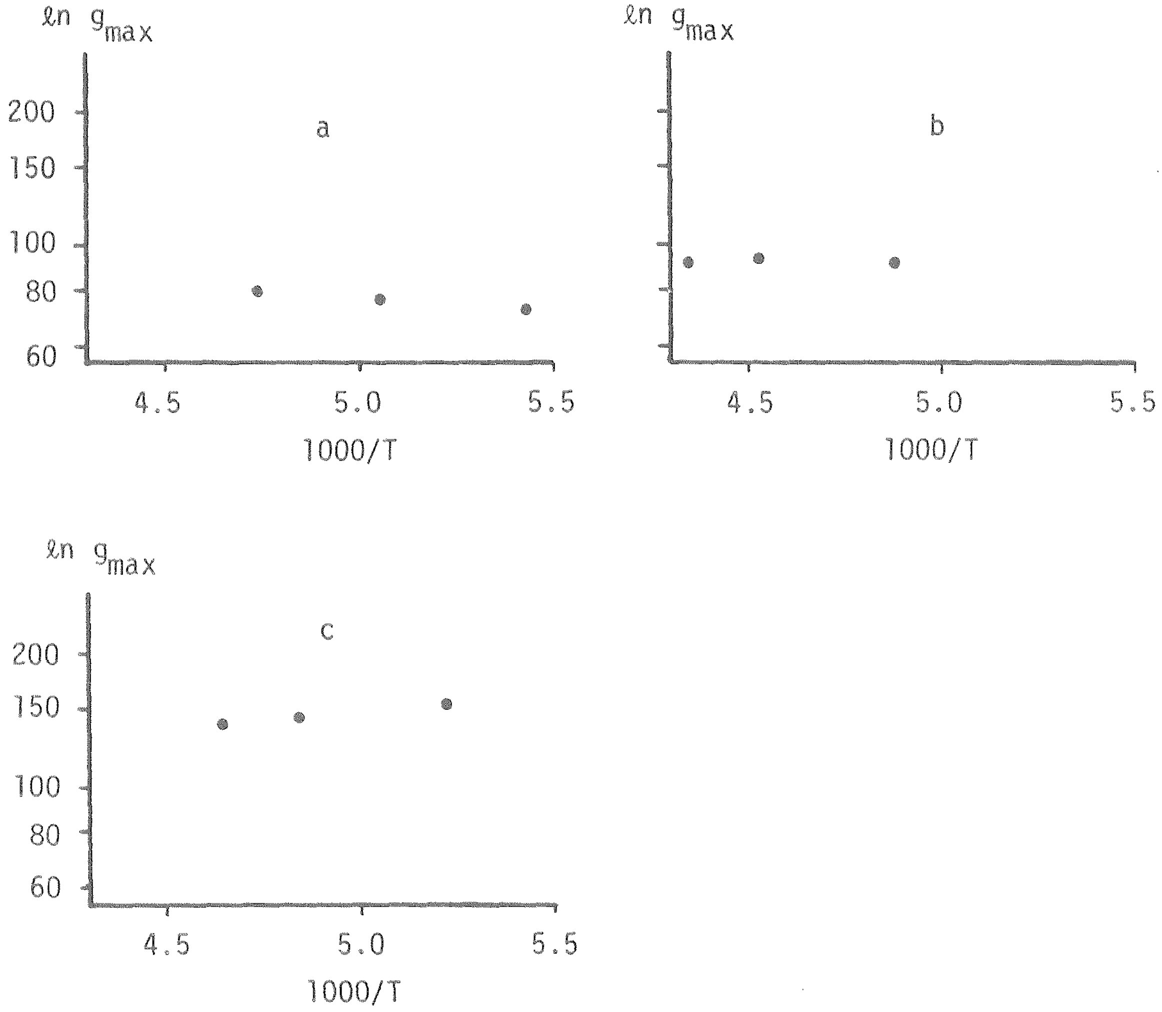

Figure 5.2 Plots of the log of the maximum of $g(E_a)$ against 1/T, second vibration mode. a). c = 0.23. b). c = 0.64. c). c = 0.86. Errors are much smaller than the dots.

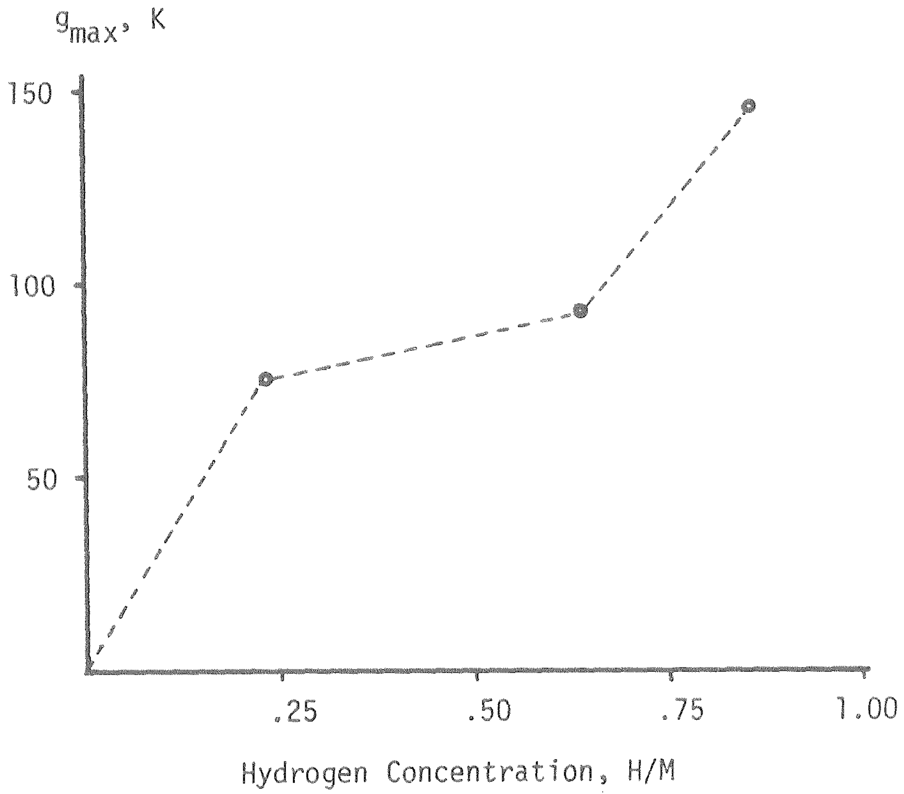

Figure 5.3 The concentration dependence of the maximum value of $g(E_a)$ for the three specimens where c is known, second vibration mode. Errors are much smaller than the circles.

5.1.2 Behavior of the Peak

Figure 5.3 displays a dependence of g_{max} on c that is not very simple. If instead we had plotted the integral of g(E), the point at c = 0.23 would have been raised even higher relative to those at the higher concentrations because its peak is much broader. In figure 5.4(a), the positions E_{max} of the maxima in g are plotted vs. c, including two values for the double peak of the nominally c = 0 data. The latter are plotted at a c value which is only a crude guess based on the assumption that, for this and the c = 0.23 data, g_{max} is proportional to c. Then in figure 5.4(b) the full widths at half maximum of the peaks are plotted vs. c.

In each of these last three figures it appears that the two lower concentration peaks belong to one family while the two higher ones belong to another. To allow better comparison of the intrinsic shapes of the peaks, in figure 5.5 they have all been scaled to unity height and shifted versus energy so that their upper toes coincide, to the extent possible. The upper two concentrations' peaks are remarkably close in shape, and the lower two are much more similar to each other than to the former two. It would seem plausible that between c = 0.23 and c = 0.64 a change has occurred in the metal lattice or in the nature of the relaxing defect.

The nature of this change is not clearly understood yet. From the results of x-ray diffraction(5.13) and soft x-ray emission spectroscopy(5.14) experiments described near the end of chapter 1, it is clear that the hydrogen is surrounded almost exclusively by Zr atoms up to at least c = 1. Therefore, this is not the cause of the differences seen

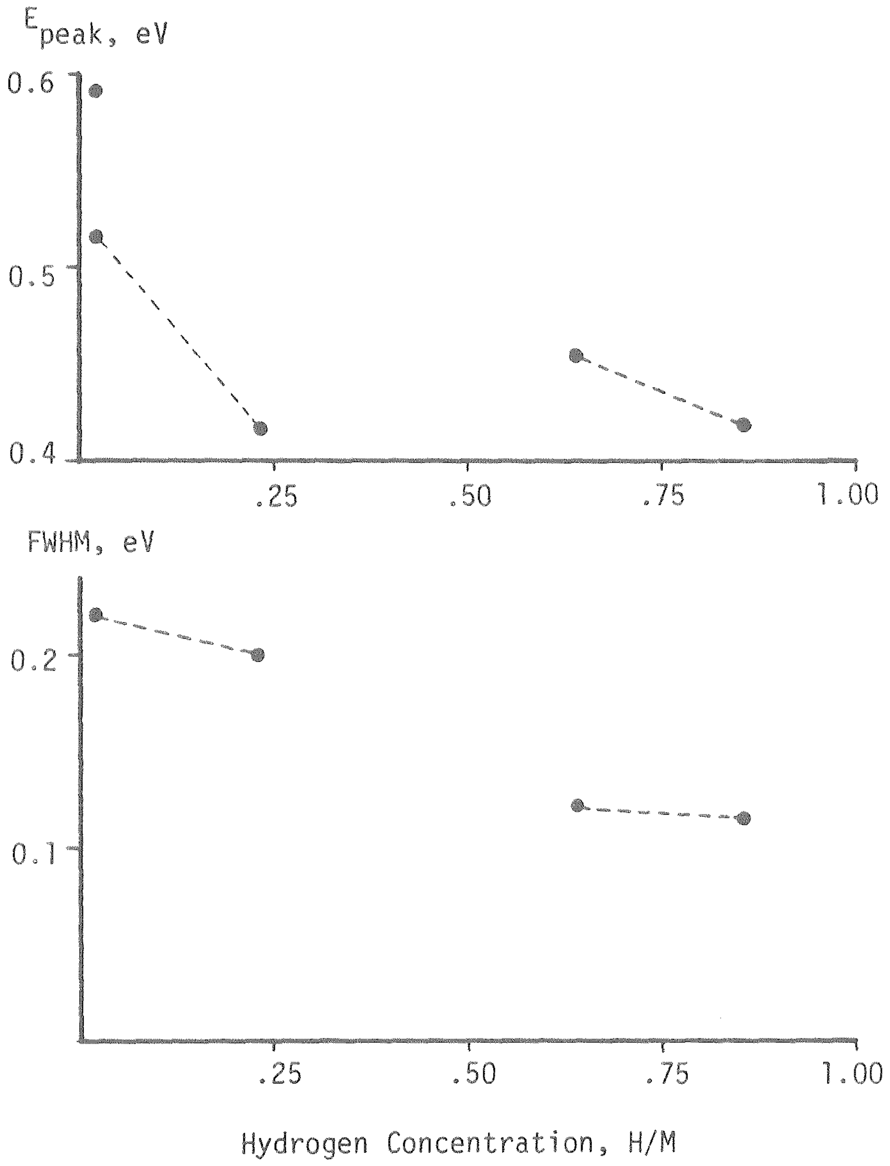

Figure 5.4 a). Concentration dependence of the position of the peak in $g(E_a)$, second vibration mode. The c value used for the alloy with c ≈ 0 is a rough estimate (see text). Errors due to uncertainty in τ_o are about the diameter of the dots. b). The full width at half maximum for the same peaks. Dotted lines are for emphasis only.

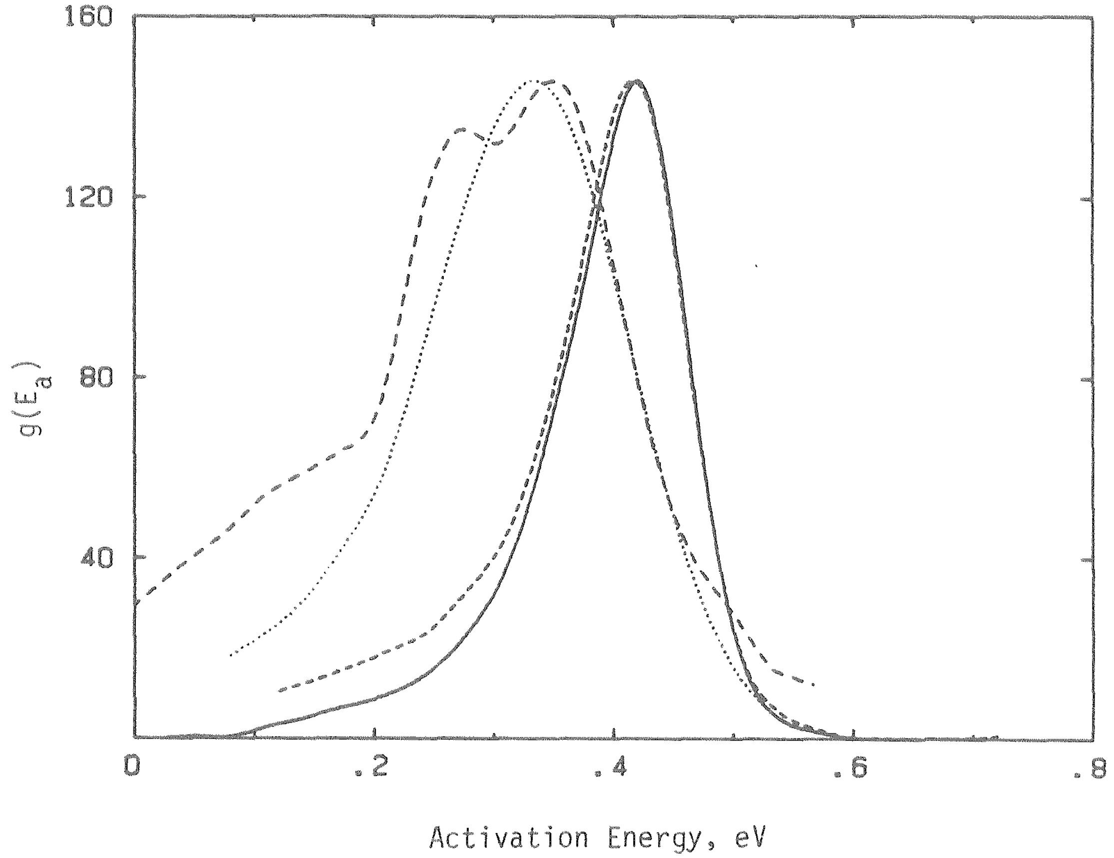

Figure 5.5 The distribution of activation energies for the second vibration mode of the four alloys of figure 5.1, scaled to unity height and shifted in energy to bring their upper toes into approximate coincidence, in order to allow comparison of the peak shapes. — — —, c ≈ 0, shifted by 0.242 eV. ....., c = 0.23, shifted by 0.084 eV. ----, c = 0.64, shifted by 0.039 eV. ——, c = 0.86, unshifted.

between the low and high c peaks. It would appear that at large c the amorphous alloy is forced to undergo some sort of structural reordering. This conclusion is based on the above evidence in addition to the x-ray results just mentioned, and shown in figure 1.3. When hydrogen was added to near the $c = 1$ level, the Zr-Zr distances increased while the Zr-Pd and Pd-Pd distances were almost unaffected. It is impossible for simple homogeneous expansion to explain this result: Local motions of Zr atoms relative to Pd atoms are required aside from that. This type of structure change has an analog in the changes in crystal structure seen in crystalline alloys as c increases.

Another feature of figure 5.1 is that as c increases, the $g(E_a)$ curve decreases continuously in height at high E_a values, while it increases at low values. This is in sharp contrast to the behavior of an amorphous $Zr_{76}Ni_{24}$ alloy reported by Agyeman et al.(5.15) where, as more hydrogen was added, the internal friction curve followed the previous curves on the high temperature side but then diverged upward near the peak and below to yield a higher, broader peak, shifted to lower energies. In a-Nb_3Ge the peak was found merely to grow everywhere without appreciable shift in temperature(5.1). But in $Nb_{40}Ni_{60}$(5.11) and $Pd_{77.5}Cu_6Si_{16.5}$(5.10) the behavior found was similar to that described here. Several explanations are possible.

The first and only explanation which has been advanced to date(5.10) is the filling of the deepest wells first as described above in equation (5.5), coupled with a correlation between well depth G and activation energy. One simple model used, for example, is that pictured in figure 5.6 where all the barrier heights are equal. Then E_a just varies inversely with G, and the initial filling of deep wells leads to the

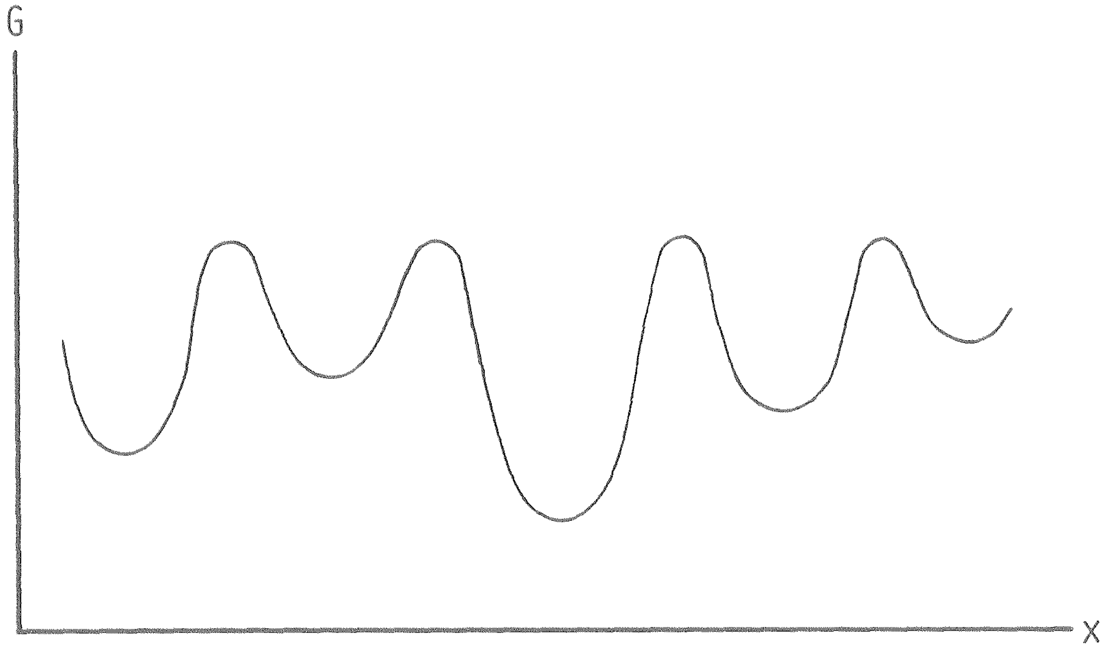

Figure 5.6 A schematic representation of a model for the potential energy wells in a glassy metal. All maxima have the same energy but the energies of the minima are distributed.

initial appearance of high E_a values. This would nicely explain the $Zr_{76}Ni_{24}$ data mentioned above. However, though there is undoubtedly a certain amount of truth in this picture, it is a rather poor approximation. Due to the greater steepness of the hydrogen-metal pair potential at small distances, the saddle point energy will be more sensitive to fluctuations in these distances than will the energy at the minimum. Therefore, there should be a distribution of saddle-point energies as wide as or wider than the distribution of energies at the minima.

A much more sophisticated calculation has been done by Richards(5.16). He has derived an approximate relationship between the sum of the edge lengths of tetrahedral and octahedral sites and their interstitial site energies, using several simple pair potentials. He did the same for the relationship of the perimeter of these sites' triangular faces to the saddle point energy for a hydrogen atom passing through these faces. He then represented the first peak of an RDF by a Gaussian and applied this to the calculation of the distribution of the above total edge lengths, and hence the site or saddle point energies. He focused only on hopping through triangular faces, ignoring square faces, and got a nearly symmetric distribution of activation energies. Doing this for amorphous $Pd_{80}Si_{20}$ he got a distribution whose mean could be adjusted to agree with that of the experimental data. The width he calculated was somewhat too wide to fit the data. He also took into account the correct filling of the wells. According to his calculation the well depth and the activation energy are statistically correlated. As a result, when the hydrogen concentration increases, the center of the peak in the distribution of activation energies moves to lower energy while its width increases somewhat, as we expect. Of course, the distribution of all sites, occupied and unoccupied, is still independent of c.

We see, however, that this well-filling ideas does not explain the present data in which g(E) decreases radically at high E_a while it increases at lower E_a. This effect has sometimes been explained as being due to the mutual blocking effect of hydrogen atoms in neighboring deep wells which keep the atoms in a given deep well from hopping. However, this would require that most of the nearest neighbors of a deep well also be deep, which is almost certainly not true since it would require macroscopic separation of the material into large regions with either deep or normal wells. And in any case, even if it were true, the apparent minimum separation requirement mentioned in Chapter 1 which prevents H-H distances of less than about 2.1 Å might keep the nearest neighbor sites empty. Also it could well be true that adjacent deep wells are connected by unusually low rather than high E_a barriers, as we will see below. Finally, this idea leads to an apparent width of $g(E_a)$ which increases with c, while the present data do the opposite. In sum, this approach appears almost worthless for explaining the data here.

A second explanation exists for the downward motion of the upper toe of g(E) with c, as follows. The known lattice expansion caused by hydrogen will, as argued above, affect the saddle point energies more strongly than the energies at the minima. Their difference, E_a, will without question decrease with expansion. The only question is whether this effect is large enough to account fully for the observed decrease in E_a.

The third possibility is that the changes in the chemical potential due to the excess potential $\Delta\mu_H$ introduced in equation (1.16) might be responsible. The proton part of this, related to the lattice strain energy, is essentially just the second explanation above. However, the electronic part could also produce the observed results by affecting the saddle point and minimum differently as a function of c. Recall that in Pd, part of the electrons go into the existing d and s bands at the Fermi level and part go into newly created semilocalized screening states near the bottom of the s band. If this picture holds in other metals, surely the former electrons would not be appreciably affected by a change in position of the H atom from minimum to saddle point. The question is whether the screening electrons will be affected by c. The answer, in Pd at least, is yes. As the 4d band gets filled, the density of states at E_f goes down sharply. Meanwhile, in the simplest approximation of the Friedel model the screening falls off exponentially with distance, with a decay length(5.17)

$$r_0 = [4\pi\varepsilon_0^2 \; D(E_f)]^{-\frac{1}{2}}. \tag{5.8}$$

When this radius gets long enough that the screening charges of two ions (i.e., the proton and a metal ion) interact, the energy rises. This should happen first and most strongly at the saddle point, raising the activation energy. Conversely, if E_f lies in a region where D(E) is increasing with E, an increase in E_f would reduce the screening length and might lower the activation energy. In Zr_2PdH_x the superconducting critical temperature and magnetic susceptibility, which should be proportional to $D(E_f)$, both go down by about a factor of 2 as c goes from 0 to 1. Hence the screening length will increase with c and the activation energies should go up, rather than down as observed. We conclude that the only viable explanation is the lattice expansion.

5.1.3. Sites for the Peak Region

One of the best ways to investigate the kind of interstitial sites present in an amorphous metal from a theoretical point of view is by examination of a computer model. Several investigators have worked on this. Ahmadzadeh and Cantor(5.6) have examined hard sphere and computer-relaxed soft sphere models for polyhedra of atoms connected by distances less than some cutoff distance. This was done only for a pure metal with all spheres having the same radius. They do not in this way account for all the volume, but they find tetrahedra and octahedra in ratios that agree qualitatively with those of Finney and Wallace(5.5) and Bernal. Their distributions of saddle point and interstitial radii show distinct bimodal behavior similar to those of Finney and Wallace mentioned near the end of chapter 1. However, unlike Finney and Wallace, they were able to identify whether the contributions came from 3- or 4-sided faces for saddle points, or from tetrahedra or octahedra for site minima. For the relaxed models the portions of the distribution due to triangular saddle points and tetrahedral interstital sites, respectively, are nearly symmetrical peaks, while the 4-sided faces and octahedra provide long tails at larger radii. They did not proceed to calculate distributions of activation energies, but qualitatively the results implied, if that were done, are obvious. Richards, as mentioned above, went on to carry out those calculations.

Since possible interstitial sites in glassy metals appear to be composed mostly of tetrahedra, with a few octahedra and larger sites, it should be safe to assume that the peak in g(E) is due primarily to hydrogen atoms jumping out of tetrahedral sites, through triangular faces. As was mentioned above, we are fairly confident that the majority of H atoms sit in Zr_4 tetrahedra over the range of c covered.

5.2 TAIL REGION

We have so far mostly ignored the low energy tail of g(E). Probably its most striking aspect in figure 5.1 is the fact that it quickly saturates at a certain absolute level and increases no further, and in fact actually decreases slightly with increasing c. The hydrogen concentration at saturation is unknown, but it is less than 0.23 H/M. The almost inescapable conclusion is that it is due to an impurity trap or a deep well, such as an octahedral or larger site.

One argument that somewhat disfavors impurities as an explanation is the variation in sample preparation detailed in Chapter 3. These included the ribbons being melt-spun at different times, use of different purities of starting elements, different exposures to air at 25 C or 200 C, and different annealing times in the hydrogenation process. Therefore it might be expected that they would have different levels of O or N impurities.

A second reason to question hydrogen-impurity defects as the source of the low energy tail is that they might be expected to produce a peak rather than such a broad distribution. Further, it might be questioned whether the impurity would really pull the activation energy, as opposed to the interstital site energy, down that far.

The other possibility, deep octahedral sites, requires discussion of some considerations not yet dealt with. Repeated reference has been made to the idea that for smaller holes the hydrogen exists at a higher and steeper point on its pair potential with the metal, similar to the case illustrated in figure 2.1, but with smaller holes having the radius marked "nn" and larger holes the radius marked "nnn". This idea is supported by the fact that hydrogen causes a large lattice expansion for crystalline metals in which it occupies either tetrahedral or octahedral sites, implying that for both sites the slope of the pair potential is negative. Further evidence for this idea lies in the fact that in many metals hydrogen occupies the largest sites. Examples are hcp cobalt and fcc gadolinium for octahedral sites and bcc vanadium, niobium, tantalum, and iron for tetrahedral sites (since these are larger than the bcc octahedral sites).

On the other hand, there are some exceptions. In bcc copper the octahedral sites are occupied. In all the phases of zirconium (hcp, fcc, and face-centered tetragonal) the tetrahedral sites are occupied. Otherwise, copper and zirconium are very different with respect to hydrogen: in zirconium its heat of formation is very large and negative while in copper it is small. Evidently for these metals the simple spherical pair potential is not an adequate description of the hydrogen-metal interaction. Chemical bonding effects, including the coordination number of metal atoms around the hydrogen, may be important. In any case, though, it may be that in amorphous Zr_2Pd there are sites that have a deeper potential energy minimum than do the tetrahedral sites, with their coordination number of 4, or the octahedral sites, with a coordination number of 6. An example might be a heavily distorted octahedron, as we shall see shortly.

The other explanation of the tail region depends not only on the sites occupied but on the path taken by a hydrogen atom in hopping from one site to another. In this case these two issues are very intimately related. As already examined in a previous publication(5.18), the idea is that the tail results from hopping through four-sided or square faces, which have two degrees of freedom not present in a triangular face. For the latter the shape is fixed except for the variability of each side's length, as determined by the width of the first peak in the RDF. Allowing all three sides to vary in length results in limited variability in the radius of the hole through the center and hence limited variability in the saddle point energy. This is just the calculation carried out by Richards. We assume that the main peak in $g(E_a)$ results from hopping through these three-sided faces.

For a square face, apart from the variability in the length of the sides there is freedom to deform it into a non-square parallelogram in the plane, or to bend it out of the plane along a diagonal axis. For either deformation the diagonal length starts out at $\sqrt{2}d$, where d is the length of the side, and can decrease until it reaches a length of about d. To be specific, consider an octahedron, figure 5.7. Let it be initially elongated along the x axis. Then start compressing it along the z axis. Initially the potential energy minimum will lie at the center. As the top and bottom atoms approach each other this minimum will eventually split, say into two minima along the x axis as shown in the same figure. Just after this the activation energy for hopping between these two sites will be at a minimum. As the octahedron is compressed further along the z axis, it will rise. When the top and bottom atoms reach a distance d, the formerly square face through the center will have changed to two adjacent triangular faces, and the octahedron into four very distorted tetrahedra (with perhaps four minima

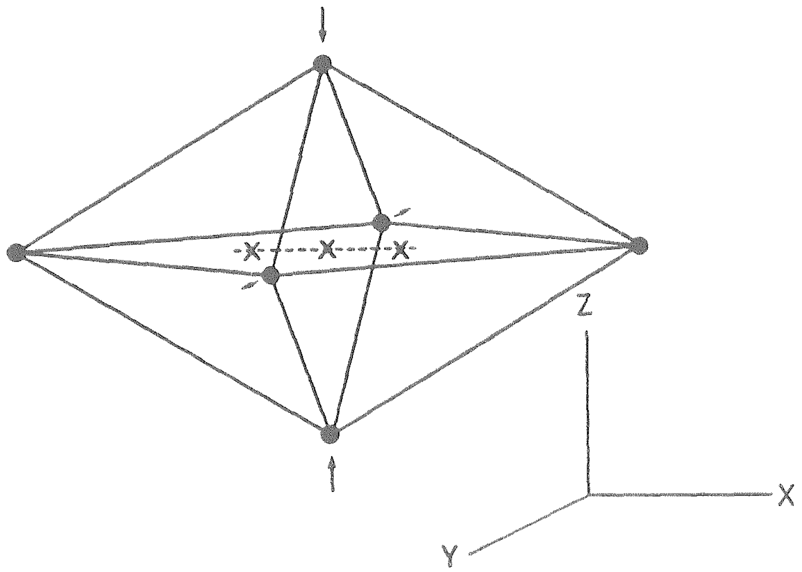

Figure 5.7 A distorted octahedron with metal atoms represented by dots and hydrogen sites by x's, used as a model for the variable saddle point energies of hopping through square faces.

in the potential energy). The activation energy for jumping through these faces will have moved continously from zero up to the value for a triangular face. For the larger sites illustrated in figure 1.4 similar considerations apply.

If we now envision an ensemble of such octahedra or other sites whose square faces are distorted to varying degrees in the metal, the result should be a smooth, continuous distribution of activation energies ranging from zero up to the main peak. This is just what is seen. Further, for the partially distorted octahedron the interstitial site energies may be low, as mentioned above, leading to the trapping behavior seen. The reason is that if an octahedron has been distorted enough that the central minimum has been split into two minima, each lying in a half octahedron (figure 1.4(b)), the site's coordination number is 5. It may be that the increase in site volume over that of a tetrahedral site lowers the potential energy more than it is raised by the increase in coordination number. This may be true even though it is not true for a coordination number of 6 or higher.

One caveat is that the total number of non-tetrahedral sites is by all accounts relatively low, perhaps of the order of 15% of all sites. But only part of these will be sufficiently distorted that they will have split into two minima, so the number of sites contributing to the low energy tail may be only a few percent. Of course, the factor $(\Delta\lambda)^2$ will undoubtedly be different than for the tetrahedral sites. If it is larger it would make the tail more prominent. It should also be noted that experimentally $g(E_a)$ does not go all the way down to zero energy as predicted but drops off to zero at about 0.07eV. The changing strength of $g(E_a)$ versus E_a in this tail region could be due either to a changing density of sites with E_a or to the $(\Delta\lambda)^2$ factor's being a function of the distortion of the square face, or both. Certainly, $\Delta\lambda$ is zero for a regular octahedron and becomes nonzero when the polyhedron is distorted, yielding a trend similar to that seen in the data.

Finally, then, we see that either impurity traps or hopping through square faces can explain the tail. The present data are not capable of distinguishing between these possibilities with certainty, but they favor the latter.

5.3 THE UNHYDRIDED ALLOY

For the unhydrided Zr_2Pd specimen the relaxation strength distribution shows some unique features. The low temperature tail is relatively very prominent, in agreement with the idea that it represents trapped hydrogen atoms. But even more striking is the double peak structure and its very high activation energy.

It is a little difficult to believe that these peaks, or even the lower one, have the same source as the peak at 0.42 eV for $c = 0.23$. It is tempting to speculate that they may arise from trapping, parhaps by O or N impurities. This would explain their higher activation energy, larger by 0.1 - 0.2 eV, which is a reasonable value for the depth of a trap. The double peak might be attributed to two kinds of traps or perhaps to first and second nearest neighbor sites around the trap, with the first nearest neighbors being the deepest.

The main problem with this picture is that as pointed out above these sites should remain present in the internal friction spectrum at higher concentrations. Much more information is needed before any conclusions can be reached. It should be useful to do NMR on low-c samples and to compare this with data for higher c to see if the hydrogen site parameters are different.

In passing we note that a small, very narrow peak was seen in the second vibration mode for the unhydrided Zr_2Pd specimen at 252 K, superimposed on the rising low temperature tail. Initially it had a magnitude of $Q^{-1} = 4 \times 10^{-5}$ and a width of about 5 K. This was remeasured in the second mode, but when the mode 3 measurements were made it had disappeared. It is so narrow that the minimum value of E_a that can be associated with it is 1.1 eV. This is suggestive of metal atom rather than hydrogen hopping and might be due either to relaxation of the glassy lattice or to anelastic relaxation in crystalline inclusions small enough to have escaped detection by X-ray diffraction. However, the latter seems unlikely in view of the fact that the peak seemed to disappear with time.

5.4 $Y_{64}Fe_{36}$ DATA

The internal friction measurements on $Y_{64}Fe_{36}$ have not been analyzed nearly as thoroughly as those of the Zr_2PdH_x alloys. As explained previously, this was due to much larger measurement error in addition to uncertainty about the high temperature rising background. In spite of this several comments can be made. The extra peak at lower temperature was not seen in the data of Kunzi, et al.(5.19) on the similar alloy $Y_{65}Co_{35}$. It was not large enough to allow its isolation from the main peak by subtraction, given the level of data uncertainty. However, it appears from visual inspection to have roughly the same 1/T shift as does the main peak in its vicinity once the backgrounds are accounted for. If so, it will have the same τ_0 value, and it can be included when computing g(E) since the inversion assumes that all relaxation components have the same τ_o. Since Kunzi, et al. found that their peak in $Y_{65}Co_{35}$ was due to hydrogen, it is a reasonable assumption that the main peak here is also. However, it would be interesting to know whether or not the small bump is hydrogen-related or not. If so, this along with the unhydrided Zr_2Pd sample become the first known examples of a hydrogen-related double peak in an amorphous alloy. If not, this would join one other possible example(5.20) as the only known internal friction peaks in non-magnetic glassy alloys.

Beyond this, the internal friction data themselves in figure 4.7 seem to show the same low temperature tail seen almost universally in metallic glasses, though due to problems discussed in Chapter 4 the $g(E_a)$ spectra do not show the peak asymmetry as clearly.

5.5 COMPARISON TO OTHER RESULTS

The similarity of the present peak shapes to those seen in $Pd_{80}Si_{20}$ and other metallic glasses has already been noted. If the low energy tail represents hopping through (distorted) square faces, that would explain its general presence in widely different glasses, assuming that all glasses have this structural feature in common. Hydrogen-impurity trapping could also explain this general phenomenon if all the hydrogenated glasses examined to date had impurities in roughly the same amounts, but this seems doubtful.

The τ_o values in $(Zr_2Pd)_1H_{.86}$ can be compared to inelastic neutron scattering results on a-Zr_2Pd hydrogenated to about the same level as the c = 0.86 sample(5.21). The energy $\hbar\omega_o$ of the transition from the ground state to the first excited state was measured as 0.125 eV. This

τ_0 is just the quantum frequency of motion of the atom in the potential well. Since this is not very small compared to the overall activation energy of .42 eV we see that quantum effects will be important, but in the classical limit the atom has the same frequency of motion as in the quantum mechanical limit and $2\pi/\tau_0$ can be identified as ω_0, with the following correction. From equation (1.20) in Chapter 1 we recall that the attempt frequency is renormalized by $\exp(\Delta s/k)$ where Δs is the difference in vibrational entropy between the saddle point and the minimum. This we can compute: the value of τ_0 from Table 1 yields $2h/\tau_0 = 0.283$ eV, so dividing by $\hbar\omega_0$ from above we get $\Delta s = k \ln 2.26$. The equivalent of about 1 extra lattice state per hydrogen atom would be created if all hydrogen atoms were at their saddle points (assuming the single atomic jump picture).

The range of activation energies seen here is also confirmed by the NMR measurements of Bowman$^{(5.22)}$, who made measurements of the proton rotating frame relaxation times $T_{1\rho}$ on hydrogenated Zr_2Pd alloys with c = .96. The proton-proton term in the dipole relaxation time dominates other contributions in this alloy, so it is a favorable one for these measurements. A large minimum was found in $T_{1\rho}$ corresponding to hydrogen hopping. These data were converted to a value of $\tau_c = \tau_d/2$ where τ_c is the mean correlation time, while τ_d is the mean residence time measured in internal friction experiments.

Bowman's resulting data are shown in figure 5.8. The plots of τ_c^{-1} for the crystalline hydrides fit well to a straight line on the Arrhenius plot, but the data for the glassy alloy show a short fairly straight region near the top followed by a curve below. This is the result of a peaked distribution of activation energies. At low tempera-

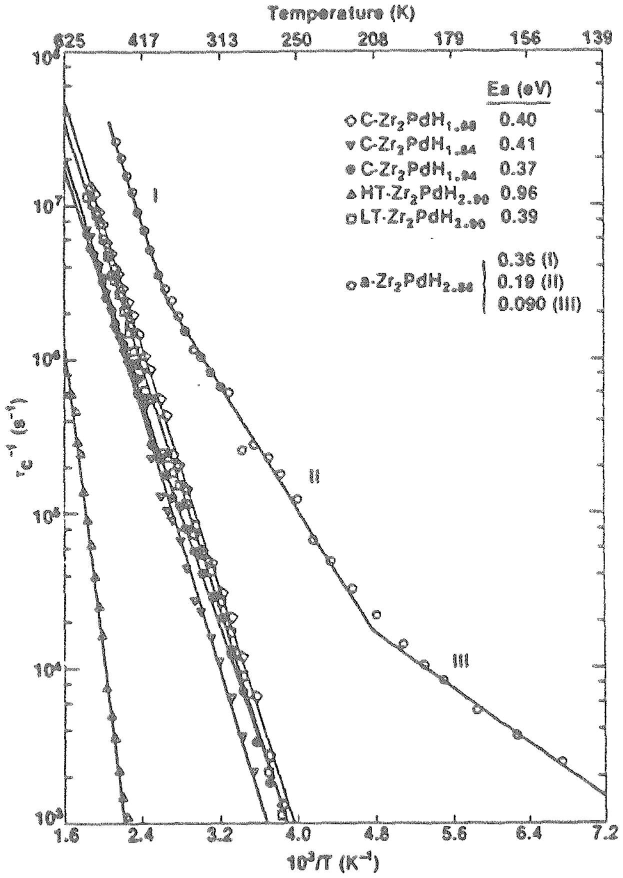

Figure 5.8 Inverse correlation times as a function of temperature from Bowman's $T_{1\rho}$ NMR data. The lines represent least-square fits to the data to give activation energies. For the a-$Zr_2PdH_{2.88}$ the curve was divided into three regions for fitting purposes. (Taken from ref. 5.22)

tures all but the lowest-E_a hops are frozen out and τ_c appears to have a small activation energy. At higher temperatures the hops with larger E_a values start contributing and overwhelm those of lower E_a because they are greater in number; g is higher there. Finally, as barriers higher than E_{max} start contributing, they make little difference because they are fewer in number. The upper behavior settles down at a slope near that given by E_{max}. Thus the peak seen by internal friction qualitatively explains the NMR data. Further, the range of values found for the apparent activation energy vary from 0.08eV to 0.43eV(5.23), agreeing perfectly with those seen for the c = .86 hydride, of 0.07eV to 0.42eV at the peak.

5.6 SUMMARY

Internal friction measurements have been made in two amorphous alloys, a-Zr_2PdH_x and a-$Y_{64}Fe_{36}$. The hydrogen-related peaks observed were mostly measured over a temperature interval of about 80 K to 370 K. For the high hydrogen concentration alloy measurements were carried on down to 10 K. In most cases measurements were made at the three lowest vibration modes of each specimen to allow fitting of an activation energy and time constant τ_0 to the temperature shifts of the peaks.

The procedure for fitting internal friction measurements made at different frequencies becomes more complicated when the peaks represent a spectrum of relaxations whose time constants are thermally activated with different activation energies. In this case a simple attempt to calculate the activation energy from the temperature shift is incorrect. The relaxation strength at a temperature then becomes a nonlocal function of $g(E_a)$, depending on its behavior in an energy interval.

This fact has not been appreciated in the past, leading to errors in calculations of activation energies. This is particularly a problem where very broad activation energy distributions are present, as in metallic glasses.

The integral equation for the anelastic modulus has been inverted using a singular value decomposition method to yield a distribution of relaxation strength over activation energy. This is the first time this has been done in a non-parametric way. The results show the qualitative features expected from the internal friction data, with an asymmetric peak and a long tail extending down to below 0.1 eV. The distributions for different frequencies generally agree well with each other for one specimen.

There is a general trend for the upper side of the peak to move to lower energy with increasing c. The only possible explanation for this appears to be the effect of lattice expansion on the activation energies for hopping out of the sites. At the high hydrogen concentrations, $c = 0.64$ and $c= 0.86$, the peak becomes much narrower and the peak position moves upward before resuming its downward trend. At the same time the peak loses intensity if normalized by c. As a result of these two effects the peak area normalized by c, and hence the calculated asymmetry of the strain dipole, are much smaller at large c. While some of this could be due to site competition between hydrogen atoms at high concentrations. the relaxation strength does not follow a $c^2(1-c)^2$ dependence. Nor is there a strong exponential dependence of relaxation strength on temperature at constant c. From these considerations it appears that the relaxing defect is Snoek-like (i.e., due to a single atom rather than H-H or H-impurity pairs or other more complex clusters), and that the nature of the hydrogen site changes considerably at large c. This may be due to a change induced in the structure of the metallic glass, an idea also supported by the x-ray diffraction experiments showing a change in Zr-Zr distances while Zr-Pd and Pd-Pd distances remain virtually unchanged.

Regardless of some of the uncertainties mentioned above, it appears correct to assume that the peak in $g(E_a)$ is due to hydrogen hopping through saddle points in triangular faces. This agrees with dense random packing models using hard spheres, or soft potentials relaxed by a computer, which show that the great majority of the faces around interstitial sites are triangular.

The low-energy tail in $g(E_a)$ saturates at low concentration, indicating that it is due to sites whose potential wells are deeper than average. A model is suggested to explain the broad featureless nature of the tail, based on hopping through four-sided faces. These can be distorted continuously from a square into a set of triangles. A distribution in this degree of distortion would account for the smooth nature of the tail, the fact that it goes to low energies, and that it continues just up to the peak. Other ideas such as impurity trapping do not explain the observations as well. The similarity of the form of the internal friction peak to other peaks reported in both transition metal-metalloid and transition metal-transition metal metallic glasses suggests that the peak shape is based on very general phenomena, of the above type.

REFERENCES

CHAPTER 1

1.1) G. Alefeld and J. Volkl, in Hydrogen in Metals I, ed. by G. Alefeld and J. Volkl, Springer-Verlag, Berlin (1978).

1.2) E. Wicke and H. Brodowsky, in Hydrogen in Metals II, ed. by G. Alefeld and J. Volkl, Springer-Verlag, Berlin (1978).

1.3) D. G. Westlake, H. Shaked, P. R. Mason, R. B. McCart, and M. H. Mueller, J. Less-Comm. Met. 88, 17 (1982).

1.4) F. Aubertin, U. Gonser, and S. J. Campbell, J. Less-Comm. Met. 101, 437 (1984).

1.5) N. Nishimiya, A. Suzuki, T. Sekine, S. Ono, and E. Asada, J. Less-Comm. Met. 88, 263 (1982).

1.6) H. Peisl, in ref. (1.1).

1.7) R. C. Bowman, Jr., E. L. Venturini, B. D. Craft, A. Attala, and D. B. Sallenger, Phys. Rev. B 27, 1474 (1983).

1.8) H. Wagner, in ref. (1.1).

1.9) A. S. Nowick and B. S. Berry, Anelastic Relaxation in Crystalline Solids, Academic Press, New York (1972).

1.10) A. S. Nowick and W. R. Heller, Advan. Phys. 12, 251 (1963).

1.11) H. Kanzaki, J. Phys. Chem. Solids 2, 24 (1957).

1.12) K. Samwer and W. L. Johnson, Phys. Rev. B 28, 2907 (1983).

1.13) K. H. J. Buschow, P. C. Bouten, and A. R. Miedema, Rep. Prog. Phys. 45, 937 (1982).

1.14) H. Buck and G. Alefeld, Phys. Stat. Sol. (b) 49, 317 (1972).

1.15) L. D. Landau and E. M. Lifshitz, Statistical Physics, 2nd ed., Pergamon Press, Oxford (1969).

1.16) J. J. Vuillemin and M. G. Priestley, Phys. Rev. Lett 14, 307 (1965).

1.17) K. W. Kehr, in ref. (1.1).

1.18) H. Eyring, J. Chem. Phys. 3, 107 (1932).

1.19) T. Springer, in ref. (1.1).

1.20) C. Baker and H. K. Birnbaum, Acta Met. 21, 865 (1973).

1.21) Z. Qi, J. Volkl, H. Wipf, and G. Alefeld, J. Physique 42, C5-763 (1981).

1.22) R. Kirchheim, Acta Met. 29, 845 (1981).

1.23) P. Vajda, J. N. Daou, J. Physique 44, 543 (1983).

1.24) J. A. Rodrigues and R. Kirchheim, Scripta Met. 17, 159 (1983).

1.25) S. Tanaka and M. Koiwa, J. Physique 42, C5-781 (1981).

1.26) W. Klement Jr., R. H. Willens, and P. Duwez, Nature 187, 869 (1960).

1.27) X. L. Yeh, K. Samwer, and W. L. Johnson, Appl. Phys. Lett. 42, 242 (1983).

1.28) R. B. Schwarz and W. L. Johnson, Phys. Rev. Lett. 51, 415 (1983).

1.29) P. H. Gaskell, in *Glassy Metals II*, ed. by H. Beck and H.-J. Guntherodt, Springer-Verlag, Berlin (1983).

1.30) J. D. Bernal, Proc. Roy. Soc., Ser. A 280, 299 (1964).

1.31) J. D. Bernal, in *Liquids: Structure, Properties, and Solid Interactions*, ed by T. J. Hugel, Elsevier, Amsterdam (1965).

1.32) M. Ahmadzadeh and B. Cantor, J. Non-Cryst. Solids 43, 189 (1981).

1.33) D. Shechtman, I. Blech, D. Gratias, and J. W. Cahn, Phys. Rev. Lett. 53, 1951 (1984).

1.34) J. L. Finney and J. Wallace, J. Non-Cryst. Solids 43, 165 (1981).

1.35) D. F. Polk, Scripta Met. 4, 117 (1970).

1.36) G. S. Cargill III, in *Solid State Physics*, Vol. 30, Academic Press, New York (1975).

1.37) B. S. Berry and W. C. Pritchet, J. Appl. Phys. 44, 3122 (1973).

1.38) H.-U. Kunzi in *Glassy Metals II*, ed. by H. Beck and H.-J. Guntherodt, Springer-Verlag, Heidelberg (1983).

1.39) D. Weaire, M. F. Ashby, J. Logan, and M. J. Weins, Acta Met. 19, 779 (1971).

1.40) R. K. Viswanadham, J. A. S. Green, and W. G. Montague, Scripta Met. 10, 229 (1976).

1.41) A. J. Maeland, in *Proc. Int. Symp. Hydrides for Energy Storage*, ed. by A. F. Adresen and A. J. Maeland, Pergamon, Oxford (1978).

1.42) R. C. Bowman, Jr., and A. J. Maeland, Phys. Rev. B 24, 2328 (1981).

1.43) A. J. Maeland, L. E. Tanner, and G. G. Libowitz, J. Less-Comm. Met. 74, 279 (1980).

1.44) K. Suzuki, J. Less-Comm. Met. 89, 183 (1983).

1.45) K. Aoki, A. Horata, and T. Masumoto, in Proc. 4th Int. Conf. on Rapidly Quenched Metals, ed. by K. Suzuki and T. Masumoto, Japan Inst. of Metals, Sendai, Japan (1982).

1.46) M. Hirabayashi, H. Kaneko, T. Kajitani, K. Suzuki, and M. Ueno, AIP Conf. Proc. #89, 87 (1982).

1.47) A. Williams, J. Eckert, X. L. Yeh, M. Atzmon, and K. Samwer, in Liquid and Amorphous Metals V, part 1, ed. by C. N. J. Wagner and W. L. Johnson, North-Holland, Amsterdam (1984).

1.48) A. J. Maeland, J. Less-Comm. Met. 89, 173 (1983).

1.49) K. Kai, T. Fukunaga, T. Nomoto, N. Watanabe, and K. Suzuki, in ref. (1.45).

1.50) K. Tanaka, M. Higatani, K. Kai, and K. Suzuki, J. Less-Comm. Met. 88, 317 (1982).

1.51) R. C. Bowman, Jr., A. Attalla, A. J. Maeland, and W. L. Johnson, Sol. State Comm. 47, 779 (1983).

1.52) F. H. M. Spit, J. W. Drijver, W. C. Turkenburg, and S. Radelaar, in Metal Hydrides, ed. by G. Bambakidis, Plenum, New York (1981).

CHAPTER 2

2.1) J. L. Snoek, Physica 6, 591 (1939).

2.2) See ref. (1.9).

2.3) B. S. Berry and W. C. Pritchet, Scripta Met. 15, 637 (1981).

CHAPTER 3

3.1) See ref. (1.52)

3.2) R. C. Bowman, Jr., M. J. Rosker, and W. L. Johnson, J. Non-Cryst. Solids 53, 105 (1982).

3.3) F. H. M. Spit, J. W. Drijver, W. C. Turkenburg, and S. Radelaar, J. Physique 41, C8-890 (1980).

3.4) B. S. Berry and W. C. Pritchet, in Rapidly Quenched Metals III, vol. 2, ed. by B. Cantor, The Metals Society, London (1978).

3.5) H. U. Kunzi, E. Armbruster, and H. J. Guntherodt, in Proc. 4th Int. Conf on Rapidly Quenched Metals, ed. by K. Suzuki and T. Masumoto, Japan Inst. Metals, Sendai (1982).

3.6) R. C. Bowman, Jr., private communication.

3.7) P. Duwez, Prog. Sol. State Chem. 3, 377 (1966).

3.8) L. M. Besley and R. C. Kemp, Cryogenics , 497 (1978).

3.9) S. Timoshenko, D. H. Young, and W. Weaver, Jr., in Vibration Problems in Engineering, 4th ed., Wiley, New York (1974).

CHAPTER 4

4.1) H. U. Kunzi, K. Agyeman, and H.-J. Guntherodt, Solid State Comm. 32, 711 (1979).

4.2) See ref. (3.5).

4.3) See ref. (1.9).

4.4) See ref. (1.37).

4.5) See ref. (3.9).

4.6) B. S. Berry and W. C. Pritchet, Scripta Met. 15, 637 (1981).

4.7) H. S. Chen, H. J. Leamy, and M. Barmatz, J. Non-Cryst. Solids 5, 444 (1971).

4.8) T. Soshiroda, M. Koiwa, and T. Masumoto, J. Non-Cryst. Solids 22, 173 (1976).

4.9) B. S. Berry, in Metallic Glasses, ed. by J. J. Gilman and H. J. Leamy, Amer. Soc. for Metals, Metals Park, Ohio (1976).

4.10) S. Tyagi and A. E. Lord, Jr., J. Non-Cryst. Solids 30, 273 (1979).

4.11) B. S. Berry, Scripta Met. 16, 1407 (1982).

4.12) B. S. Berry and W. C. Pritchet, Phys. Rev. B 24, 2299 (1981).

4.13) G. Dahlquist and A. Bjorck, Numerical Methods, Transl. by N. Anderson, Prentice-Hall, Englewood Cliffs, New Jersey (1974).

4.14) C. L. Lawson and R. J. Hanson, Solving Least Squares Problems, Prentice-Hall, Englewood Cliffs, New Jersey (1974).

4.15) D. V. Baxter, Ph.D. thesis, California Institute of Technology, Pasadena, California (1984).

CHAPTER 5

5.1) See ref. (3.4)

5.2) See ref. (3.2).

5.3) See ref. (1.9).

5.4) See ref. (1.20).

5.5) See ref. (1.34).

5.6) See ref. (1.32).

5.7) R. Kirchheim, F. Sommer, and G. Schluckebier, Acta Met. 30, 1059 (1982).

5.8) A. D. Le Claire and W. M. Lomer, Acta Met. 2, 731 (1954).

5.9) F. M. Mazzolai and H. K. Birnbaum, J. Physique 42, C5-769 (1981).

5.10) O. Yoshinari, M. Koiwa, A. Inoue, and T. Masumoto, Acta Met. 31, 2063 (1983).

5.11) See ref. (4.6).

5.12) H. U. Kunzi, E. Armbruster, and K. Agyeman, Proc. Conf. on Metallic Glasses: Science and Technology, ed. by C. Hargitai, I. Bakonyi, and T. Kemeny, Vol. 1, Central Res. Inst. Phys., Budapest (1980).

5.13) See ref. (1.12).

5.14) See ref. (1.50).

5.15) K. Agyeman, E. Armbruster, H. U. Kunzi, A. Das Gupta, and H.-J. Guntherodt, J. Physique 42, C5-535 (1981).

5.16) P. M. Richards, Phys. Rev. B 27, 2059 (1983).

5.17) See ref. (1.2).

5.18) L. E. Hazelton and W. L. Johnson, J. Non-Cryst. Solids 61 & 62, 667 (1984).

5.19) See ref. (4.1).

5.20) Y. E. Kalinin and I. V. Zolotukhin, Fiz. Tuerd. Tela 22, 223 (1980).

5.21) See ref. (1.47). Their measured concentration was 1.17 ± 0.2 as determined by weight change, which is very insensitive to hydrogen and more sensitive to absorbed oxygen or nitrogen. The hydrogenation was carried out in the apparatus described in chapter 3, under pressure conditions that should have yielded c = 0.98, which is within their error limits.

5.22) See ref. (1.51).

5.23) R. C. Bowman, Jr., J. S. Cantrell, A. Attalla, D. E. Etter, B. D. Craft, J. E. Wagner, and W. L. Johnson, J. Non-Cryst. Sol. 61 & 62, 649 (1984).